T.R.

GEBZE TECHNICAL UNIVERSITY

INSTITUTE OF BIOTECHNOLOGY

INVESTIGATION OF TRANSNEURONAL DEGENERATION IN TRAUMATIC INJURY AND NEURODEGENERATIVE DISEASES

ESRA NUR YİĞİT

A THESIS SUBMITTED FOR THE DEGREE OF

DOCTOR OF PHILOSOPHY

DEPARTMENT OF BIOTECHNOLOGY

GEBZE

2022

T.R.

GEBZE TECHNICAL UNIVERSITY

INSTITUTE OF BIOTECHNOLOGY

INVESTIGATION OF TRANSNEURONAL DEGENERATION IN TRAUMATIC INJURY AND NEURODEGENERATIVE DISEASES

ESRA NUR YİĞİT

A THESIS SUBMITTED FOR THE DEGREE OF DOCTOR OF PHILOSOPHY

DEPARTMENT OF BIOTECHNOLOGY

THESIS SUPERVISOR:

PROF. DR. IŞIL AKSAN KURNAZ

CO-SUPERVISOR:

PROF. DR. GÜRKAN ÖZTÜRK

GEBZE

2022

T.R.
GEBZE TEKNİK ÜNİVERSİTESİ
BİYOTEKNOLOJİ ENSTİTÜSÜ

TRAVMATİK HASAR VE NÖRODEJENERATİF HASTALIKLARDA TRANSNÖRONAL DEJENERASYONUN ARAŞTIRILMASI

ESRA NUR YİĞİT

DOKTORA TEZİ
BİYOTEKNOLOJİ ANABİLİM DALI

TEZ DANIŞMANI:
PROF. DR. IŞIL AKSAN KURNAZ
EŞ-DANIŞMAN:
PROF. DR. GÜRKAN ÖZTÜRK

GEBZE
2022

GEBZE TEKNİK ÜNİVERSİTESİ	**DOKTORA JÜRİ ONAY FORMU**

GTÜ Biyoteknoloji Enstitüsü Yönetim Kurulu'nun 28/01/2022 tarih ve 2022/03 sayılı kararıyla oluşturulan jüri tarafından 10/02/2022 tarihinde tez savunma sınavı yapılan Esra Nur Yiğit'in tez çalışması Biyoteknoloji Anabilim Dalında DOKTORA tezi olarak kabul edilmiştir.

JÜRİ

ÜYE (TEZ DANIŞMANI):	Prof. Dr. Işıl KURNAZ
ÜYE:	Prof. Dr. E. Damla ARISAN
ÜYE:	Doç. Dr. Tunahan ÇAKIR
ÜYE:	Dr. Öğr. Üyesi Hüseyin ÇİMEN
ÜYE:	Dr. Öğr. Üyesi Neşe AYŞİT

ONAY

Gebze Teknik Üniversitesi Fen Bilimleri Enstitüsü Yönetim Kurulu'nun

...../...../…… tarih ve ……/…..... sayılı kararı.

İMZA/MÜHÜR

SUMMARY

In this study, we implemented different neurodegenerative disease models including Parkinson's disease (PD), Huntington's disease (HD) and traumatic injury in varied cell types, assessed their feasibility as a model for studying transneuronal degeneration, and investigated possible neuroprotection mechanisms. In modelling PD, we used two paradigms: while overexpression of wild type or mutant α-synuclein did not cause significant cell death in SH-SY5Y and LUHMES cell lines, induction of cell death was confirmed upon 6-OHDA treatment. We confirmed that 6-OHDA treatment induces Parkinsonian toxicity in SH-SY5Y and LUHMES cells. Using this *in vitro* PD model, a drug repositioning approach revealed that pretreatment of Quercetin and Rutin is neuroprotective in 6-OHDA induced PD model in both SH-SY5Y and LUHMES cells. We further shown that Elk1 overexpression is neuroprotective through the same gene pathways as Quercetin and Rutin. In order to establish the *in vitro* HD model, we overexpressed wildtype vs mutant Huntingtin (mHtt) protein in HEK293T cells and in primary neurons. We observed that mHtt formed mostly cytoplasmic aggregates in HEK293T cells and nuclear aggregates in primary neurons. We found that localization of mHtt aggregates coincided with accumulation of F-actin. Additionally, we found that overexpression of phosphomutants of Elk1 decreases mHtt aggregation, indicating it can have a neuroprotective effect not only in PD but also in HD. Long term monitoring revealed that mHtt aggregates are not degraded even if mHtt overexpressing neurons died and possibly cause toxicity to surrounding healthy neurons. This has confirmed the presence of TND in *in vitro* HD model. Besides, time lapse calcium imaging revealed that *in vitro* induction of either PD or HD resulted with synchronized calcium activities with higher frequencies in neurons, even the cells do not express mHtt themselves. *In vitro* and *in vivo* single cell axotomies further revealed that injury in a single neuron triggers a synchronized calcium activity similar to observed in PD or HD and death of surrounding healthy neurons which is significantly decreased in P2X7 knockout cells.

Key Words: Parkinson's disease, α-synuclein, Huntington's disease, Huntingtin, Traumatic injury, Transneuronal degeneration, SH-SY5Y, LUHMES.

ÖZET

Bu çalışmada, çeşitli hücre tiplerinde Parkinson hastalığı (PH), Huntington hastalığı (HH) ve travmatik yaralanma dâhil olmak üzere farklı nörodejeneratif hastalık modelleri ve bunların transnöronal dejenerasyon modeli olarak kullanılabilirliği değerlendirilerek olası nörokorunma mekanizmalarını araştırdık. PH modellemesinde iki paradigma kullandık: yabani tür veya mutant α-sinükleinin aşırı anlatımı anlamlı bir hücre ölümüne neden olmazken 6-OHDA uygulamasının SH-SY5Y ve LUHMES hücrelerinde hücre ölümünü indüklediği doğrulandı. 6-OHDA uygulamasının SH-SY5Y ve LUHMES hücrelerinde Parkinson benzeri toksisiteye sebep olduğunu doğruladık. Bu *in vitro* PH modeli kullanılarak uygulanan ilaç yeniden konumlandırma yaklaşımı, Quercetin ve Rutin'in ön tedavisinin, hem SH-SY5Y hem de LUHMES hücrelerinde 6-OHDA ile indüklenen PD modelinde nöroprotektif olduğunu ortaya koydu. Ek olarak, Elk1 aşırı anlatımının, Quercetin ve Rutin ile aynı gen yollarını etkileyerek nöroprotektif olduğunu gösterdik. *In vitro* HH modelinin oluşturulması için, HEK293T hücrelerinde ve birincil nöronlarda yabani tür ve mutant Huntingtin (mHtt) proteininin aşırı anlatımı sağlandı. mHtt agregatlarının, HEK293T hücrelerinde çoğunlukla sitoplazmik, nöronlarda ise nükleer agregasyonlar oluşturduğunu gözlemledik. Ayrıca mHtt agregatlarının F-aktin ile birlikte biriktiği gösterildi. Buna ek olarak, Elk1'ın fosfo mutantlarının aşırı anlatımının mHtt agregasyonunu azaltması sadece PH'da değil, HH'da da nöroprotektif bir etkiye sahip olabileceğini gösterdi. Uzun süreli canlı görüntüleme, aşırı mHtt anlatımı bulunan nöronlar ölse bile mHtt agregatlarının ortamda kaldığını ve muhtemelen çevredeki sağlıklı nöronlarda toksisiteye neden olduğunu ortaya koydu. Bu bulgular, *in vitro* HH modelinde TND'nin varlığını doğruladı. Ayrıca, kalsiyum görüntülemesi yapılan hücrelerde PH veya HH indüklenmesi ile nöronlarda mHtt anlatımı bulunmasa da senkronize ve yüksek frekanslı kalsiyum aktivitesi gözlendi. *In vitro* ve *in vivo* tek hücre aksotomileri, tek bir nörondaki hasarın, PH ve HH ındakine benzer bir şekilde çevredeki nöronlarda senkronize bir kalsiyum aktivitesini ve çevredeki sağlıklı nöronların ölümünü tetiklediğini ve bunun P2X7 ekspresyonu bulunmayan hücrelerde anlamlı ölçüde azaldığını ortaya çıkardı.

Anahtar Kelimeler: Parkinson hastalığı, α-sinüklein, Huntington hastalığı, Huntingtin, Travmatik hasar, transnöronal dejenerasyon, SH-SY5Y, LUHMES.

ACKNOWLEDGEMENTS

First and foremost, I am grateful to my supervisors Prof. Dr. Işıl AKSAN KURNAZ and Prof. Dr. Gürkan ÖZTÜRK for their continuous support, endless patience and invaluable guidance throughout my PhD and beyond.

I would like to thank my project supervisor Doç. Dr. Tunahan ÇAKIR as he gave me an opportunity to work in his project and inspire me to broaden the scope of my studies.

Also, I would like to thank my thesis defense committee members Prof. Dr. Elif Damla ARISAN, Dr. Öğr. Üyesi Hüseyin ÇİMEN, and Dr. Öğr. Üyesi Neşe AYŞİT for their support and kindness.

I would like to thank Dr. Mehmet Şerif AYDIN for always being there for me; without his priceless emotional and scientific support, I could not complete this thesis.

I would like to thank especially Dr. Melis SAVAŞAN SÖĞÜT and MSc. Ekin SÖNMEZ for their helpfulness, assistance and collaborative work and all other members of Axan Lab including Dr. Başak KANDEMİR, Dr. Oya ARI UYAR, MSc. Yiğit Koray BABAL, MSc. Gülbahar ÇAĞIL, MSc. Büşra Nur ÇİÇEK, MSc. Betül ERTURAL, MSc. Doğukan METİNER and MSc. Merve ÜSTÜN. Also I would like to thank all my labmates in Öztürk Lab. including MSc. Olgu Enis TOK, MSc. Sevginur BOSTAN, Dr. Sadık BAY, MSc. Safiye SERDENGEÇTİ, MSc. Ayşe Server SEZER, MSc. Gülsena BAYDAŞ, Dr. Şükriye BİLİR, MSc. Şeyma KABLAN ÇİMEN, Şevval ŞİMŞEK, MSc. Cemil ÖZGÜL and SABİTA/MEDİTAM staff starting with Hilmi Kaan ALKAN, Mehtap ŞİMŞEK, Büşra BATĞİ, Arda KEBABÇI, Ekrem ÖZDEMİR and Ali ŞENBAHÇE.

I would like to extend my thankfulness to my dearest friends MSc. Burcu KURT VATANDAŞLAR, MSc. Emre VATANDAŞLAR, MSc. Fatmagül İlayda AYDINLI., MSc. Tuba OĞUZ and MSc. Zeynep ALADAĞ.

I would like to thank my beloved husband Doğuhan Burak YİĞİT for his endless love, support and patience throughout my busy pace of timeless working hours.

Last but not least, I thank my dear mother Nebiye SARI, my sister Berra and my father Cemalettin EKMEKCİOĞLU for their unconditional love.

I want to thank TUBITAK BIDEB 2211 - National PhD Scholarship Programme for funding my PhD education. This study was partially supported by TUBITAK under the research grant no: 315S302 and GTÜ BAP under grant no: 2018-A101-03.

TABLE of CONTENTS

LIST of ABBREVIATIONS and ACRONYMS

Abbreviations and Acronyms		Explanations
5xFAD	:	Transgenic mice expressing a total of 5 AD-linked mutations
6-OHDA	:	6-hydroxydopamine
AD	:	Alzheimer's disease
AIF	:	Apoptosis inducing factor
BBB	:	Blood Brain Barrier
CLEM	:	Correlative light and electron microscopy
DRG	:	Dorsal root ganglion
ETS	:	E-twenty six
HD	:	Huntington's disease
HEK293T	:	Human embryonic kidney 293 cells
Htt	:	Huntingtin protein
KO	:	Knock-out
LUHMES	:	Lund human mesencephalic cells
mHtt	:	Mutant Huntingtin protein
PD	:	Parkinson's disease
PTM	:	Posttranslational modification
PTP	:	Permeability transition pore
RIN	:	RNA integrity
ROS	:	Reactive oxygen species
SNpc	:	Substantia nigra pars compacta
TCF	:	Ternary Complex Factor
TND	:	Trans neuronal degeneration

LIST of FIGURES

LIST of TABLES

1. INTRODUCTION

1.1. Transneuronal degeneration

Neurodegeneration refers to progressive loss of nerve cells involving many complex events taking place consecutively [1]. In many tissues, a damage can be recovered physiologically but generally this is not the case for nervous tissue. As symptomatic evidences are detectable after significant neuron death in most neurodegenerative processes, it is crucial to define sequential events that is responsible for the progressive nature of neurodegeneration that take place following initial degeneration [2].

Neurodegeneration can be induced by genetics or environmental factors as well as traumatic injuries. Regardless the reason, neurodegeneration can also be separated in two major phases as primary and secondary injury phases. Neural tissue injury induces two distinct events in succession: Primary injury and secondary injury. Local response in the trauma region is called as primary injury and the subsequent disruptive changes which generally arose after a significant time period is called secondary injury [3]. In most cases of traumatic brain injury, death occurs days or even weeks after trauma. Primary injury initiates a series of disruptive events termed as secondary injury [4]. Secondary injury starts with cerebral events including astrocytic activity and blood-brain barrier disruption which results with activation of NMDA and AMPA receptors leading to depolarization and degenerative events and may affect surrounding healthy cells as well as the primary injury site in a continuous manner. As degree of degeneration is increased, axonal calcium increases and activates cytoskeletal breakdown in axons. Axonal degeneration will cause disruption of synaptic connections which in turn cause the spreading of degeneration to healthy neurons which are synaptically connected to the injured neurons (

Figure 1.1) [5]. Spread of degeneration from primarily injured neurons to neighboring healthy neurons is termed as **transneuronal degeneration (TND)**. Besides neuron-to-neuron interactions, involvement of surrounding glial cells also contributes to the transneuronal degeneration by activation of inflammatory processes.

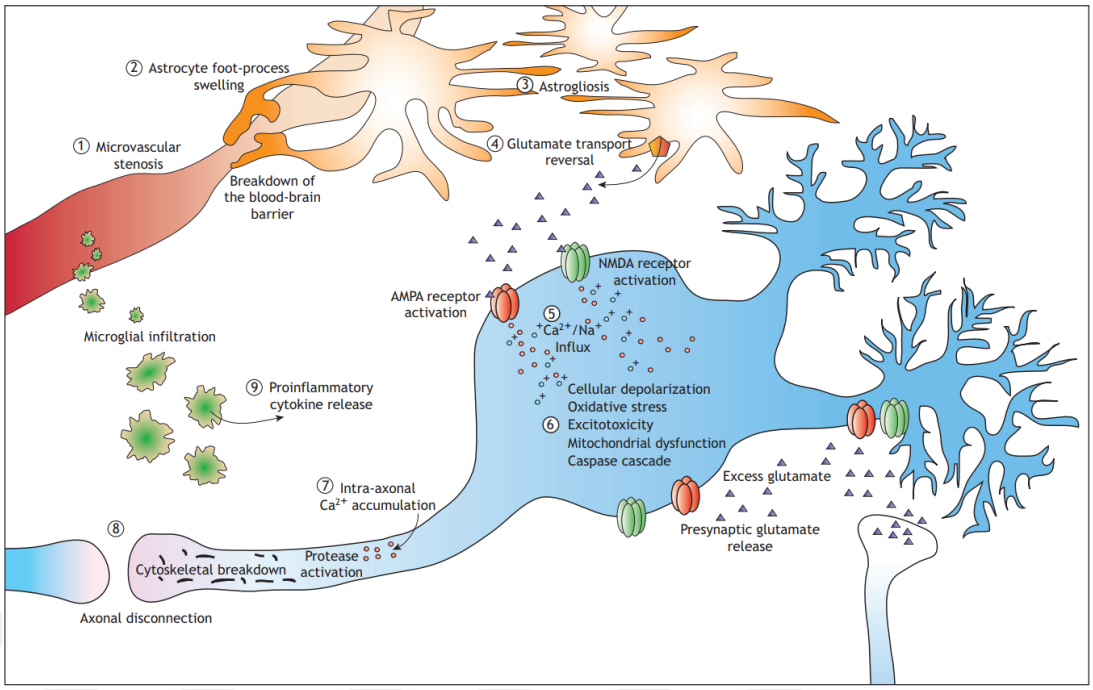

Figure 1.1: Sequential events that take place after traumatic injury. Traumatic injury triggers a series of events leading to robust neurodegeneration. Astrogliosis and blood-brain barrier (BBB) breakdown occur simultaneously and acts a first sign of degeneration which results with microglial infiltration hence activation of immune response through proinflammatory cytokines. Astrocytic activation causes glutamate release and activation of NMDA/AMPA receptors which in turn increase oxidative stress and excitotoxicity through intracellular calcium increase. A neuron with increased intracellular calcium levels release glutamate which in turn results with toxicity in the surrounding healthy cells. Additionally, axonal accumulation of calcium activates axonal proteases which in turn induces cytoskeletal breakdown [5].

While this classification is explicit in traumatic injuries, it is more complicated in progressive diseases such as Alzheimer's disease (AD), Parkinson's disease (PD) or Huntington's disease (HD). Degeneration takes place in a specific brain region and spread to the surrounding cells in time. This spreading process takes days/weeks in case of traumatic injury while it takes years in progressive neurodegenerative diseases. In traumatic injury, acute loss of cells and severe excitotoxicity is one of the main reasons of this difference but as the neurodegeneration spread, cell loss accelerates and secondary injury takes the place of primary injury [4].

1.2. Common Pathways Among Neurodegenerative Diseases

Generally, studies are focused on a single neurodegenerative condition at a time and this extensive approach let us understand many molecular mechanisms underlying each condition in detail [6]. Oxidative stress, mitochondrial dysfunction and aging are considered as driving forces of most of the cases especially in sporadic conditions [7]. Besides, neuroinflammation, glutamate excitotoxicity and synaptic dysfunction is present in nearly all cases of neurodegeneration, whether familial or sporadic, and thought the play a significant role in cell-to-cell spread of degenerative signaling [8]. On the other hand, genetic susceptibility possibly determines the form of neurodegeneration, originating brain area or the type of aggregation profile as its in many proteinopathies [9].

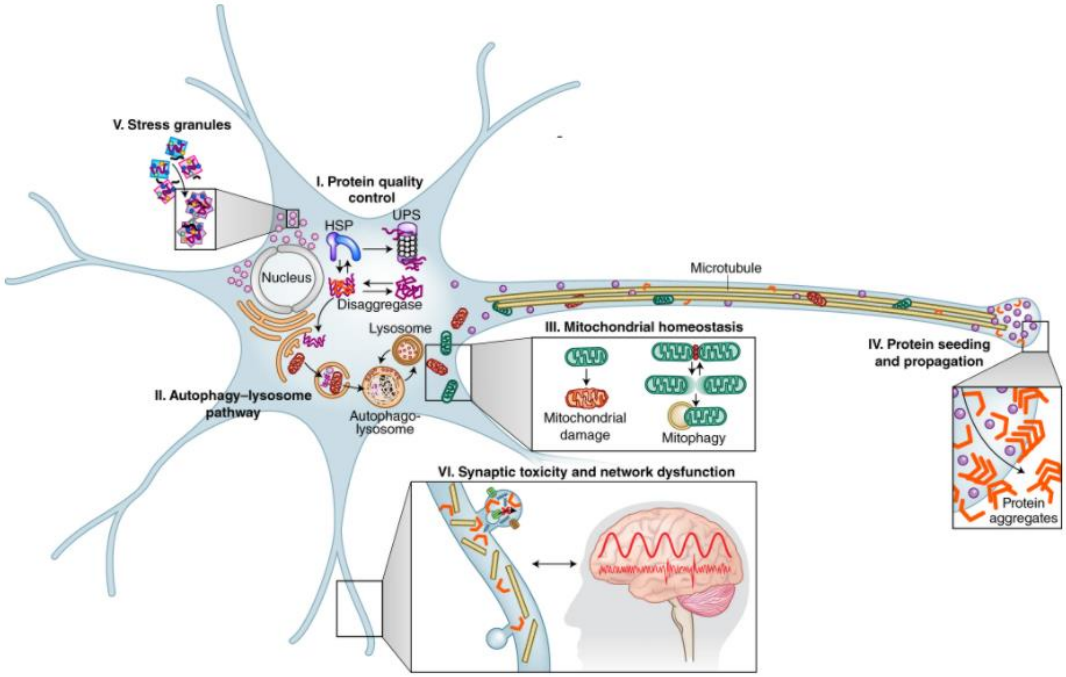

Figure 1.2: Common pathways among neurodegenerative diseases.

Neurodegenerative diseases have common mechanisms that lead to progression of degeneration. Disruptions in ubiquitin proteasome system and autophagy-lysosome pathway leads to accumulation of unfolded proteins which in turn results with axonal or somatic protein aggregation, mitochondrial dysfunctions and synaptic alterations [10].

Some mechanisms for progression proteinopathies have been proposed: these include sequential spreading, skein-like inclusions, cross-seeding and exosome mediated transportation, trans-synaptic propagation and tunneling nanotubes are some of these mechanisms [8], [11]. Although most neurodegenerative diseases are characterized by a specific protein aggregation profile, pathological evidence shows common pathways also include disruptions in ubiquitin-proteasome system (UPS), or lysosomal pathway which increases protein aggregation and a series of degenerative events such as mitochondrial dysfunctions, synaptic disconnections as it seen in the secondary injury phase of traumatic brain injury (**Figure 1.2**) [10]. Investigating different studies about different neurodegenerative conditions provides insight about possible common mechanisms but revealing common molecular pathways among different neurodegenerative conditions in a single experimental platform would provide us with more reliable and valuable information about the spread and progression of these conditions through healthy cells.

1.3. Traumatic Injury

A series of events which can be broadly classified as cerebral, cellular or inflammatory processes take place upon traumatic brain injury [12]. The most prominent feature of traumatic brain injury is the excess release of excitatory neurotransmitters, mainly glutamate, resulting with NMDA receptor activation and increased intracellular calcium levels in close proximity of the injury zone [13, 14]. As the primary injury comprised of a mechanical breakdown, membrane integrity of the injured cells will be disrupted which causes robust influx of Ca ions [15]. Many crucial events in cells depend on calcium fluxes and activated in response to interruption of calcium homeostasis [16]. Increased cytoplasmic calcium leads to production of reactive oxygen species (ROS) in a direct or mitochondria dependent manner through formation of mitochondrial permeability transition pore (PTP), which in turn results with the release of NAD^+, $NADP^+$, cytochrome c and apoptosis inducing factor (AIF) (**Figure 1.3**) [17, 18].

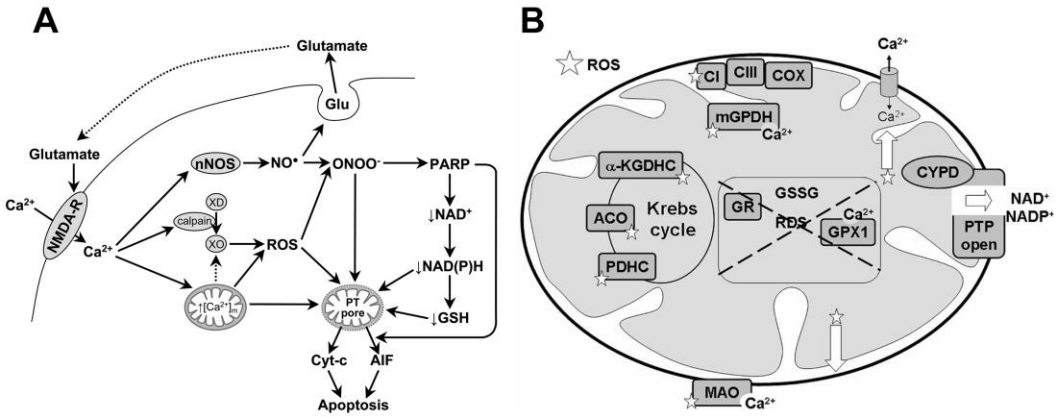

Figure 1.3: Events occurring in response to cytoplasmic calcium increase. A) Increased extracellular glutamate levels induces calcium uptake through NMDA receptors which leads initiation of apoptotic processes via direct calpain- and mitochondria-dependent manner [17] . B) Calcium dependent formation of PTP causes NAD^+ and $NADP^+$ release leading to ROS production [18].

As well as traumatic injury causes disruptive events in central nervous system, similar consequences can also be observed in peripheral nerve injuries, ie neuropathic pain. Additionally, single cell studies post-injury revealed that each neuronal sub-type has been shown to respond to injury differently in either peripheral or central nervous system [19, 20]. So, it is crucial to study the degenerative processes in single cell level to discriminate between the complex consequences arising after different neurodegenerative conditions.

1.4. Parkinson's Disease

Parkinson's disease is characterized with specific loss of dopaminergic neurons in substantia nigra pars compacta (SNpc) and accumulation of Lewy bodies in the same area [21]. Lewy bodies are inclusion bodies that are composed of mainly α-synuclein aggregates [22]. Although most of the Parkinson's disease cases are sporadic, genetically inherited forms provide valuable information about the pathogenesis and molecular mechanisms leading to neurodegeneration [23]. Mutations in *SNCA, LRRK2, PARKIN, DJ-1, PINK1* and *ATP13A2* genes are commonly found in familial forms of PD [24]. Multiplication of *SNCA* locus or A53T, E46K and A30P

point mutations induce PD pathology in different severity levels through formation of toxic α-synuclein oligomers [25-28]. Point mutations in α-synuclein disrupt its α-helical structure leading to impairments in synaptic release through reduction in its membrane binding capacity [29].

Mutations in *LRRK2* gene mostly associated with neuroinflammation. Patients with sporadic PD pathology showed induced immune response and increased expression of LRRK2 in immune cells which can contribute to PD pathology [30].

Parkin protein catalyzes ubiquitination of mitochondrial proteins and serine/threonine kinase PINK1 phosphorylates Parkin protein. Mitochondrial depolarization induces PINK1 phosphorylation of Parkin and Parkin is transferred to mitochondria to initiate mitophagy [31]. Loss of function mutations in PINK1 and/or Parkin causes impairment in mitochondrial vesicle trafficking resulting with defective mitochondria repair mechanism [32].

Finally, DJ-1 is a chaperone protein which functions as an oxidative stress sensor and activated in response to ROS production [33]. It is shown to protects cells from 6-OHDA induced oxidative stress, a mechanism which is impaired in the presence of point mutations in it 51. and 53. aminoacids [34]. Additionally, interaction of DJ-1 with ERK cause activation of ERK, which eventually phosphorylates Elk-1 and generates a protective response through SOD1 expression [35].

1.5. Huntington's Disease

Huntington's Disease (HD) is a neurodegenerative disease characterized by motor and cognitive disorders, which includes the death of GABAergic middle spiny neurons and cholinergic neurons in the striatum [36]. Mutations in the exon-1 region of the gene encoding the Huntingtin (Htt) protein cause an increase (>35) in CAG nucleotides and, accordingly, the elongation of the glutamine (Q) stretch in the N-terminus of the Htt protein (polyQ) [37]. Mutant Huntingtin protein (mHtt) is prone to oligomerization and causes accumulation of fibrillar aggregates in cells [38]. It is known that wildtype Htt plays crucial roles in various physiological processes such as cell to cell signaling, cytoskeletal dynamics, exocytosis/endocytosis and vesicle transport [39-41]. It is also known that wildtype Htt is involved in intracellular trafficking through interaction with motor machinery or direct binding to tubulin [42-45]. Gauthier et al showed that wildtype Htt mediates vesicular transport through

interaction with Huntingtin associated protein-1 (HAP-1) and $p150^{Glued}$ subunit of dynactin. In the presence of polyglutamine expansion, mHtt - HAP-1 and $p150^{Glued}$ interaction is increased which resulted with sequestration of those proteins and decreased microtubule binding hereby impaired vesicular transport [46]. Additionally, Contanzo et al and Waelter et al showed that vimentin filaments are redistributed around mHtt aggregates like a cage structure [47, 48]. Besides, vimentin overexpression increased mHtt aggregation through its phosphorylation by Rho-associated protein kinase (ROCK) resulting with sequestration and immobilization of IRBIT protein to mHtt aggregates [49]. Another study stated that mHtt impairs actin stress response through transglutaminase 2 activation and defective actin turnover caused by high actin-cofilin cross-linkage [50].

1.6. Purinergic Signaling in Neurodegeneration

Purines are studied widely in nervous system as they have neuromodulation role and are accepted as cotransmitters [51-53]. In physiological conditions they are released with neurotransmitters such as catecholamines, acetylcholine and dopamine [52, 54, 55]. Purinergic receptors are classified as P1 and P2 receptors which are adenosine and ATP gated channels respectively. P2 receptors are separated into two major groups: ionotropic receptors (P2X receptors) and metabotropic receptors (P2Y receptors) [56, 57]. Upon ATP binding, P2X receptors go through conformational change and open a nonselective cation channel triggering signaling cascades mainly dependent on influx of Ca2+ ions [58].

Our previous findings indicate that, purinergic signaling plays an important role in transneuronal degeneration (TND). We have developed an in-vitro single cell axotomy model to study TND. Based on our previous results, we found that a defined number of single cell axotomies in a defined area in DRG (dorsal root ganglion) cell culture initiates a degenerative cascade (Yiğit et al, under preparation). Cell viability is decreased in uninjured cells following axotomy and it can be prevented by treating cells with purinergic P2X7 receptor inhibitor Brillant Blue G (BBG). Interestingly, immunocytochemistry analysis revealed that DRG neurons do not express P2X7 receptor but the glial cells do. Dye uptake analysis confirmed that single cell neuron axotomy triggers receptor opening in surrounding glial cells in a time scale as short as 15 min, and this increase is also prevented by blocking P2X7 receptors.

In literature, it is shown that P2X7 polymorphism (1513A>C) is a risk factor for the sporadic form of PD [59]. In addition, 6-OHDA treatment of neurons in substantia nigra decreased expression of P2X and P2Y receptors of striatal and GABAergic interneurons [60]. As opposite, extracellular ATP shown to increase aSyn expression in neurons through P2X1 activation [61]. Also, blocking P2X7 receptor with A438059 shown to inhibit DA deficiency in striatum but not promoting survival of dopaminergic neurons [62]. In another study, it is shown that P2X7 receptor activation caused ATP release via Pannexin1 and aSyn decreased the extracellular ATPase activity which creates a positive feedback leading to aSyn accumulation [63].

In a transgenic mouse model of AD, it was shown that P2X7 receptors are upregulated near Amyloid beta plaques [64]. In a different study, P2X7 was shown to be overexpressed in brain samples of AD patients [65]. In an in-vitro study, cultured human microglial cells are treated with AB1-42 peptide and P2X7 expression significantly increased in treated cells compared to control cell. Similar with the findings in PD, presence of AB induces Ca2+ influx, ATP release and interleukin beta (IL-1B) secretion in microglial cultures or hippocampal slices in WT mice while this couldn't be observed in P2X7 KO mice [66]. Interestingly, in an AD mouse model (APPswe/PS1dE9) with presenilin1 and APP mutations, P2X7 immunoreactivity was observed in activated microglial cells even before AB plaque formation [67].

HD is an autosomal dominant genetical disorder, which is characterized by mutations in Huntingtin (Htt) protein results with expanded CAG repeats in exon-1. It is shown that mutant Htt expressing neurons are more prone to apoptosis by P2X7 stimulation. Also, transgenic model of HD showed altered levels of P2X7 in neurons [68].

Based on these findings, it is possible that purinergic signaling, especially P2X7 receptor to has a common role in neurodegenerative diseases. And based on our findings, we hypothesized that this common role may be related to TND observed in different conditions.

1.7. Elk-1 and its Association with Neurodegenerative Diseases

Elk1 is a member of the TCF (ternary complex factor) subfamily of the ETS (E twenty-six) oncogene transcription factor family which is strongly expressed in the

central nervous system. Activation of Elk-1 can affect several cellular functions such as survival, proliferation and differentiation [69].

The activity of the Elk1 protein is mainly determined by its post-translational modifications. In order to understand the different roles of Elk-1 in the cell, its structure and post-translational modification sites should be examined in detail. The Repression (R) domain and transactivation (C) domain of Elk1 are the main regions that determine its activity and have post-translational modifications (PTM) [70]. SUMOylation of the lysine regions in the R domain or dephosphorylation suppress the transcriptional activity of Elk1, while the phosphorylation of amino acids in the C domain by JNK, ERK and p38 kinases increases transcriptional activity.

Phosphorylation of Serine 383 and 389 regions of Elk1 by ERKs has been shown to be important for Elk1 activity. Serine 383 phosphorylation has been found in Elk1 proteins in both the cytoplasm and the nucleus. Prevention of phosphorylation from S383 and S389 results with cytoplasmic localization Elk1 [71]. It has also been stated that Serin 383 and 389 phosphorylation increases the DNA binding affinity of Elk1 and provides transcription activation [72].

It has been shown that amyloid beta application in primary neuron cultures increases the sensitivity of neurons by preventing BDNF-dependent Elk1 activation [73]. In addition, the fact that Elk1 is a potential suppressor of the gene of PSEN-1 suggests that it will play a protective role in toxic amyloid beta accumulation [74]. Contrary to these findings, it has been shown that the phosphorylated form (T417+) of the Threonine 417 region, which is known as the cytoplasmic toxic form of Elk1, is colocalized with Lewy bodies in Parkinson's disease and inclusion bodies in Huntington's and Alzheimer's patients [75].

In Huntington's disease, activated ERK and Elk1 proteins were found in the striatum region of the R6/2 transgenic mouse model used as the Huntington model. Although it is not certain whether the activation of Elk1 in neurodegeneration processes is an intracellular survival mechanism or a process leading to cellular death, it has been shown that ERK inhibition increases cell death in R6/2 mice [76]. Another study in R6 transgenic mice and a striatal cell model showed that although the amounts of Elk1 and pElk1S383 are increased in the striatum, Elk1 in the nucleus is not colocalized with Htt aggregates, moreover, when the Elk1 level is decreased using

siRNA, cell death increases and therefore activation of Elk1 is considered as an intracellular survival mechanism [77].

1.8. *In vitro* Models of Neurodegeneration

Neurodegenerative diseases are studied widely in both *in vivo* and *iv vitro* systems. Both have their own advantages and disadvantages compared with each other. *In vivo* models can be a more realistic model which mimics the real disease condition while in-vitro models have a more isolated environment hence making it easier to work with a single or limited number of cell type.

Parkinson's disease (PD) is a progressive disorder which is characterized symptomatically by motor dysfunction, tremor and rigidity [78]. Degeneration of striatal neurons and loss of dopaminergic neurons in SNpc and formation of Lewy bodies containing aSyn aggregates intracellularly are some of the physiological hallmarks of PD [79]. PD can emerge as familial or sporadically but the familial PD is very rare comparing to sporadic forms. PD models can be classified as two major subtypes as neurotoxin and genetically induced models. 6-hydroxidopamine (6-OHDA), rotenone and MPP are some of the widely used neurotoxins to model PD. These neurotoxins cause toxicity by oxidation and hydrogen peroxide formation on treated cells [80]. Overexpression of wildtype (WT) or mutant forms of aSyn to induce production of aggregates and monitor pathology are also used widely [81, 82]. In literature, there are some contradictory results about aSyn toxicity, some studies indicate that aSyn overexpression causes toxicity while others show that aSyn expression is protective in case of some toxic insults and some research indicates that aSyn overexpression make cells vulnerable to toxic insults but not sufficient to induce toxicity by its own [83-87]. Different cell types are used for modelling PD in cell culture. HEK 293T, SH-SY5Y, PC12, primary midbrain cells and LUHMES cell lines are some of these cells. In our study, we have used SH-SY5Y and LUHMES cell lines as PD models.

Huntington's disease (HD) is an autosomal dominant neurodegenerative disease characterized symptomatically by motor and cognitive deficits. As it is an inherited disease, modelling HD is simpler than PD or AD. Overexpression of the exon-1 of mutant Huntingtin (mHtt) protein with expanded CAG repeats is the most commonly used model to study HD.

All of the aforementioned *in vitro* models are widely used and accepted as reliable models of these neurodegenerative diseases. On the other hand, Co-culture systems are used less comparing to the methods above [88]. Generally, co-culture systems are used to monitor cell-to-cell transfer of protein aggregates and can be implemented by either using multi-well systems or mixed co-cultures [89]. Our cell culture model is aimed to obtain a neurodegeneration initiating region on a culture for obtaining a reliable system and make it easier to monitor disease progression process.

1.9. *In vivo* Models of Neurodegeneration

Animal models give valuable information about the pathogenic processes occurring in the neurodegenerative diseases and provide a valuable platform for developing therapeutics. Broadly, *in vivo* models can be divided into genetic and chemical based models. Choosing and obtaining a suitable model that meets the criteria of a specific research is crucial. Depending on the aim of the study, time span, severity and localization of the degeneration should be considered carefully.

In the case of proteinopathies that have a genetic background or clue, transgenic mice are used widely. In the case of AD, which has a well-defined genetic background, one of the mostly used strain is 5xFAD mice, which carries a total of 5 mutations in APP and presenilin genes, and exhibits beta-amyloid aggregates and neuronal degeneration as main hallmarks of AD [90]. Transgenic mice strains for modelling PD is also exists and widely used. Mice that express A53T mutant aSyn, G2019S mutant LRRK2 under different promoters are used as animal models of PD [25, 27, 91]. In the case of HD, strategy is much more straightforward: transgenic mice encode for mutant Htt with different number of CAG repeats, resulting in different sizes of polyQ repeats in either full-length or only exon-1 of Htt; the size of polyQ stretch determines both the severity and age onset of the pathology in the animal [92-95].

Besides genetics-based models, chemical models are also used as they represent the sporadic cases, are less expensive than transgenic models, and give faster results. However, heterogeneity between animals as well as the spatial and temporal limitations of the chemical agent are among the disadvantages of chemical models. Similar to *in vitro* models Rotenone, 6-OHDA and MPTP administration are widely used for inducing Parkinsonian degeneration in mice or primates [96]. All of these drugs can pass BBB and inhibit mitochondrial complex I [96]. Rotenone induces

neurotoxicity through mitotic inhibition and impairment in mitochondrial energy metabolism and selectively causes nigrostriatal degeneration in low concentrations [97]. MPTP and 6-OHDA induces oxidative stress through disruption of mitochondrial electron transport chain and ROS production respectively [80].

Traumatic injury models are classified as impact acceleration, nonimpact acceleration and direct deformation models [98]. A common feature of these models is difficulty to study disease in single cell level. For overcoming this issue, inducible or constitutive gene expression is achieved via viral based gene delivery. By using viral delivery, embryonic lethality that may arouse from the knock-in/knock-out of specific gene can be avoided, targeted expression is possible and progression of neurodegeneration can be observed in a controlled way. In the case of traumatic injury, the aforementioned methods result with broad injury that makes it hard to investigate pathology in single cell level. To overcome this limitation, single cell injury with the use of a laser makes it possible to apply a precise injury as small as single axon level and in *in vivo* scale [99, 100]. Time lapse imaging throughout the injury is important in single cell studies to determine the processes that initiates the spread of degeneration in a noninvasive way and provides valuable information about the whole process from start to end. Functional MRI, PET and 2p imaging are used to monitor neuronal activity [101]. 2p imaging achieves single-cell level in the highest resolution and imaging speed [102].

1.10. Aim of this Study

Neurodegeneration is a progressive and generally irreversible process that often spreads from degenerative site to neighboring healthy regions. Spreading of degeneration from primarily injured cells to the neighboring healthy cells is termed as transneuronal degeneration. It has been reported that purinergic signaling plays significant roles in traumatic injury and transneuronal degeneration, as well as neurodegenerative diseases including Huntington's disease (HD) and Parkinson's disease (PD). Our previous results with a single cell axotomy model in dorsal root ganglion (DRG) cell culture showed that purinergic signaling, particularly P2X7, had an important role in the spread of degenerative signal from injured cells to neighboring healthy cells. It is known that many neurodegenerative conditions exhibit a spreading-like behavior. Even though the symptoms, protein aggregation profile or time scale are

distinct across many neurodegenerative disorders, they may have a common spreading mechanism including synaptic connectivity, physiological relationship and anatomical localization.

Thus, in this study, we have hypothesized that (a) purinergic signaling is important in TND and may be a risk factor that plays a role in propagation rate and severeness in neurodegenerative conditions; (b) Elk-1 has a neuroprotective role in many neurodegenerative disorders such as PD and HD. To that end, we have implemented a cell culture model to investigate spread of TND in central nervous system (CNS) cells, as well as generated *in vitro* PD model where we studied gene expression patterns in response to neurodegeneration, identifying common pathways among different neurodegenerative conditions and investigated mHtt-cytoskeleton interactions as well as neuroprotective role of Elk-1.

Transcriptome based KEGG pathway analyses using 6-OHDA based PD model of SH-SY5Y and LUHMES cells revealed that common pathways existed among different neurodegenerative conditions. Basically, alterations in cellular transport, glutamatergic and purinergic signaling pathways are highlighted in many conditions. We used calcium imaging to determine variations in glutamatergic signaling pathway. Neurons responded similarly in terms of calcium activity in PD, HD or traumatic injury models. In all conditions, synchronized and increased calcium activity was observed. Additionally, we showed that Elk1 overexpression and knocking out P2X7 is neuroprotective in either HD and PD models and traumatic injury respectively.

2. MATERIALS and METHODS

2.1. Materials

2.1.1. Plasticware

Table 2.1: List of plasticware.

Reagents	**Supplier – Catalog No**
Centrifuge Tube (50 ml)	Nest - 602002
Centrifuge Tube (15 ml)	Nest - 601002
Microcentrifuge Tube (2 ml)	Nest - 620011
Ultracentrifuge tube	Beckmann - 361625
Glass bottomed petri dishes	WPI - FD35PDL-100
Amicon 100K column	Milipore - UFC910024
Petri dish (100mm)	Nest - 704004
Petri dish (150mm)	ThermoFisher - 168381
6-well plates	Corning - 3516
96-well plates	Corning - 3596
35 mm petri dishes	Thermo - 130180
T25 Flask	Nest - 707003
T75 Flask	Sarstedt - 83-3911-002
Cell scraper	Vwr - 10062-904

2.1.2. Plasmids

Table 2.2: List of plasmids.

Plasmid name	**Promoter**	**Description**
pEGFP	CMV	EGFP backbone
Q23-EGFP	CMV	EGFP tagged WT exon1 Htt
Q74-EGFP	CMV	EGFP tagged mutant exon1 Htt
EGFP-alphasynuclein-WT	CMV	EGFP tagged WT alpha Synuclein
EGFP-alphasynuclein-A53T	CMV	EGFP tagged mutant alpha Synuclein
pAAV.Syn.GCaMP6s.WPRE.SV40	Syn	GCaMP6s in AAV expression cassette
pLenti-Lifeact-tdTomato	CMV	Lifeact-tdTom in lenti exp. cassette
miniSOG-Vimentin-7	CMV	miniSOG tagged Vimentin
pHelper	CMV	Helper for AAV production
RepCap 2/1	CMV	RepCap 2/1 for AAV production
pCDNA3.1	CMV	Empty backbone
CMV-Elk1	CMV	Ubiquitious expression of Elk1
CMV-Elk1-S324A	CMV	Ubiquitious expression of phosphomutant Elk1
CMV-Elk1-S383A	CMV	Ubiquitious expression of phosphomutant Elk1
CMV-Elk1-T417A	CMV	Ubiquitious expression of phosphomutant Elk1
ElkVP16	CMV	Constitutively active Elk1 expression

2.1.3. Cell lines, Bacterial Strains and Mice Strains

Table 2.3: List of Cell Lines, Bacterial Strains and Mice Strains.

Cell line	**Supplier - Catalog No**
SH-SY5Y: human neuroblastoma cell line	ATCC - CRL-2266
LUHMES: Human dopaminergic cell line	Schildknecht Lab
LUHMES – aSyn – EGFP : Human dopaminergic cell line overexpressing aSyn	Schildknecht Lab
HEK293T: Human embryonic kidney cell line	ATCC - CRL-3216
AAV293: Human embryonic kidney cell line for AAV production	Cell BioLabs – AAV-100
Mice Strain	**Supplier - Catalog No**
C57BL/6J	Jackson Laboratories - 000664
B6.129P2-P2rx7 tm1Gab /J	Jackson Laboratories - 5576
Mapttm1(EGFP)Klt/J	Jackson Laboratories - 004779
Bacterial Strain	**Supplier - Catalog No**
DH5α	Invitrogen - 18265017
Stbl3	Invitrogen - C737303

2.1.4. Chemicals and Reagents

Table 2.4: List of chemicals and reagents.

Reagent	**Supplier – Catalog No**
1X PBS	Multicell - 311-010-CL
Trypsin-EDTA (0.05 %)	Capricorn – TRY-1B
DMSO	Sigma – D8418
MEM non Essential Amino Acids	Biosera - XC-E1154
FBS	Gibco - 10500-064
10X PBS	Multicell - 311-012-CL
OptiMEM	Gibco - 51985-034
PEI (Linear)	Polysciences - 23966-1
Lipofectamine 2000	Invitrogen - 11668027
OptiPrep	Sigma – D1556
DMEM high glucose	Gibco - 21969-035
Laminin	Sigma – L2020
L-15	Multicell – 323-050
RPMI 1640	Gibco - 21875-034
Neurobasal-A	Gibco - 10888-022
HBSS	Sigma – H9269
Percoll	Sigma – P4937
Antibiotic/Antimicotic	Multicell – 450-115-EL
GlutaMAX	Gibco – 35050-061
B-27	Gibco-17504-044
Collagenase	Sigma - C7657
Trypsin inhibitor	Biomatik - A5107
Papain	Sigma – P4762
DNase	Biomatik – A2442
LB Agar	Biomatik - A8523
LB Broth	Biomatik - A8521
Ampicilin	Biomatik – A2154
Kanamycin	Biomatik – A3102
Glycerol	Sigma - G8898

Table 2.4: Continued.

Benzonase	Sigma - E8263
D-sorbitol	Sigma – S1876
NaCl	Sigma - 31434
Trizma base	Sigma – T1503
$CaCl_2$	Sigma – C1016
KCl	Sigma – P9541
$MgCl_2$	Sigma – M8266
Phenol Red	Biomatik – A3616
OsO_4	EMS - 19180
Potassium Ferrocyanide	EMS – 26603-01
Uranyl acetate	EMS - 22400
L-Aspartic acid	Sigma -11189
Lead (II) nitrate	Sigma - 228621
Thiocarbohydrazide	Sigma - 223220
DAB	Sigma - 32750
Aminotrizole	Sigma – 8.14495.0100
Advanced DMEM:F12	Thermo Fisher - 12634028
Tetracycline	Sigma - T7660
N2 supplement	Thermo Fisher - 17502001
L-Glutamine	Thermo Fisher - 25030081
b-FGF	R&D - 233-FB
db-cAMP	Sigma - D0627
Poly-L-ornithine	Sigma – P-3655
Poly-D-lysine	Sigma - P7280
Poly-L-lysine	Sigma - P6282
Fibronectin	Sigma – F-1141
GDNF	R&D - 212-GD
DAPI	Sigma – D9542
Hoechst	Thermo - 62249
Propidium Iodide	Invitrogen - P3566
Safeview	Abm - G108

Table 2.4: Continued.

Protease/Phosphatase Inhibitor Cocktail	Cell Signalling - 5872
4x Laemli buffer	Biorad - 1610747
Phalloidin	Thermo – R415
RIPA buffer	Cell Signalling - 9806
Precision Plus Protein All Blue Prestained Protein Standard	Biorad - 1610373

2.1.5. Kits

Table 2.5: List of kits.

Product Name	**Supplier – Catalog No**
Endo-free MaxiPrep Plasmid Isolation kit	Qiagen - 12362
Epoxy embedding medium kit	Sigma - 45369
MiniPrep Plasmid Isolation kit	Ambrd - 10-13-01-50
MidiPrep Plasmid Isolation kit	Intron - 17251
iScript cDNA Synthesis Kit	Biorad - 1708890
iTaq Universal SYBR Green Mix	Biorad - 1725121
PureLink RNA Mini kit	Invitrogen - 12183020
TGX Stain-Free FastCast Acrylamide Kit	BioRad - 1610183
Trans-Blot Turbo Mini PVDF Transfer Kit	Biorad - 1704272

2.1.6. Antibodies

Table 2.6: List of antibodies.

1' Antibody	**Supplier – Catalog No**
Anti-Vimentin	Sigma - V5255
Anti-β-tubulin	Invitrogen - PA1-41331
Anti-β-III-tubulin	Novus – NB100-1612
Anti-Flag	Santa Cruz – sc7945
Anti-Huntingtin	Cell Signalling - 5656
Anti-Elk1	Santa Cruz – sc-365876
Anti-α-synuclein	Santa Cruz – sc-12767
Anti-β-actin	Cell signaling - 4970
Anti-GFAP	Cell Signalling – 3670S
2' Antibody	**Supplier – Catalog No**
Goat-anti-mouse -HRP	Santa Cruz - sc-2005
Goat-anti-rabbit-HRP	Santa Cruz - sc-2030
Anti-mouse-Alexa Plus 647	Invitrogen – A32728
Anti-chicken-Alexa 633	Life Technologies – A21103

2.2. Methods

The experimental flow of this thesis study is comprised of 3 main strategies: (i) *in vitro* Parkinson's Disease model studies, (ii) *in vitro* Huntington's Disease model studies, (iii) *in vitro* and *in vivo* modelling of TND. Parkinson's Disease model is obtained by two different cell lines (SH-SY5Y and LUHMES cell lines), and two different strategies (α-synuclein overexpression and 6-OHDA toxicity) (Figure 2.1). We have observed 6-OHDA-induced PD model to give more consistent results and was preferred for following experiments (microarray and RNASeq) in both SH-SY5Y and LUHMES cell model. Transcriptome analyses in these *in vitro* models have been performed and possible drug targets for drug repurposing have been determined. Efficacy of selected drugs have been tested and their neuroprotective effects were confirmed in both cell models. Additionally, neuroprotective effects of Elk-1 relative to drugs have been determined.

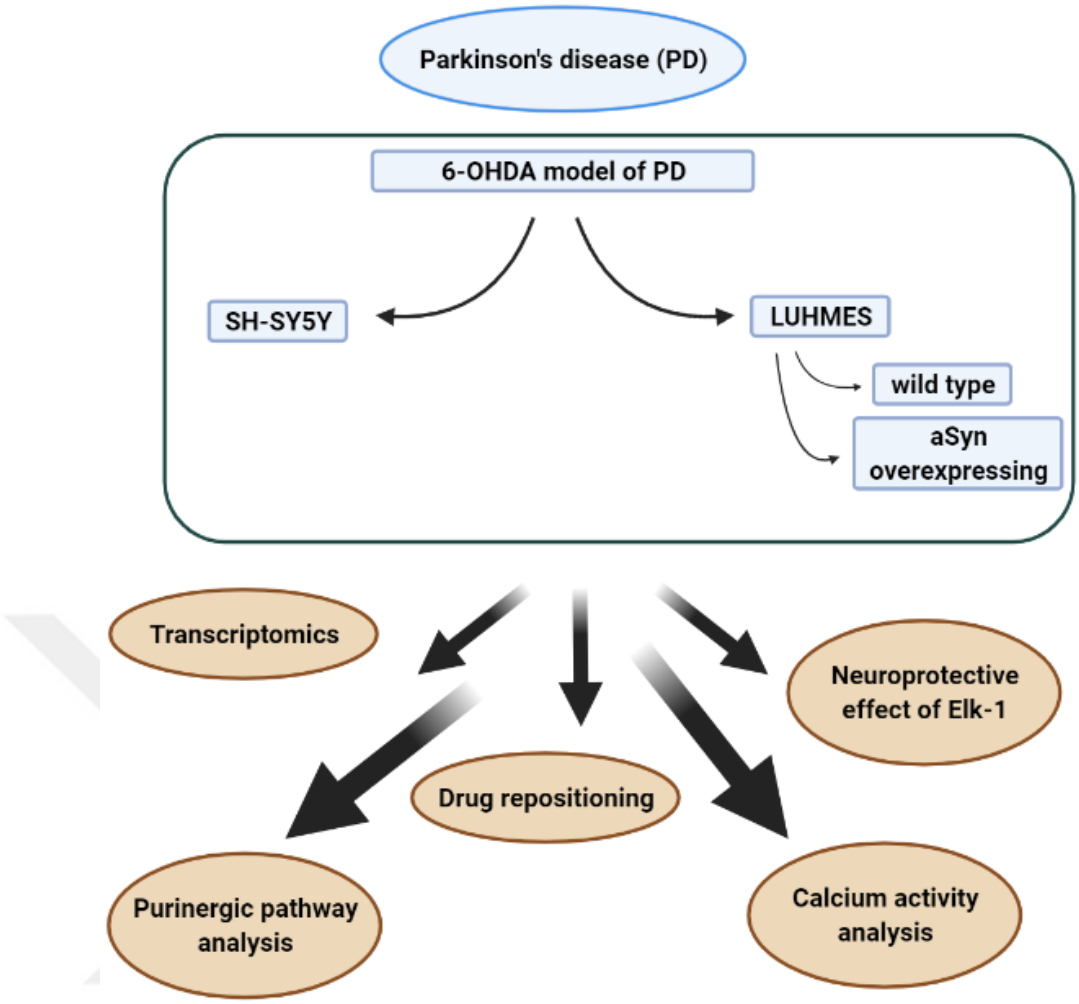

Figure 2.1: Experimental strategy 1.

Parkinson's Disease. Modelling of PD includes two different *in vitro* models obtained with 6-OHDA treatment and aSyn overexpression. Drug repositioning approach is performed after transcriptome analysis in both cell types. Neuroprotective effects of drugs and Elk1 is investigated.

Second strategy included an *in vitro* HD model by overexpressing mHtt in both HEK293T cells and primary neurons. mHtt aggregation was readily observed in both cell models, and the interaction of the mHtt aggregates with other cellular components such as mitochondria and cytoskeleton has been studied. Using advanced microscopy techniques (airy scan confocal, correlative electron microscopy, and live cell imaging) we have investigated interaction of mHtt with cytoskeletal element F-actin and contribution of Elk1 to the formation of aggregates, as well as its neuroprotective effect (

Figure **2.2**).

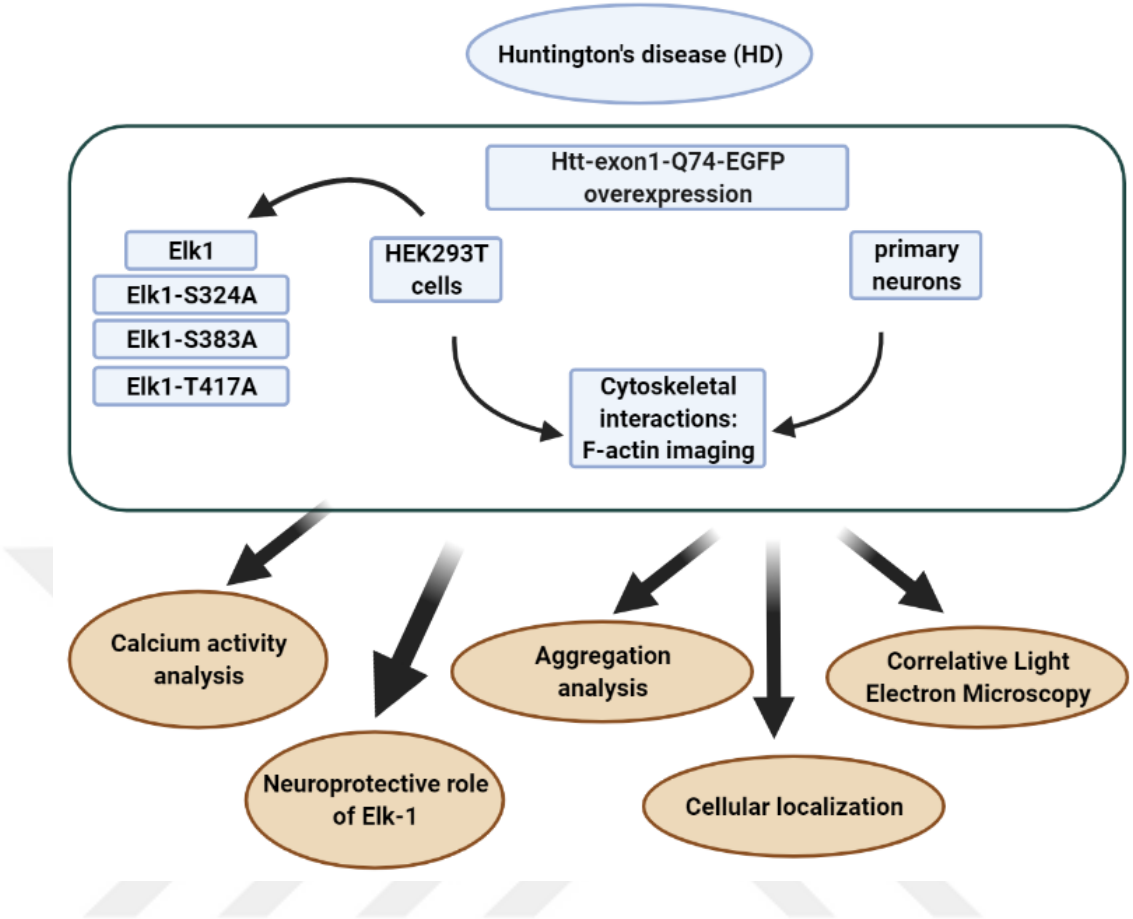

Figure 2.2: Experimental strategy 2.

Huntington's Disease. HD is constructed using both HEK293T cells and primary neurons. Interaction of mHtt with cytoskeletal components are investigated together with effect of Elk1 in aggregate formation.

Third experimental strategy of this thesis focused on investigating traumatic injury and TND through *in vitro* and *in vivo* models. DRG and hippocampal neurons were used as model cells and spread of injury from single cell to surrounding healthy neurons has been investigated in terms of calcium activity and cell death. Effects of P2X7 receptor and calcium was investigated in healthy cells in response to an injured neuron nearby (

Figure **2.3**).

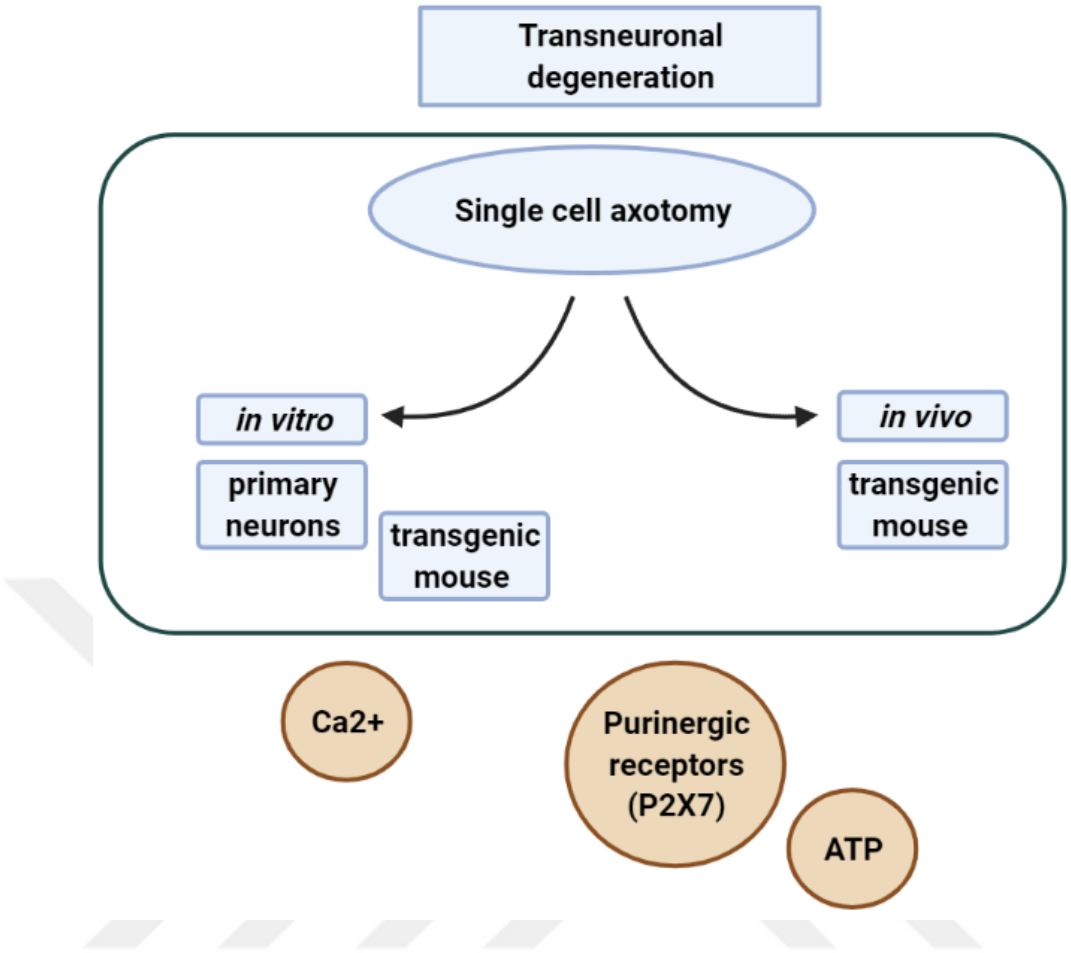

Figure 2.3: Experimental strategy 3- *In vitro* and *in vivo* TND model. Primary neuron cultures and transgenic mice with tagged neurons are used for *in vitro* and *in vivo* modelling of TND respectively. Role of calcium and purinergic signaling are investigated in spread of traumatic injury induced toxicity.

2.2.1. Cell lines

HEK293T and SH-SY5Y cells are maintained in T75 flasks with high glucose DMEM supplied with 10% FBS and 1% Penicilin/Streptomycin in physiological conditions (37^{o}C, 5% CO_2). Culture medium is replaced every 3 day and cells are passaged at 70%-90% confluency. For passaging, old medium is removed and cells are washed with 5 ml sterile 1x PBS following 0.05 % trypsin-EDTA incubation for 3 minutes at room temperature. After cells were detached, trypsin is inhibited with 10 ml complete medium and cells are harvested by centrifugation at 300 g for 5 minutes. Cells are counted by hemocytometer and seeded into 96-well plates as 30.000 cells in each well for viability analysis. For microarray, western blot and RT-PCR

experiments, cells were seeded in 100 mm petri dishes as $2x10^6$ cells each or 300.000 cells in each well of 6-well plates. Frozen cells are stored in -80 freezer for short time and liquid nitrogen for longer periods in freezing medium (complete DMEM containing 10% DMSO).

Wildtype or mutant aSyn-overexpressing LUHMES cells are kind gifts from Stefan Schildknecht Lab, Germany. LUHMES cells are seeded in poly-L-ornithine/fibronectin coated flasks and maintained in proliferation medium (DMEM:F12 supplemented with L-glutamine (2 mM) 40 ng/ml b-FGF and 1% N2 supplement) in T75 flasks. Protocol established in the originator laboratory (Schildknecht Lab) is followed for differentiation [103]. Briefly, when the cells reached 75% confluency, proliferation medium is removed and cells are washed with sterile 1x PBS following incubation with 0.05% trypsin-EDTA for 1-2 min at 37ºC. Detached cells are resuspended in DMEM:F12 and harvested by centrifugation at 300 g for 5 minutes. Cells are counted with hemocytometer and $4x10^6$ cells are seeded into poly-L-ornithine/fibronectin coated T75 flasks with proliferation medium for pre-differentiation (day 0). Cells are allowed to adhere to surface for 24 hours and proliferation medium is replaced with differentiation medium (DMEM:F12 containing L-glutamine (2 mM), N2 supplement (1%), GDNF (2 ng/ml), dbcAMP (100 µm), tetracycline (1 µg/ml)). Cells are incubated further in T75 flask for 48 hours and detached as described previously. Cells were seeded with differentiation medium as 1.5×10^6 in each well of 6-well plate, 50.000 in each well of 96-well plate and 6×10^6 in each 100 mm petri dishes for western blot and RT-PCR assays, viability assay and RNASeq analysis respectively. After 48 hour of incubation, differentiation medium is renewed (day 4) and differentiation is completed after additional 48 hours (day 6).

2.2.2. Primary Neuron Culture

Primary hippocampal and cortical neuron culture:

Glass bottomed petri dishes are coated with poly-L-lysine for 2h at room temperature, washed twice with sterile dH2O and air-dried prior seeding the cells. Newborn p0-p3 mice are sacrificed using cervical dislocation and hippocampus and/or cortex is dissected in dissection medium (L-15 medium supplied with 1% Penicillin/Streptomycin and 1% GlutaMAX). Dissected hippocampus and/or cortex is incubated at 4 C with 1% Papain in dissection medium. 1% DNase is added to the

papain mix and tissue is triturated with fire polished Pasteur pipettes with decreasing diameters three times to obtain single cells. Enzyme activity is inhibited by transferring triturated cells to dissection medium supplemented with 10% FBS and incubated at + 4 ^{o}C for 15 min. Cells are centrifuged at 1000 rpm for 5 min, supernatant is discarded and cell pellet is resuspended in culture medium (NBA medium supplied with 1% GlutaMAX, 1% Penicillin/Streptomycin, 2% B-27).

Primary DRG neuron culture:

One day before cell culture, 35 mm glass-bottomed petri dishes ae marked with the UV laser attached to confocal microscope. The marked petri dishes are coated with 1% poly L lysine at room temperature for 2h. At the end of the period, 150 µl of 1% Laminin is added to the petri dishes that are washed 2 times with sterile ddH2O and kept at 37°C overnight. Petri dishes are washed prior to cell seeding and air dryed. Transgenic and/or C57 mice are sacrificed by CO2 aspiration method. To prevent contamination, mouse is washed with 70% EtOH prior to surgical operations. The ribs are carefully dissected without damaging the DRGs and washed once with sterile ddH2O, and then taken into the dissection medium on the cold plate. 35 (+5, -5) DRGs are separated from the ribs by cutting their peripheral and central extensions under a 0.5x stereo microscope (Carl Zeiss).

DRGs are incubated in NBA medium containing 1% Type I collagenase at 37 °C, 5% CO2 for 40 minutes. At the end of the incubation, collagenase is removed by washing 3 times with 1 ml of HBSS carefully, and 500 µl of 10x Trypsin EDTA in NBA medium is added and incubated for 15 minutes at 37 °C, 5% CO2. Later, 1% DNAse I is added to the tube and DRGs are gradually triturated with 1000 µl pipette tip, 200 µl pipette tip and finally 2 insulin needles until the tissue was homogenized (~10 minutes). Then, isolated cells are incubated in 37 °C 5% CO2 for 30 mins. At the end of the incubation period, Trypsin EDTA and DNAse are removed by centrifugation at 1000 rpm for 3 minutes and the cells are resuspended in NBA medium containing 10% FBS and 6% Trypsin inhibitor. Percoll layers of 60%, 35% and 10% are prepared, respectively, and the cells are carefully added to the top layer and centrifuged at 1700 rpm for 20 minutes. DRG neurons are between the 60% and 35% layers. ~750 µl of Percoll/medium mixture is collected between 60% and 35% layers and washed by adding 3 ml of NBA, the cells are counted and seeded in on the coated

petri dishes, with 1500 – 2000 neurons in each petri dish. After the cells adhered, the media is completed up to 1.5 ml.

2.2.3. *In vitro* Single Cell Axotomy and Simultaneous Imaging

For *in vitro* modelling of traumatic injury, primary hippocampal cells were used. Hippocampal cells were isolated from newborn (p0-p2) mice and seeded into glass bottomed petri dishes (500k cell each). Cells were transduced with AAV-Syn-GCaMP at div2. After GCaMP expression was started and neural network established (div7-div10), cells were imaged with confocal microscope using 40x/1.3 Plan Apochromat oil objective and 488 nm laser for spontaneous calcium activity (before axotomy). Then, single cell axotomy was performed in each well of primary neuron cultures using a 355 nm UV Laser (Rapp Optoelectronic), and both axotomized and neighboring cells were imaged simultaneously.

For RT-PCR experiments, hippocampal cells are cultured and maintained for 10 days in cell culture to neuronal network to be matured. Total of 50 single-cell axotomies were performed in a single petri dish and all cells were collected 24h post axotomies.

2.2.4. *In vivo* Single Cell Injury and Simultaneous Imaging

For investigating TND in *in vivo* conditions, a dorsal root ganglion (DRG) live imaging model of mice using 2-Photon microscopy was utilized. 6–8-week-old β-III-Tubulin-EGFP mice (Mapttm1(EGFP)Klt/J – Jackson Laboratories, #004779) were anesthetized with isoflurane during the surgery. After animals were deeply anesthetized, PI (5 mg/kg) was injected through tail intravenously. A dorsal skin incision was made to beneath the thorax level of mice. Fascia was removed carefully and muscles were separated gently (Figure 2.4). L3 or L4 ganglia was exposed and residual tissue on DRG was removed carefully. Exposed DRG was stabilized on a stage with a homemade L shaped metal plate to minimize motion arises from breathing or heartbeat of animal (

Figure 2.5).

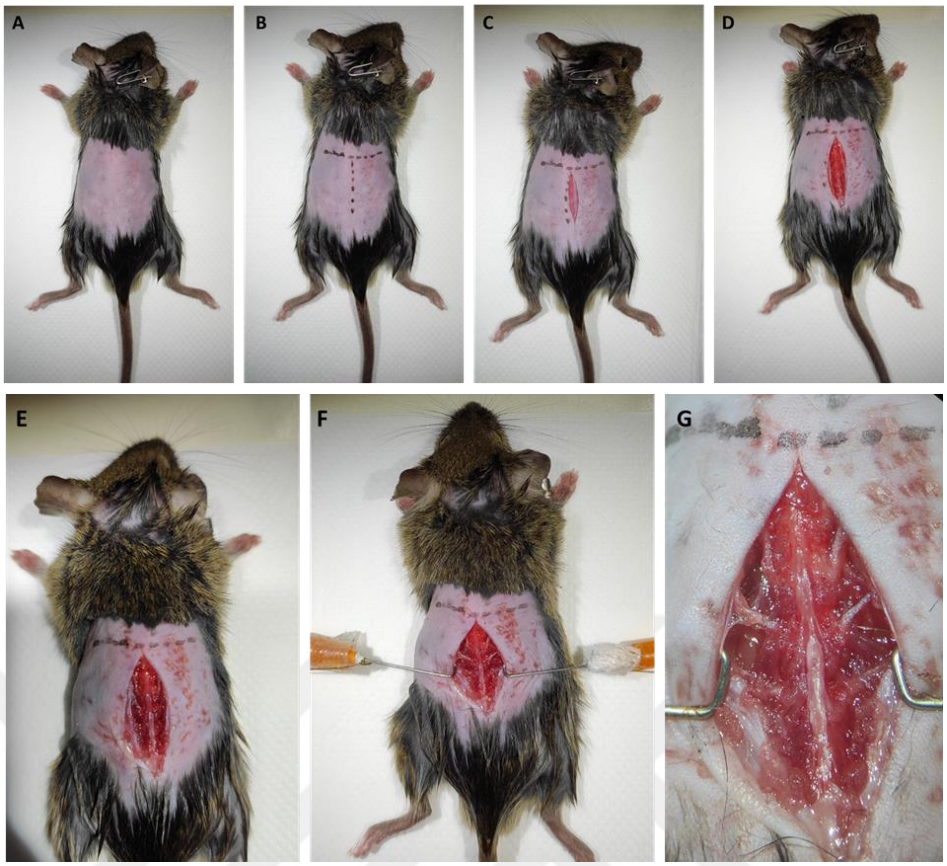

Figure 2.4: Step by step (A – G) surgical procedure for in-vivo DRG imaging.

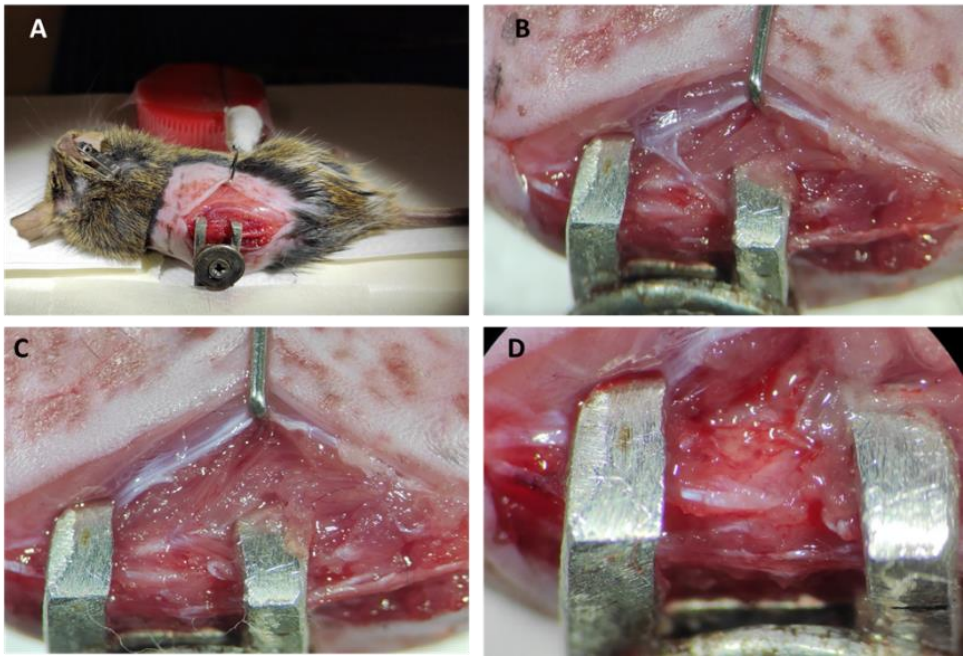

Figure 2.5: Surgical procedure for stabilizing mice using metal holder and exposing DRG.

DRG was imaged with Zeiss 7 MP microscope (Carl Zeiss, Jena, Germany) equipped with dual Ti:Sapphire multiphoton lasers (Coherent Chameleon Vision II and Ultra, Coherent, Santa Clara, CA). 820 nm wavelength was used for imaging. EGFP, PI and backward Second Harmonic Generation (SHG) signals (used for collagen of capsule of DRG) were simultaneously acquired using a 10x/0.4 NA Plan-Apochromat dry objective, image sizes were 1024×1024 pixels, Z stack images covering whole DRG were acquired with a z-step size of 2.8 um. Z stack image of whole DRG was taken before injury. Single cell injury was performed using femtosecond laser at 820 nm and 100 % power. Images were taken right after, 1h and 4h after injury. After 4h time period, muscles and skin were sutured and same position of DRG was imaged 24h after injury.

2.2.5. Competent Bacteria Preparation

DH5α and Stbl3 bacterial strains are used for plasmid amplification. Both strains are made competent using the same protocol. Briefly, a single bacteria colony is selected and inoculated in 100 ml LB Broth until OD600 value gets to 0.4. Then, bacteria are pre-cooled in ice for 10 min and centrifuged at 2700 g for 10 min at 4 ºC at separate 50 ml tubes. Supernatant is discarded, pellet in each tube is resuspended in 1.6 ml ice cold 100 mM $CaCl_2$ and incubated on ice for 30 min. After incubation cells are centrifuged at 2700 g for 10 min at 4ºC. Supernatant is discarded and cell pellet is again resuspended in 1.6 ml ice cold 100 mM $CaCl_2$ followed by 20 min incubation on ice. Cells are combined in one tube and 0.5 ml ice-cold 80% glycerol is added. Freshly prepared competent bacteria is aliquoted in small amounts (50 – 100 µl) and each aliquot is snap frozen in liquid nitrogen for further use.

2.2.6. Bacterial Transformation and Plasmid Isolation

Plasmids are transformed into competent bacteria for amplification. DH5α strain is used for transformation of expression plasmids. Stbl3 strain is used for AAV expression, helper or rep/cap plasmids. 20ng – 100 ng plasmid is added to 100 µl of competent bacteria and incubated on ice for 30 min. Transformation is done by heat shock applied in 42ºC for 60 sec followed by a 5 min incubation on ice. 900 µl antibiotic free LB Broth is added to bacteria and incubated for 1h-2h at 37ºC with shaking on 125 rpm. 300 µl of bacteria is spread onto agar plates with specific

antibiotics and incubated at 37ºC for overnight. A single bacterial colony is selected and inoculated in 300 ml LB Broth with the appropriate antibiotic for overnight. Bacteria is collected with centrifugation at 4000 g for 20 min at 4ºC and plasmid isolation is done using MaxiPrep plasmid isolation kit according to the manufacturer's instructions.

2.2.7. AAV Production and Titration

AAV293 cell line is used for AAV production. Cells are maintained in high glucose DMEM containing 10 % FBS and 1 % NEAA. A total of 12 x 15 cm petri dishes were prepared for each AAV prep. Cells are cotransfected with Transfer, Helper and RepCap plasmids with 1:4 plasmid:PEI ratio when reached to 70 % confluency. Cells are collected with cell scraper 72h post transfection and pelleted by centrifugation at 300 g for 5 min. Cell pellets are resuspended in 9 ml sterile lysis buffer (150 mM NaCl, 20 mM Tris, pH:8) and lysed with 3x freeze-thaw cycles in liquid nitrogen/37ºC heat bath followed by sonication (30 sec ON, 15 sec OFF) for 5 min. 10 µl 1M $MgCl_2$ and 10 µl Benzonase (250K U) is added to lysed cells and incubated at 37ºC with shaking (~170 rpm) for 20 min. Cell debris is pelleted with centrifugation at 4000 rpm for 20 min at 4ºC. Supernatant is ultracenrifuged through iodixanol gradient (17 %, 25 %, 40 %, 60 %) at 55.000 rpm for 2.15 h at 4ºC. AAV is collected from 40 % fraction. Iodixanol is removed and AAV is concentrated in storage buffer using 100K columns for 3x centrifugation at 3500 rpm for 30 min at 4ºC. Concentrated AAV particles are aliquoted and stored at – 80 for further usage. AAV titer is calculated using absolute quantification method via qRT PCR. WPRE forward and reverse primers were used for amplification and pAAV-Syn-GCaMP6s-WPRE-SV40 plasmid is used to construct standard curve.

Table 2.7: Forward and Reverse Primer Sequences.

	Forward Primer	**Reverse Primer**
WPRE	GGCTGTTGGGCACTGACAAT	CCGAAGGGACGTAGCAGAAG

Table 2.8: RT PCR Reaction Mix.

Component	**Volume (µl)**
d H_2O	5
Forward primer (10)	0.5
Reverse primer	0.5
iTaq Universal SYBR Green Supermix (2x)	10
AAV	4

Table 2.9: RT PCR Protocol.

Temperature	**Time (s)**
95 ^oC	30
95 ^oC	5
60 ^oC	5
Repeat from step 2 for 40x	
65 - 95 ^oC (0.5 ^oC increments)	5s /step

2.2.8. Transient Transfection of Cells

HEK293T cells are transfected when reached to 50-70% confluency using 1:4 plasmid:PEI ratio. A total of 10 µg is used for 100 mm petri dishes and plasmid amount is changed proportionally to growth area. Briefly, 10 µg plasmid and 40 µg PEI are mixed in 1 ml serum-free medium, pulse vortexed for 15 times and incubated at room temperature for 15 minutes to obtain plasmid:PEI complex and added drop wisely to cells. Cell culture medium is refreshed after overnight incubation.

SH-SY5Y and primary cells are transfected using Lipofectamine 2000 in 1:3 plasmid:lipofectamine ratio. Briefly, 2.5 µg plasmid and 7.5 µg lipofectamine are added to 100 µl serum-free medium in separate tubes, combined afterwards and pulse vortexed for 15 times. After 15 minutes of incubation in room temperature, mixture is added dropwise to cells and medium is refreshed after overnight incubation.

2.2.9. Western Blot

SH-SY5Y and LUHMES cells are washed with ice-cold PBS, scraped and incubated with RIPA buffer containing 1x protease-phosphatase inhibitor on ice for 30

minutes followed by centrifugation at 14000g at +4ºC for 15 minutes. Supernatant is collected and proteins are quantified using Bradford assay. Proteins are denatured and reduced in 4x laemli buffer including β-merchaptoethanol at 95ºC for 5 minutes. SDS-PAGE gel is prepared using Biorad TGX Stain-Free FastCast Acrylamide Kit (10%). 20 µg protein is loaded in each well and gel is run at 80V for half an hour and at 100V for 45 minutes. SDS gel and MetOH activated PVDF membrane were sandwiched in transfer buffer and transfer of proteins was carried out using Transblot transfer device (BioRad). The membrane washed with TBS-T and blocked with 5% skimmed milk at room temperature for 1 hour and treated with primary antibodies (1: 1000, mouse anti-β-actin, mouse anti-aSyn) diluted in 5% BSA at +4 C overnight. After incubation, the membrane was washed 3 times for 5 minutes with TBS-T and incubated with secondary antibodies (1: 3000, HRP anti Mouse) diluted in 5% BSA for 1 hour at room temperature. After 1 hour, the membrane was washed 3 times for 10 minutes with TBS-T and visualized with ECL using ChemiDoc (BioRad) device. Protein band intensities were measured using Gel Analyzer Plug-in in ImageJ and normalized against β-actin.

2.2.10. RT-PCR

RNA isolation from cells were performed as described in the protocol provided by manufacturer (Ambion PureLink RNA Mini Kit). RNA concentrations were measured using Nanodrop. cDNA was synthesized from 1ug of each RNA sample using iScript cDNA Synthesis Kit (BioRad) according to manufacturer instructions (Table 1). Gene expression changes were determined for PD-related genes and microarray validations with RT-qPCR using iTaq Universal SYBR Green Supermix (BioRad) and BioRad CFX Connect. RT-PCR reaction setup and PCR protocol were applied according to manufacturer instructions (Table 3, Table 4). $2^{-\Delta\Delta Ct}$ values were calculated and fold changes were determined compared to control samples (RT-PCR experiments were performed by Ekin Sönmez).

Table 2.10: cDNA Synthesis Reaction Mix

Component	Volume (µl)
iScript Reaction Mix (5x)	4
iScript Reverse Transcriptase	1
RNA Template (1 µg)	Based on concentration
Nuclease-free dH_2O	up to 20 µl
Total volume	20

Table 2.11: cDNA Synthesis Protocol

Temperature	Time (min)
25ºC	5
46ºC	20
95ºC	1
4ºC	hold

Table 2.12: RT PCR Protocol

Temperature	Time (s)
95ºC	30
95ºC	5
60ºC	30
Repeat from step 2 for 35x	
65 - 95ºC (0.5ºC increments)	5s/step

2.2.11. Cell Viability Analysis

SH-SY5Y cells were seeded on 96-well plates (30.000 cell each well) with 10 % FBS containing DMEM and maintained for 48h. Then, cell medium was changed to 1 % FBS DMEM 3h prior to treatments and treatments were conducted as three different conditions as stated in drug/6-OHDA timeline (Figure 2.6).

Figure 2.6: Timeline of 6-OHDA and drug treatments.
SH-SY5Y cells are treated with determined drugs before, after or at the same time with 6-OHDA application. Afterwards, cells are stained with Hoechst/PI and imaged for cell viability analysis.

At the end of each treatment, cells were treated with Hoechst/PI and incubated at 37^{o}C, 5 % CO2 for 10 min before imaging. Hoechst stains both live and dead cells while Propidium Iodide (PI) is only permeable to dead cell nucleus. For each well, 5x5 tile images consisted total of 25 frames were taken using 10x objective and COLIBRI Led Lights 385 nm (for Hoechst) and 543 nm (for PI) with Zeiss Axio Cell Observer microscope. For analysis of each images, Fiji (ImageJ) was used. A macro was written in order to convert data into 8-bit binary image and Gaussian Blur filter was applied for automated selection tool to work properly for measuring Hoechst+ and PI+ cell areas in each group (Figure 2.7, Figure 2.8). Then, total cell death percentages were calculated using the equation: (PI+ area) / (Hoechst+ area) * 100.

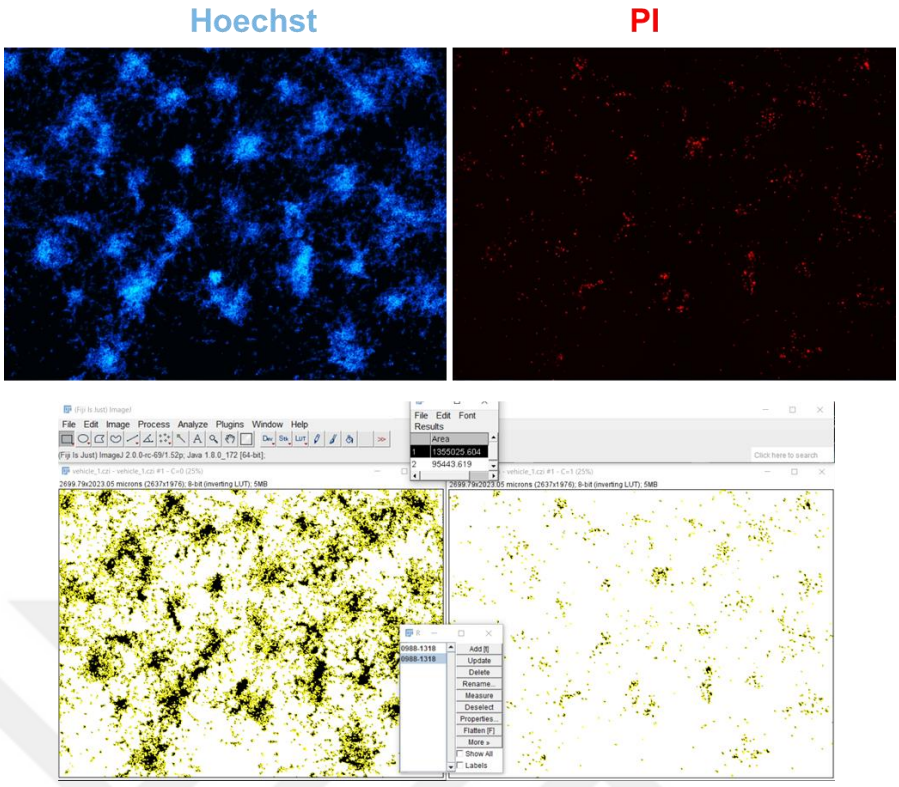

Figure 2.7: Implementation of image processing and automated selection in Fiji software.

Hoechst and PI images are converted into binary images for automated selection.

```
setOption("ScaleConversions", true);
run("8-bit");
//run("Brightness/Contrast...");
run("Enhance Contrast", "saturated=0.35");
run("Apply LUT");
run("Gaussian Blur...", "sigma=2");
setAutoThreshold("Default dark");
//run("Threshold...");
setOption("BlackBackground", false);
run("Convert to Mask");
run("Create Selection");
roiManager("Add");
```

Figure 2.8: Macro used in Fiji for automated selection of live and dead cells.

Batch processing of images are performed by macro that is able to adjust, convert to binary and select cell nuclei automatically.

Effects of Elk-1, WT and A53T mutant aSyn overexpression were investigated in PD. For this purpose, SH-SY5Y cells were seeded into 96-well plates and transfected with either pcDNA3, Elk1-VP16, p-EGFP, aSyn-WT-EGFP and aSyn-A53T-EGFP plasmids using Lipofectamine 2000. At 48h of transfection, cell medium was changed to 1 % FBS containing DMEM for 3h and cells were treated with 6-OHDA for 12h and 24h (

Figure **2.9**). Same image processing method was used for measuring cell death in these cells.

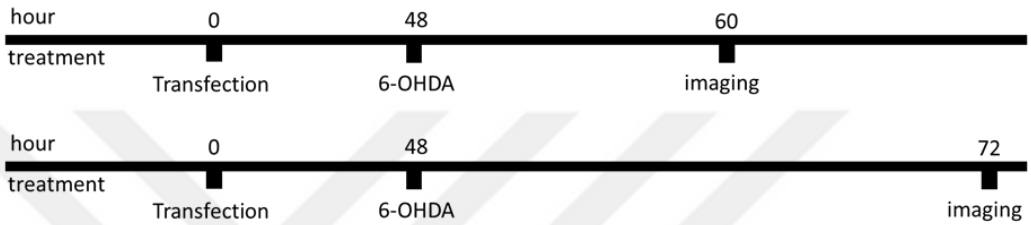

Figure 2.9: Timeline of transfections and 6-OHDA treatment.
SH-SY5Y cells are transfected with plasmids 48h before 6-OHDA treatment. Viability analysis is performed at 12h or 24h of 6-OHDA application.

Differentiated dopaminergic LUHMES cells were used for PD model. Wild type and aSyn overexpressing LUHMES cells were seeded on 96-well plates and differentiated as described in the previous thesis progress report. Differentiated LUHMES cells were treated with different concentrations of 6-OHDA and cell viability was determined by the same processing method applied for SH-SY5Y cells. As Quercetin and Rutin were found to significantly decrease cell death in SH-SY5Y cells, LUHMES cells were treated with Quercetin and Rutin prior to 6-OHDA treatment and cell viabilities were determined.

2.2.12. Aggregate Analysis

Subcellular localizations of mHtt aggregates are analyzed by segmentation. EGFP tagged mHtt expressing cells are stained with Hoechst and high resolution 3D Z stack images are taken using confocal microscopy by 40x/1.4 oil immersion objective. Segmentations were performed for aggregates or nuclei separately.

Quantifications of nuclear and cytoplasmic mHtt aggregates are performed using these segmented images and results are confirmed by confocal images (**Figure 2.10**).

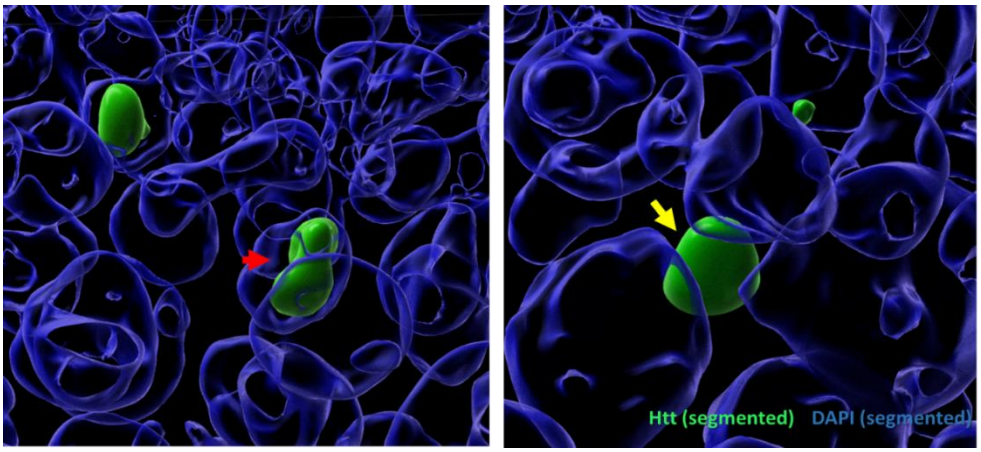

Figure 2.10: Segmentation of mHtt aggregates and nuclei in HEK293T cells. Transparent blue surfaces refer to nuclei; green surfaces refer to mHtt aggregates. Nuclear aggregate is depicted with red arrow; cytoplasmic aggregate is depicted with yellow arrow.

2.2.13. Transcriptome Analysis

For obtaining a neurotoxin based PD model, SHSY5Y cells are used. $2x10^6$ cells are seeded with complete medium on 100 mm plates. After 48h, culture medium is changed to 1%FBS complete medium (low-serum medium) and cells are incubated for 3h. After incubation, cells are treated with 6-OHDA and vehicle controls. At 12 and 18h of treatment, medium is discarded and cells are collected for RNA isolation. For RNA isolation, Agilent Micro Prep RNA Isolation kit is used according to manufacturer instructions. RNA concentrations are measured using Nanodrop and RNA integrity numbers were determined and Microarray analysis is performed according to Agilent One-Color Microarray-Based Gene Expression Analysis instructions.

Spike-In and RNA mixtures are prepared according to the protocol of RNA Spike-In One-color kit as the internal control of microarray study. Serially diluted Spike-In mixture is prepared for each sample with a maximum volume of 3.5 µl and RNA of approximately 200ng. Prepared Spike-In – RNA mixtures are combined with T7 Primer and denatured at 65ºC for 10 minutes. After denaturation, cDNA synthesis mixture is prepared and cDNA is synthesized by incubation at 40ºC for 2h followed

by incubation at 70ºC for 15 minutes. Afterwards, the transcription mixture required for cRNA synthesis is added into synthesized cDNA mixture and incubated for 2h at 40°C for cRNA synthesis and simultaneous labeling of the cRNA with the Cy3 fluorescent probe. Labelled cRNAs are isolated using Agilent Absolute RNA Nanoprep Kit according to the manufacturer's instructions. Concentration and Cy3 irradiation of the cRNAs were measured with the Nanodorop. cRNA efficiency and specific activities are calculated according to the concentration of dye, and the sample amounts to be used for hybridization are determined according to these results. Firstly, components are mixed and incubated at 60ºC for 30 minutes to fragment the RNAs. Then, samples are incubated on ice for 5 min and 25µl of 2x Hi-RPM Hybridization solution is added for termination of the fragmentation process. The samples are centrifuged for 1 minute at room temperature. The prepared mixture is placed on slides and the slide containing the probe is closed on them. The samples are incubated for 17 hours at 65ºC for hybridization.

Transcriptome analysis in LUHMES cells are performed by RNASeq analysis. Differentiated LUHMES and LUHMES-aSyn cells are treated with 50 µM 6-OHDA for 12h and collected for RNA isolation. RNA isolation is performed by the manufacturer's instructions. RNA integrity (RIN) values are measured and library preparation is performed for analysis.

Bioinformatics analysis is performed in Çakır Lab. Genes with higher than 1.70-fold changes and higher betweenness centrality values were considered as targets for drug repositioning. After literature survey, a total of 5 drugs were selected, effective concentrations were calculated and main stocks were prepared with DMSO.

2.2.14. Immunocytochemistry

Culture medium of cells in glass bottomed was removed and cells were washed with 1x PBS and incubated with 4 % PFA for 15 min at room temperature. PFA was discarded and cells were washed with 1x PBS again. Then, cells were blocked with blocking solution (1x PBS containing 3 % BSA, 1 % goat serum) for one hour at room temperature. Then, primary antibodies are added and incubated for overnight at 4ºC. After primary antibody incubation, cells were washed with 1x PBS for three times and incubated with secondary antibodies for 1 h at room temperature. Then, cells were washed with 1x PBS for five times 3 min each and imaged with confocal microscope.

2.2.15. Correlative Light and Electron Microscopy

To determine the morphological characteristics of Htt aggregates, correlative light electron microscopy (CLEM) was used and scanning transmission electron microscopy (STEM) images were taken according to confocal images of aggregates. Firstly, cells were fixed using Karnovsky fixative for 24h in 4^{o}C. Nuclear or cytoplasmic aggregates were identified using confocal microscope and UV laser branding was applied to the bottom of glass petri dishes to mark and number aggregates (Figure 2.11). High resolution Z-stack images were taken using 40x/1.3 oil immersion objective for further identification and correlation.

After regions of interest were determined, miniSOG photooxidation was done according to the protocol in [104]. Briefly, cells were incubated in blocking buffer for 30 min and freshly prepared chilled DAB solution was added. Cells were illuminated with 488 nm LED light (Colibri) using 40x oil objective for 1-2 min depending on the photo oxidation mainly observed by the brown reaction product in transmitted light.

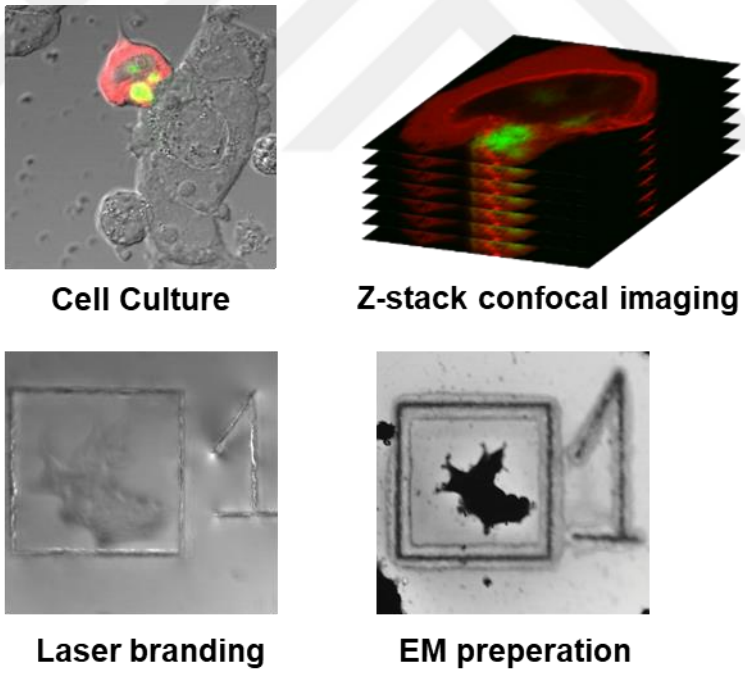

Figure 2.11: Laser branding on glass petri dish and epon block.
Cells with mHtt aggregates are localized under confocal microscope and Z-stack images are taken. Afterwards laser branding is applied to bottom of glass dishes. Cells are prepared for EM imaging and epon blocks are laser branded from the same localizations for trimming before ultrathin sectioning.

After laser branding, cells are washed with dH_2O and post fixed with reduced osmium (2% OsO_4, 1.5% Ferrocyanide) for 30 min at room temperature and were washed three times with dH2O and treated with 0.5% Thiocarbohydrazide for 15 min at room temperature. Then, cells were treated with 2% OsO4 for 30 min at room temperature, washed three times with dH_2O and incubated with 2% Uranyl Acetate at 4^oC overnight. Next day, uranyl acetate was removed and cells were treated with Lead Aspartate for 25 min at 60^oC. Then, lead aspartate was discarded and cells were washed thoroughly with dH2O five times. Afterwards, dehydration was done using 50 %, 70 %, 90 % and 100 % (x2) EtOH for 10 min each. Epoxy embedding medium (Sigma) was diluted with 1:1 and 2:1 in EtOH and cells were treated with these mixtures for 1h at room temperature. Lastly, pure epoxy embedding medium was poured over cells and incubated at 60^oC until epon polymerization was completed (24h).

After sample preparation for EM, cells appeared black and fluorescence signal could not be detected. So, laser brandings on glass petri was used as a reference and same laser brandings were applied on epon blocks (Figure 2.11). After branding, epon blocks were removed from glass petri using liquid nitrogen / 37^oC cycles until epon blocks detached from glass. Using stereo microscope, laser brandings on epon blocks were detected and trimmed using razorblade.

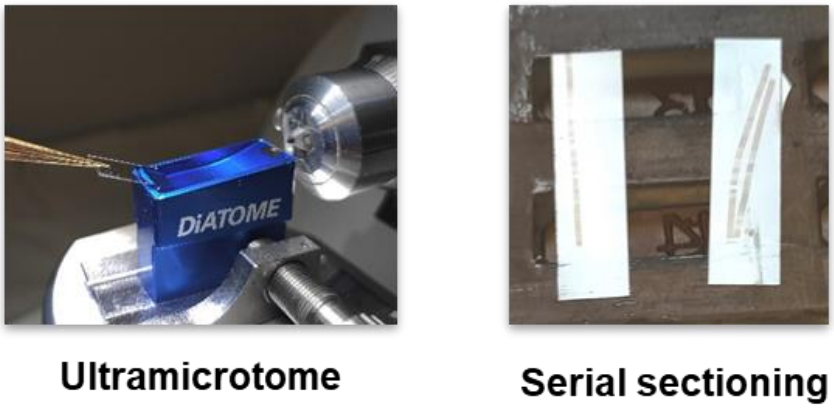

Figure 2.12: Laser brandings and numberings on epon block.
Diamond knife for ultrathin sectioning. Serial ultrathin sections are visible on Gold/Palladium ion coated hydrophilic cover glasses.

2.2.16. Array Tomography

Marked epoxy blocks were trimmed according to the ROI marks and 60 nm serial sections were taken using ultra microtome (Leica EM UC7) with a diamond knife (Diatome). (Figure 2.12) Cover glasses were manually cut into small pieces and fire-polished. Serial sections were collected onto cover glasses and coated with gold with sputter current 30 mA for 5 seconds (Leica EM ACE200). Cover glasses were sealed on aluminum stabs using carbon tape. Electron microscopy images were taken with Zeiss GeminiSEM 500 using 3.00 kV accelerating voltage and backscatter electron detector with 6.00 K X magnification and 4096 x 3072-pixel resolution. EM images were taken for total of 150-200 sections (70 nm each) using Zeiss GEMINI Electron microscope. 3D image construction was done using ImageJ, and Photoshop softwares (Figure 2.13).

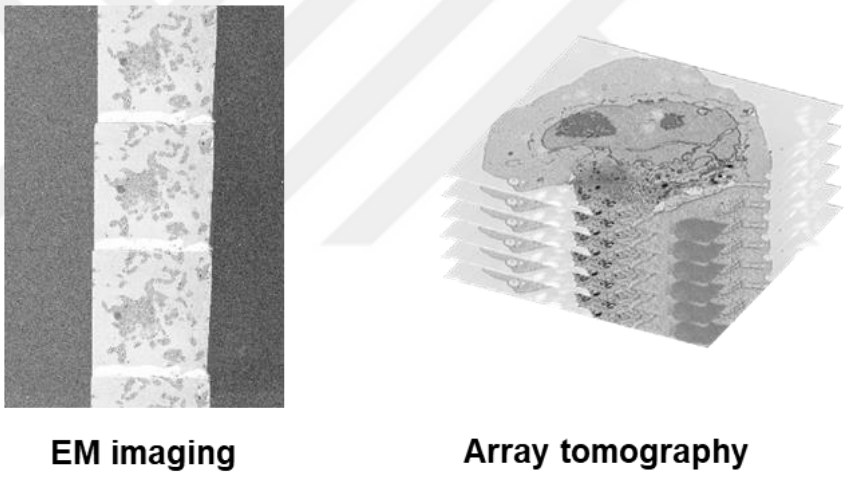

Figure 2.13: Serial ultrathin sections.
Serial sections on Gold/Palladium ion coated hydrophilic cover glasses are imaged with BSD detector. Array tomography images are constructed.

2.2.17. Statistical Analysis

All statistical analyses were performed using GraphPad Prism software. Student t-test was used to calculate statistical differences between each experimental group. Co-localization was determined using Pearson correlation analysis.

3. RESULTS

3.1. Parkinson's Disease

In line with our hypothesis that Elk-1 has neuroprotective function in neurodegenerative diseases, we have initially focused on choosing and validating the best *in vitro* PD model. To that end, different models have been utilized and the best one is selected for further experiments. We have then used these models to carry out transcriptome analysis for drug repurposing experiments in collaboration with Assoc. Prof. Tunahan Çakır from GTU Department of Bioengineering, and Ekin Sönmez from GTU Institute of Biotechnology.

3.1.1. Modelling PD in SH-SY5Y cells

3.1.1.1. Overexpression of wild-type and mutant α-synuclein

Various *in vitro* PD models rely on the overexpression of mutant aSyn in cells, resulting in aSyn aggregates and cell death. Therefore, we have obtained plasmids encoding wildtype and mutant A53T aSyn from Addgene. However, SH-SY5Y cells are hard-to-transfect cell lines and thus transfection protocol must be optimized using different reagent. We have initially transfected these cells with pCMV-EGFP vector using PEI with different plasmid:PEI ratios, and compared cell viability and transfection efficiencies. Transfection efficiencies are very low in all conditions. Best efficiency was obtained with 1:4 plasmid:PEI ratio, and increasing PEI concentration caused toxicity in cells while not improving the transfection efficiency (Figure 3.1).

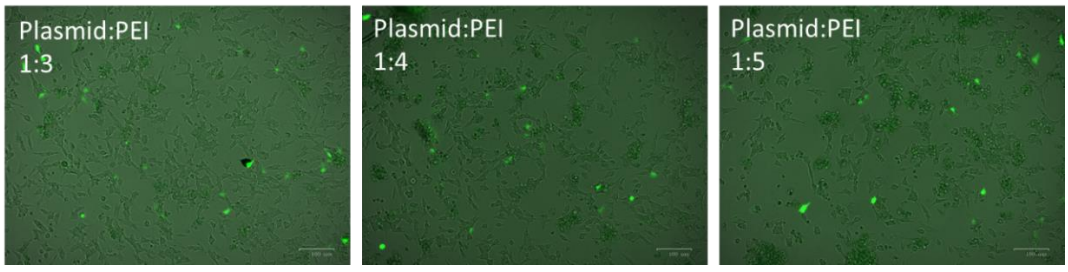

Figure 3.1: Optimization of PEI transfection in SH-SY5Y cells. Fluorescence (EGFP: green) and brightfield images are merged. Qualitative analysis showed that 1:4 plasmid:PEI ratio yields the best transfection efficiency. Scale bar:100 µm

As the accepted efficiency of PEI was not found to be sufficient for further experiments, Lipofectamine 2000 was next used as a transfection reagent. When assessed qualitatively, efficiency of Lipofectamine transfection was accepted to be higher when compared to PEI. Different plasmid:Lipofectamine ratios were applied, and 1:3 plasmid:Lipofectamine yields the best transfection efficiency while toxicity is lower compared to PEI or higher Lipofectamine concentrations (Figure 3.2).

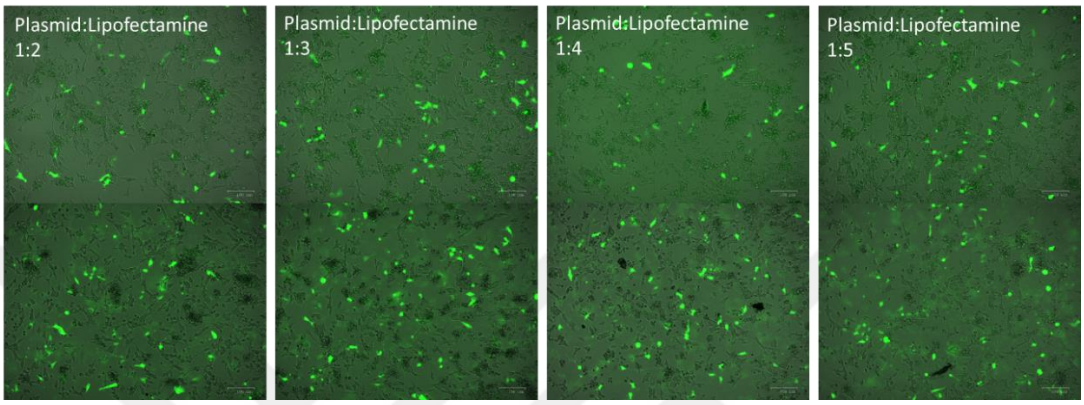

Figure 3.2: Optimization of Lipofectamine transfection in SH-SY5Y cells. Fluorescence (EGFP:green) and brightfield images are merged. 1:3 plasmid:Lipofectamine ratio yields the best transfection efficiency. Scale bar:100 µm

Next, EGFP tagged wild-type (aSyn-WT-EGFP) and mutant (aSyn-A53T-EGFP) α-synuclein coding plasmids were transiently transfected in SH-SY5Y cells. Overexpression was confirmed via Western blotting at 48h of transfection (Figure 3.3) [105]. Empty pEGFP plasmid was used as mock transfection control.

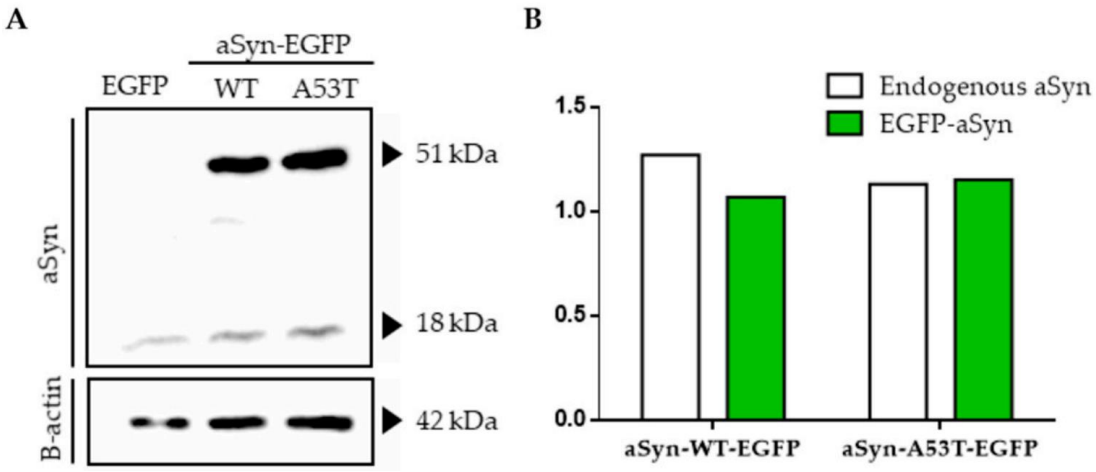

Figure 3.3: Overexpression of aSyn in SH-SY5Y cells.

SH-SY5Y cells were transfected with expression plasmids encoding EGFP tagged wild type and mutant aSyn. A) Western blot results correspond to expression of EGFP tagged wild-type and mutant (transfected, 51 kDa) and endogenous (18 kDa) aSyn are validated using mouse anti-aSyn antibody in Western blotting. B) Protein bands were quantified by normalization to β-actin expression using Gel analysis tool in ImageJ [105].

We have then assessed cell viability in order to determine α-synuclein induced toxicity. Culture medium was replaced with 1 % FBS DMEM and cells were maintained under these conditions for either 12h or 24h, however no significant differences have been observed in either wild-type or mutant α-synuclein overexpressing cells compared to mock transfection (Figure 3.4). This may be due to the short period (12 and 24 h), which may not have been sufficient for accumulation of aSyn in these cells. Nonetheless, since our experimental strategy relies on transient transfection, aSyn overexpression was not found to be applicable to our studies.

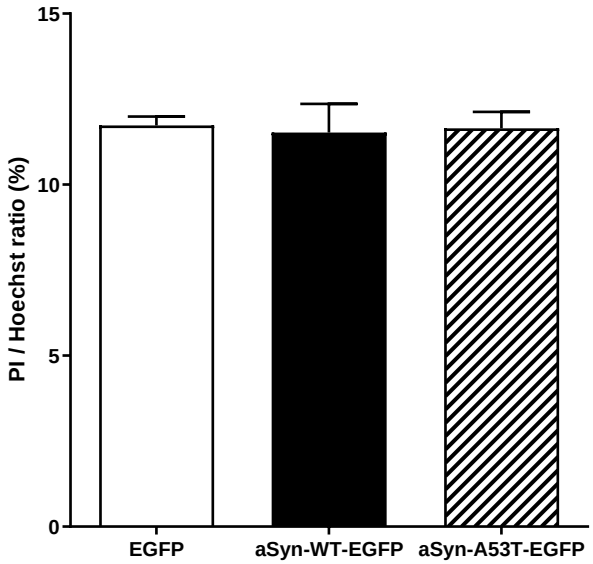

Figure 3.4: Cell viability analysis of aSyn overexpressing SH-SY5Y cells. Cells were transfected with pEGFP, aSyn-WT-EGFP, aSyn-A53T-EGFP plasmids, and 48h after transfection stained with propidium iodide and Hoechst. Number of PI+ and Hoechst+ cells were visualized and quantified automatically and PI/ Hoechst ratio was calculated for four repeats. t-test was applied for statistical analysis.

3.1.1.2. Aggregation Profile of α-synuclein

In addition to cell viability analysis, we wanted to determine the aggregation profile of α-synuclein. Aggregation could not be detected in wild-type or mutant α-synuclein transfected SH-SY5Y cells. As SH-SY5Y cells are hard to transfect cells, we used HEK293T cells to induce high overexpression levels. HEK293T cells overexpressing wild-type or mutant α-synuclein didn't form any visible aggregates. To induce toxic conditions, cells were challenged with serum starvation but neither group showed any aggregation pattern in both conditions (Figure 3.5).

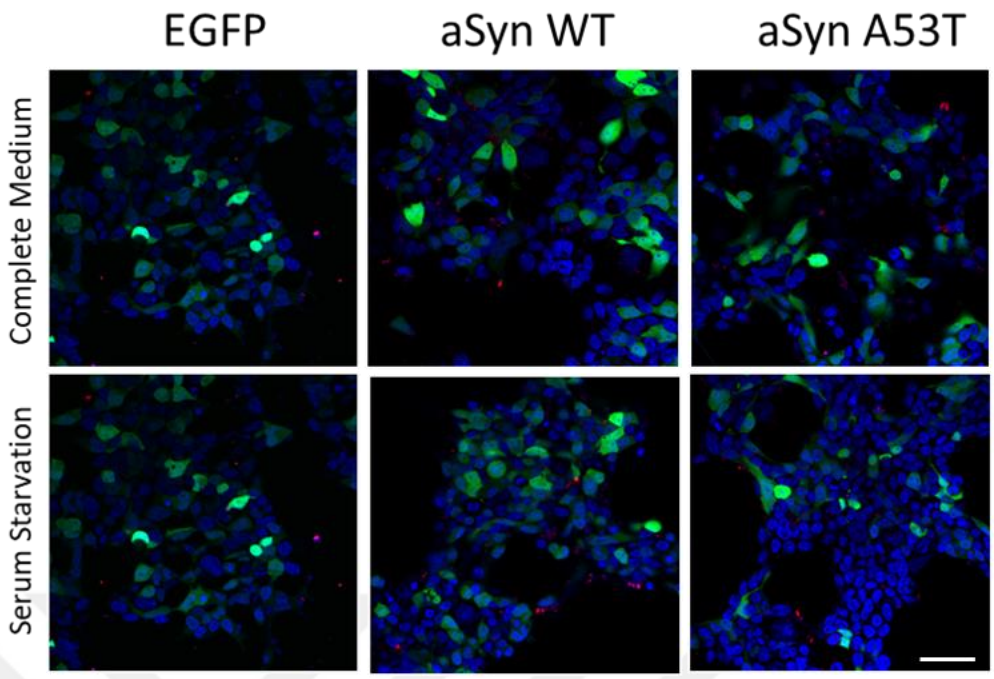

Figure 3.5: Aggregation profile of α-synuclein in normal or serum starvation conditions in HEK293T cells.

HEK293T cells were transfected with expression plasmids encoding either wildtype or Htt (aSyn WT and aSyn A53T respectively) under either complete medium or serum starvation conditions using 1 % FBS, and imaged with 405 nm and 488 nm excitation lasers using confocal microscope (Zeiss LSM 800) with 40x oil objective (NA:1.4) 120h after transfection. Scale bar: 50 µm

3.1.1.3. 6-OHDA induced PD model

As overexpression of wild-type or mutant aSyn didn't induce any significant toxicity, 6-OHDA treatment was applied to SH-SY5Y cells for obtaining a PD model. Different concentrations of 6-OHDA (10 µM, 50 µM, 100 µM, 250 µM, 500 µM) have been applied to SH-SY5Y cells which maintained in 1% FBS medium 3h prior to treatment. Cell viability analysis was performed 24h after 6-OHDA treatment. 100 µM, 250 µM and 500 µM 6-OHDA treatment was found to increase cell death significantly compared to vehicle treatment. 100 µM 6-OHDA has been preferred for further experiments (Figure 3.6).

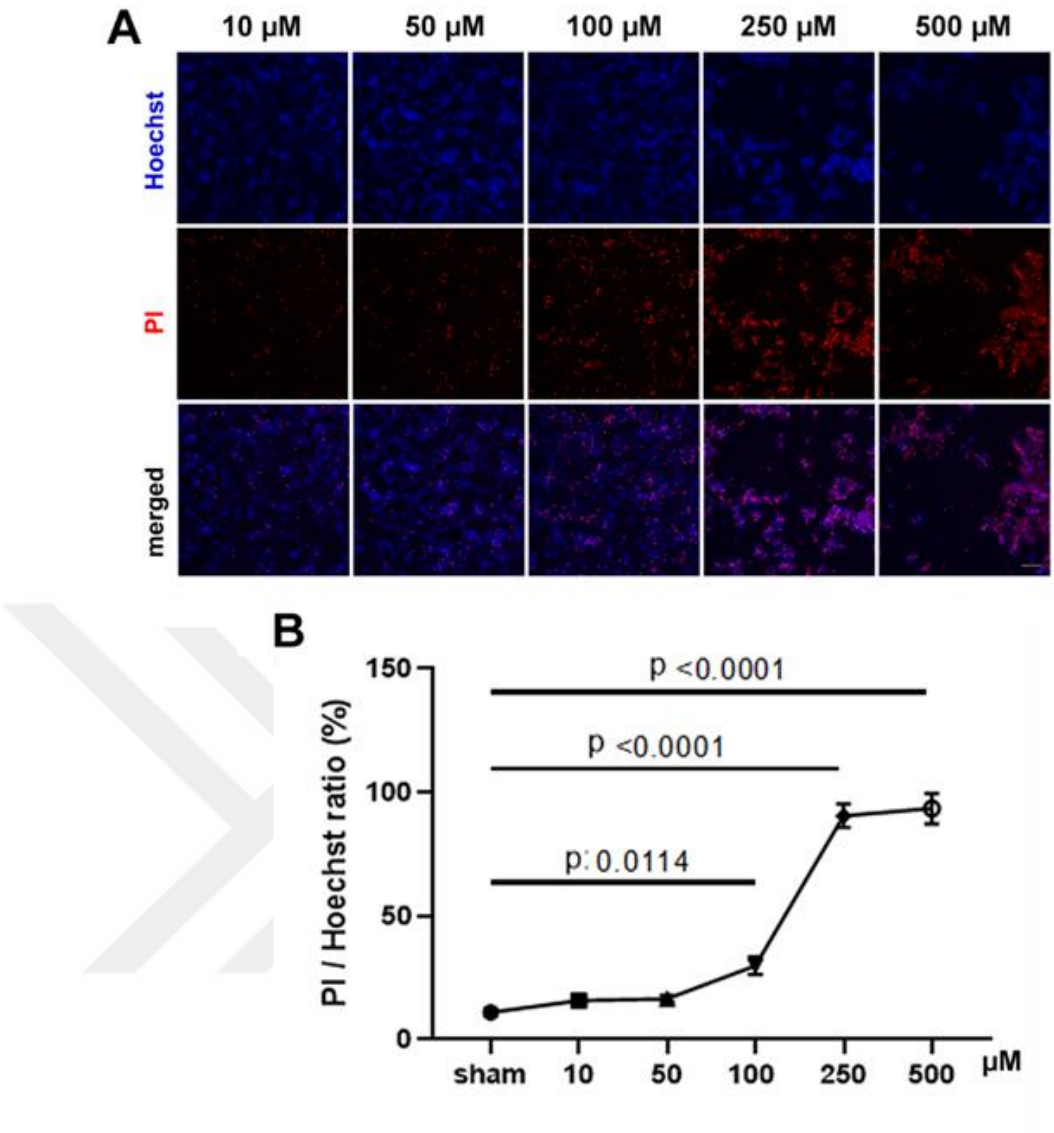

Figure 3.6: Cell viability analysis of SH-SY5Y cells after 6-OHDA treatment. A) Different concentrations of 6-OHDA is applied for 24h and cell viability analysis is performed via Hoechst/PI assay as described previously and representative fluorescence images of cells stained with Hoechst and PI are presented. B) Quantitative analysis of cell death in response to different concentrations of 6-OHDA treatment (n>3, ratio paired t-test applied for statistical analysis). Scale bar: 100µm

To determine effect of both aSyn overexpression and the presence of 6-OHDA on cell death, wildtype and mutant aSyn-overexpressing SH-SY5Y cells were treated with 6-OHDA for 12h or 24h and cell viability analysis was performed. Although wild-type or mutant aSyn overexpression increased cell death slightly compared to mock

transfection in the presence of 6-OHDA, these differences were not significant when compared to 6-OHDA effect (**Figure 3.7**). We have therefore decided to continue our *in vitro* PD studies using 6-OHDA model.

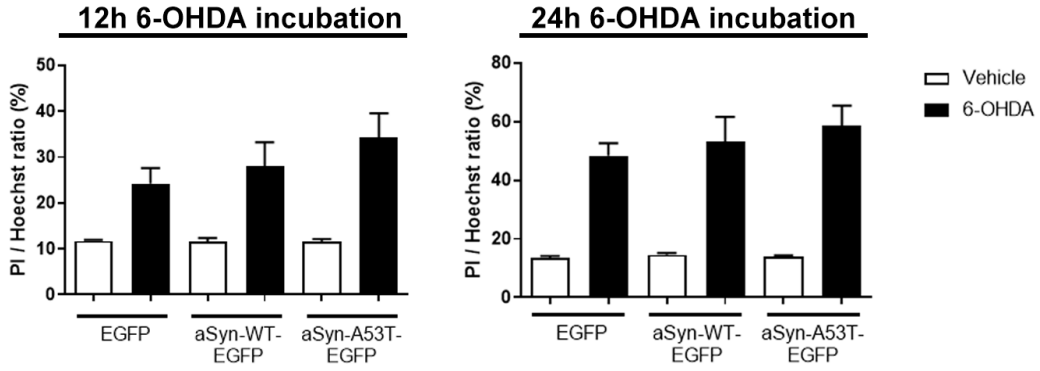

Figure 3.7: 6-OHDA induced toxicity in aSyn overexpressing SH-SY5Y cells. Cells were incubated with either dH_2O as vehicle or 100 uM 6-OHDA for 12 and 24 hrs, after which they were stained for PI and H, and PI/H ratio was calculated as described above.

3.1.1.4. Transcriptome Analysis in 6-OHDA induced PD model

As aSyn overexpression was not found to cause significant changes in the short time period of transient transfection, 6-OHDA model was chosen for further experiments. In order to carry out transcriptome analysis, SH-SY5Y cells have been collected at 12h and 18h of 100 µM 6-OHDA treatments and RNA was isolated. RIN values were found to be higher than 9.0 in all samples, therefore all of the samples have been processed further for microarray analysis. Bioinformatics analysis was performed in Çakır Lab. Essentially, 12h and 18h 6-OHDA treatments were found to yield similar distribution in PCA analysis, therefore samples were pooled before analysis. Fold changes of 1262 gene probes were found to decrease and 1208 gene probes were increased significantly (q values of Benjamini-Hochberg <0.05, determined by Çakır Lab.) (Figure 3.8).

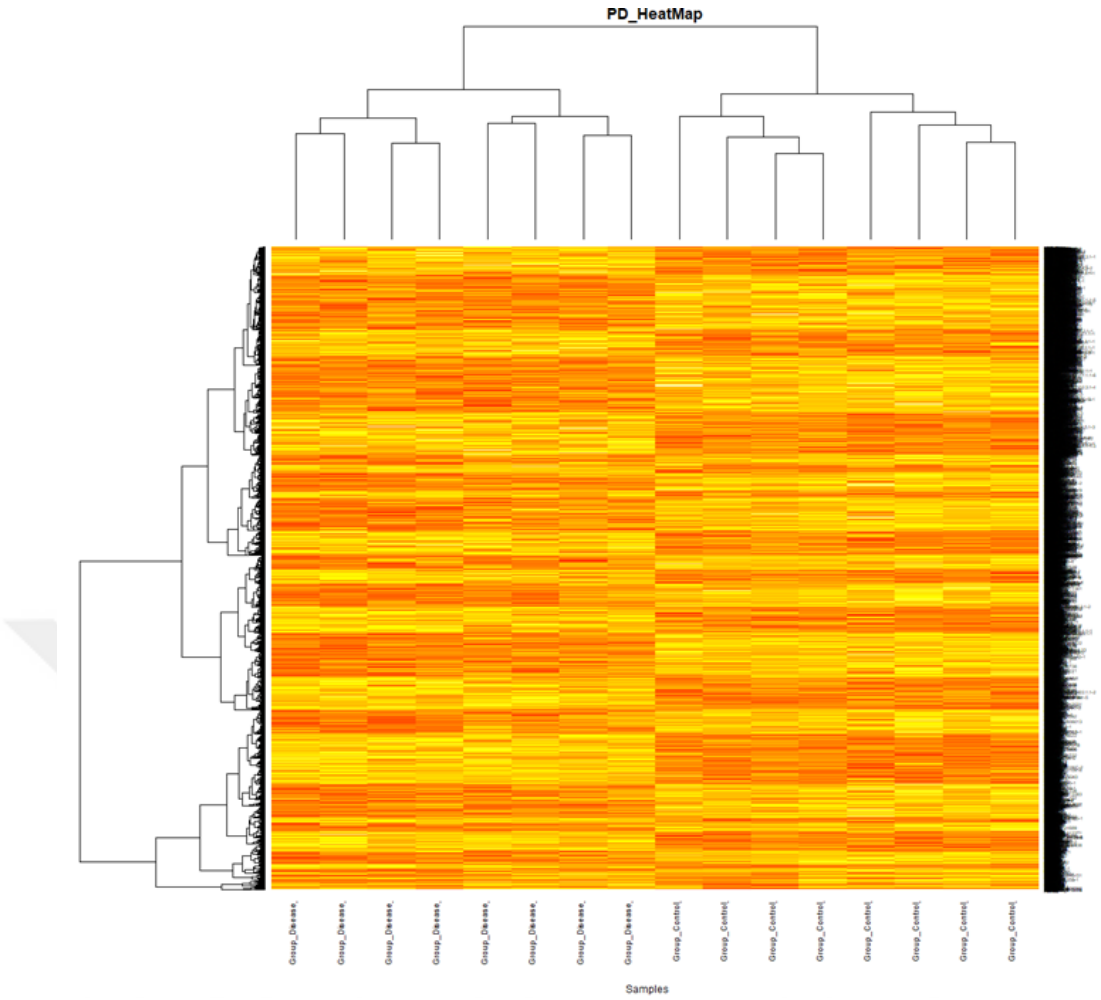

Figure 3.8: Representative heat map of significantly changed gene expressions. Gene expressions of 6-OHDA treated SH-SY5Y cells are compared to vehicle treatment (1000 genes are included, yellow and red code represents upregulated and downregulated genes respectively). Possible drug targets were determined by drug repositioning approach in Çakır Lab. A total of 5 drugs are selected for further applications (Table 3.1).

Table 3.1: Selected drugs and their gene targets.

Gene Symbol	Gene Name	P value	FC	Betweenness Centrality	Drug Target
ITGB2	integrin, beta 2 (complement component 3 receptor 3 and 4 subunit)	2.08E-08	3.41	2.11E-03	SIMVASTATIN
AKR1C3	aldo-keto reductase family 1, member C3	3.27E-08	3.24	4.21E-03	INDOMETACIN; RUTIN
CCKBR	cholecystokinin B receptor	1.82E-11	2.80	3.82E-05	PENTAGASTRIN
CEBPB	CCAAT/enhancer binding protein (C/EBP), beta	2.87E-05	1.92	3.02E-03	QUERCETIN

For validation of microarray results, RNA is isolated from the same samples and Ekin Sönmez performed the RT-PCR experiments (unpublished data; Figure 3.9).

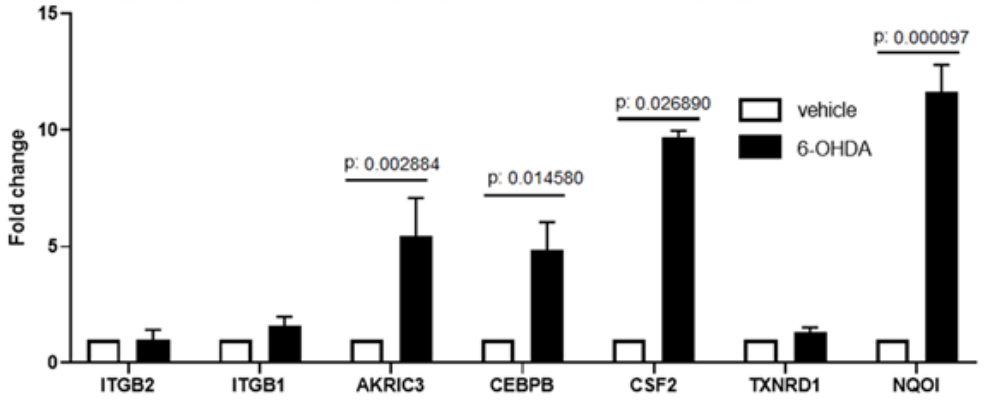

Figure 3.9: Gene expression changes in 6-OHDA treated SH-SY5Y cells. Cells were incubated with either dH_2O as vehicle (white bars) or 100 uM 6-OHDA (black bars) for 12 hrs, after which qRT-PCR analysis was performed for indicated gene targets reported for drugs identified in transcriptomic studies. Fold change was calculated as $2^{-\Delta\Delta Ct}$ and p values were determined by t-test (n>3) (Drug treatments and RNA isolation is done in the scope of this thesis and Ekin Sönmez performed the RT-PCR experiments).

3.1.1.5. Drug treatments in 6-OHDA induced PD model

Neuroprotective effects of selected drugs have been investigated in 6-OHDA treated SH-SY5Y cells. Drugs were prepared in DMSO and used at variable concentrations according to the previous studies in literature. Cells have been treated with drugs either before, after or at the same time with 6-OHDA application in the presence of 1% FBS, in order to assess whether these drugs can have a therapeutic vs neuroprotective effect (Figure 3.10).

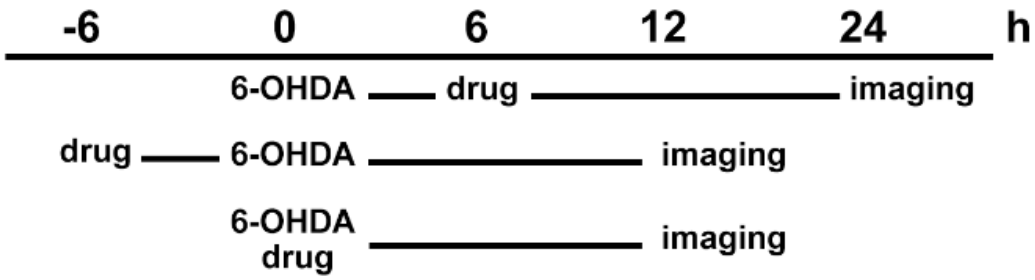

Figure 3.10: Timeline of 6-OHDA and drug applications.

Drug and 6-OHDA treatments are done in different time points and cell viability analyses are performed. To test the efficacy of drugs, cell viability analysis (imaging) is performed as it is presented in the timeline. If drugs are applied simultaneously with 6-OHDA, none of the drugs confer significant neuroprotection (Figure 3.11).

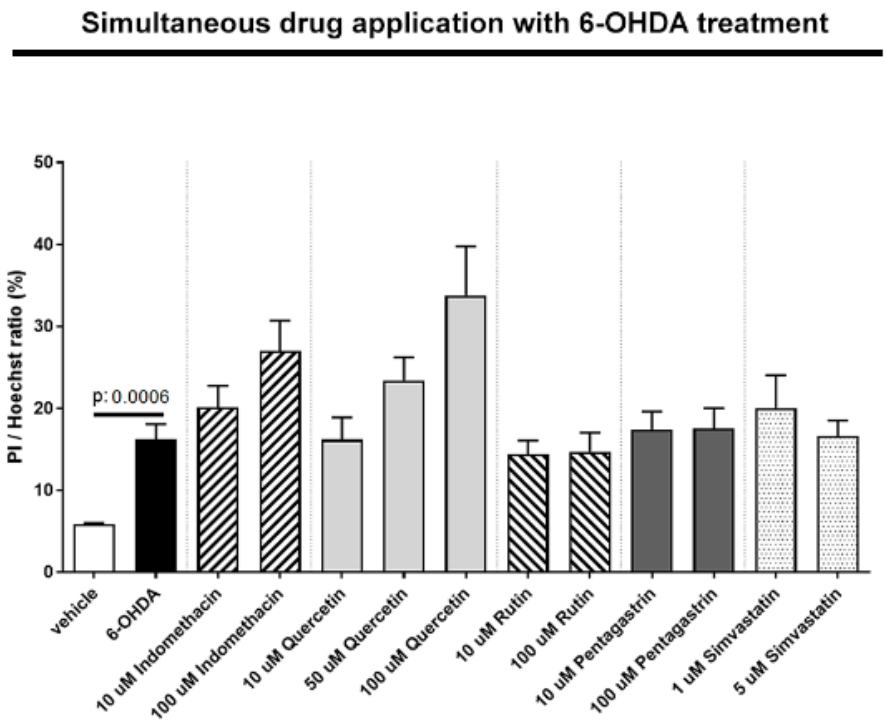

Figure 3.11: Cell viability analysis of 6-OHDA-treated SH-SY5Y cells in response to simultaneous drug treatments.

Cells were incubated with either dH2O and DMSO as vehicle (white bars) or 100 uM 6-OHDA (black bars) simultaneously with drugs indomethacin, quercetin, rutin, pentagastrin and simvastatin at indicated concentrations for 12 hrs. Cells were then stained with PI and Hoechst and PI/H ratio was calculated as before (p values were determined by ratio paired t-test, n=6).

Next, drugs have been applied before or after 6-OHDA treatments. Indomethacin, pentagastrin or simvastatin did not have any effect in drug treatments either before or after 6-OHDA applications (Figure 3.12, Figure 3.13). Rutin was found to be protective either before or after 6-OHDA applications (Figure 3.12, Figure 3.13). On the other hand, low concentrations of quercetin and both low and high concentrations of rutin were found to be neuroprotective when applied before 6-OHDA treatments (Figure 3.13).

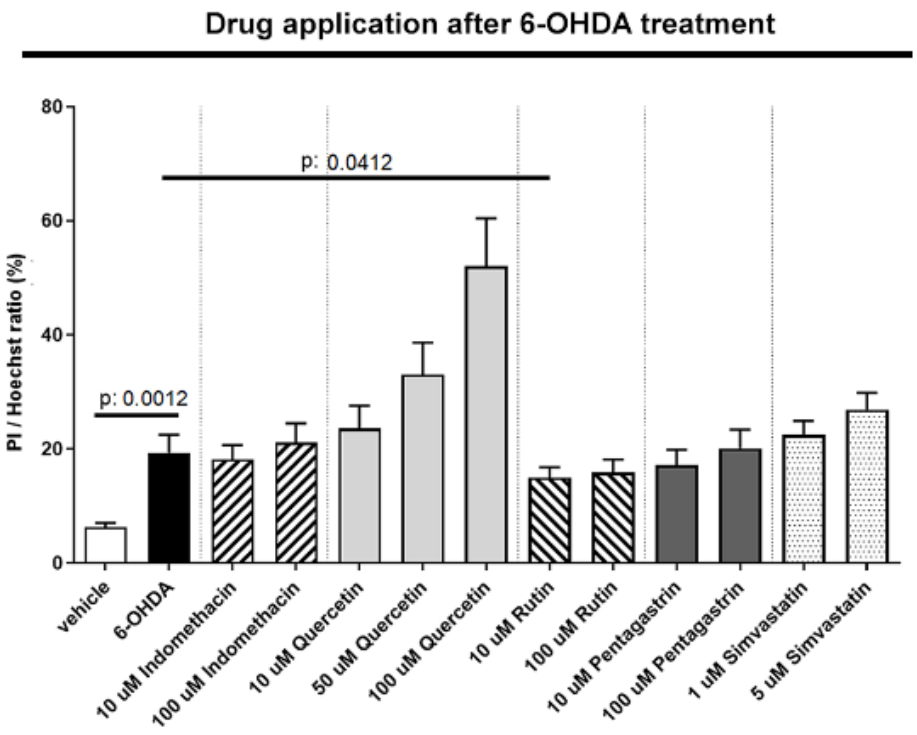

Figure 3.12: Cell viability analysis of 6-OHDA treated SH-SY5Y cells in response to drug treatments.

Cells were incubated with either dH2O and DMSO as vehicle (white bars) or 100 uM 6-OHDA (black bars); after 6 hr incubation, cells were administered the drugs indomethacin, quercetin, rutin, pentagastrin and simvastatin at indicated concentrations and incubated further for 24 hrs. Cells were then stained with PI and Hoechst and PI/H ratio was calculated as before (p values were determined by ratio paired t-test, n=6).

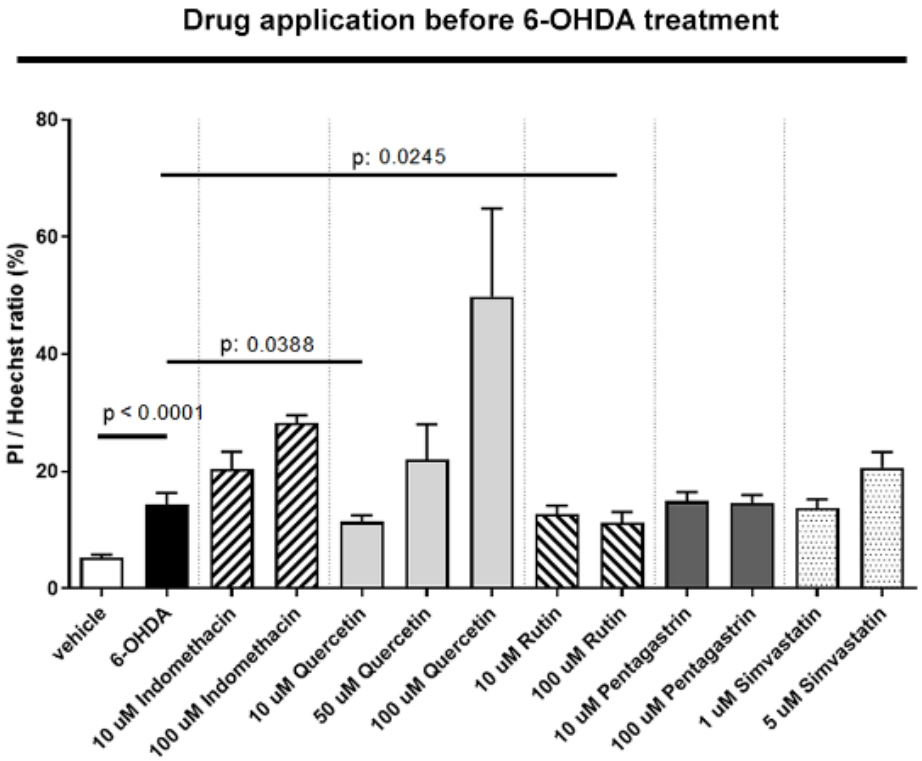

Figure 3.13: Cell viability analysis of 6-OHDA treated SH-SY5Y cells in response to drug treatments before 6-OHDA application.

Cells were administered the drugs indomethacin, quercetin, rutin, pentagastrin and simvastatin at indicated concentrations and incubated for 6 hrs; cells were then treated with either dH2O and DMSO as vehicle (white bars) or 100 uM 6-OHDA (black bars) incubated further for 12 hrs. Cells were then stained with PI and Hoechst and PI/H ratio was calculated as before (p values were determined by ratio paired t-test, n=6).

As quercetin and rutin effectively decreased toxicity of 6-OHDA in SH-SY5Y cells, expression of their target genes were analyzed in RT-PCR experiments (performed by Ekin Sönmez; unpublished). Quercetin was not found to have any effect on its target AKRIC3 but it decreased CEBPB expression, albeit not significantly. Rutin treatment was found to decrease expression of both AKRIC3 and CEBPB although not significantly (Figure 3.14).

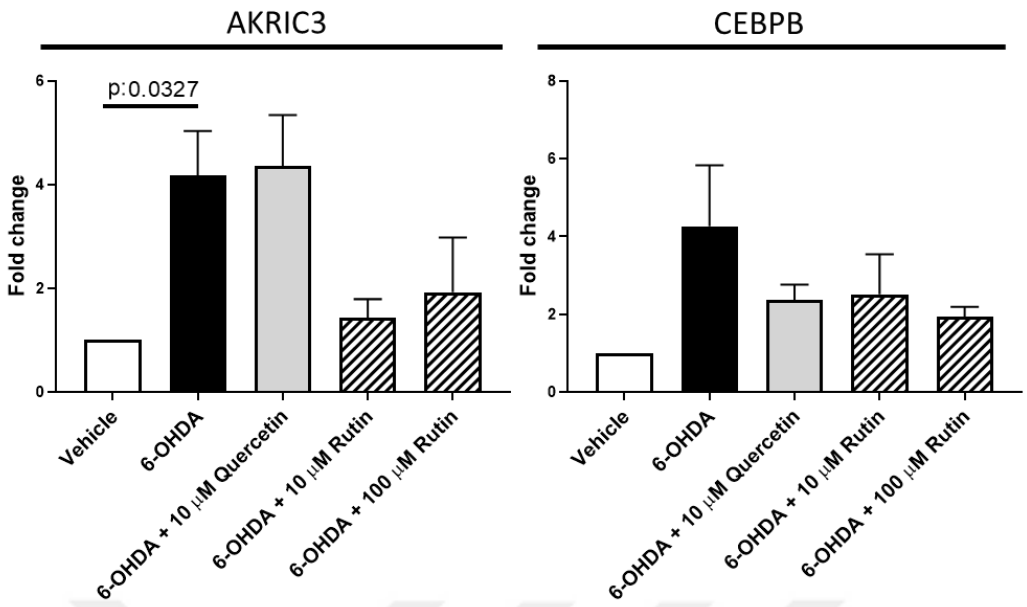

Figure 3.14: Expressions of target genes in response to drug treatments before 6-OHDA applications.

Cells were incubated with either dH_2O and DMSO as vehicle (white bars), 100 uM 6-OHDA (black bars), 100 uM 6-OHDA and 10 uM quercetin (6h before 6-OHDA) (gray bars) and 100 uM 6-OHDA and 10 or 100 uM rutin (6h before 6-OHDA) (striped bars) for a total of 18 hrs, after which qRT-PCR analysis was performed for gene targets AKRIC3 and CEBPB. Fold change was calculated as $2^{-\Delta\Delta Ct}$ and p values were determined by t-test (n>3) (RT-PCR was performed by Ekin Sönmez).

Drug efficacies were tested in PD related genes in addition to decreasing expressions of targets genes and 6-OHDA induced toxicity. Quercetin and rutin treatments were found to decrease expression of SNCA, LRRK1 and LRRK2, which have been increased after 6-OHDA applications, compared to vehicle treatments (Figure 3.15).

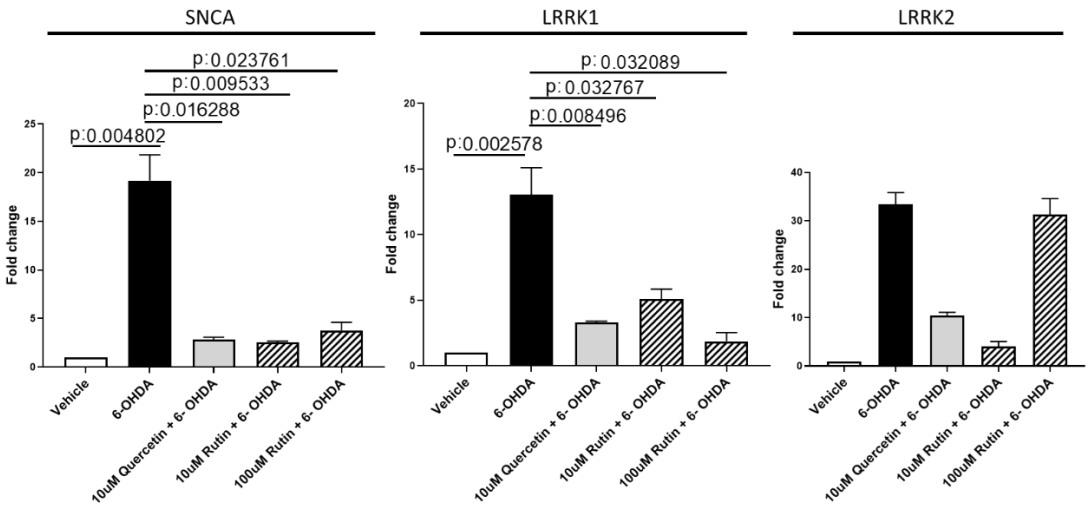

Figure 3.15: Expressions of PD related genes in response to 6-OHDA and drug treatments.

Cells were incubated with either dH_2O and DMSO as vehicle (white bars), 100 uM 6-OHDA (black bars), 100 uM 6-OHDA and 10 uM quercetin (6h before 6-OHDA) (gray bars) and 100 uM 6-OHDA and 10 or 100 uM rutin (6h before 6-OHDA) (striped bars) for a total of 18 hrs, after which qRT-PCR analysis was performed for PD-related genes SNCA, LRRK1 and LRRK2. Fold change was calculated as $2^{-\Delta\Delta Ct}$ and p values were determined by t-test (n>3) (RT-PCR was performed by Ekin Sönmez).

3.1.1.6. Neuroprotective effect of Elk1 in 6-OHDA treated SH-SY5Y cells

Elk1 expression in response to 6-OHDA treatment is determined by RT-PCR performed by Ekin Sönmez (unpublished data). Elk-1 expression is increased in SH-SY5Y cells after 6-OHDA treatment, and quercetin or rutin treatment prior to 6-OHDA application is decreased its expression (Figure 3.16).

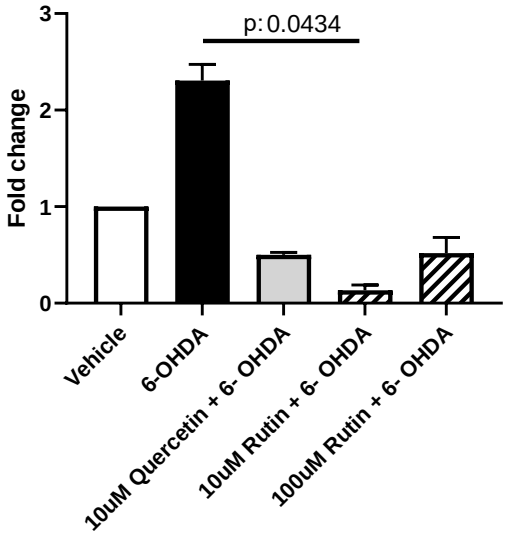

Figure 3.16: Expression of Elk1 in response to drug treatments before 6-OHDA applications.

Cells were incubated with either dH_2O and DMSO as vehicle (white bars), 100 uM 6-OHDA (black bars), 100 uM 6-OHDA and 10 uM quercetin (6h before 6-OHDA) (gray bars) and 100 uM 6-OHDA and 10 or 100 uM rutin (6h before 6-OHDA) (striped bars) for a total of 18 hrs, after which qRT-PCR analysis was performed for Elk-1 expression levels. Fold change was calculated as $2^{-\Delta\Delta Ct}$ and p values were determined by t-test (n>3) (RT-PCR was performed by Ekin Sönmez).

We hypothesized that increased Elk1 expression in SH-SY5Y cells after 6-OHDA application is an activation of an endogenous neuroprotection mechanism, which is not necessary in the presence of neuroprotective drugs. In order to assess this hypothesis, we have overexpressed Elk1 by a constitutively active expression system (VP16) prior to 6-OHDA application and performed cell viability analyses. We have found that Elk1 overexpression is protective against 6-OHDA induced cell death in early stages of 6-OHDA application (12h) but this protection is lost at later stages (24h) (Figure 3.17).

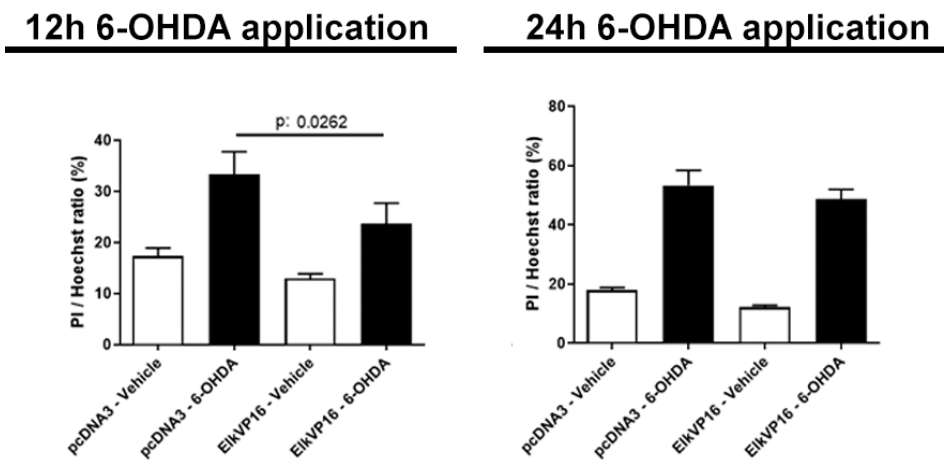

Figure 3.17: Cell viability analysis in Elk1 overexpressing SH-SY5Y cells in response to 6-OHDA application.

Cells were transfected with either pcDNA3 as mock transfection and ElkVP16 for constitutive expression of Elk1. After 48h of transfection, cells were incubated with dH_2O as vehicle (white bars) and 100 uM 6-OHDA (black bars) for 12 or 24 hrs. Cells were then stained with PI and Hoechst and PI/H ratio was calculated as before (p values were determined by ratio paired t-test, n=4).

3.1.2. Modelling PD in LUHMES cells

LUHMES cell line is considered as a reliable dopaminergic neuron model if differentiated under suitable conditions and they can be used for modelling PD and drug toxicology assays [106-108]. For this reason, we have performed similar experiments using LUHMES cells.

3.1.2.1. Differentiation of LUHMES cells

LUHMES cells are obtained from Schildknecht Laboratory and differentiated according to the optimized protocol [106]. LUHMES differentiation takes a total of 6 days and differentiated cells can be morphologically distinguished by separated cell bodies and complex projections similar to those in primary neuronal cultures (Figure 3.18).

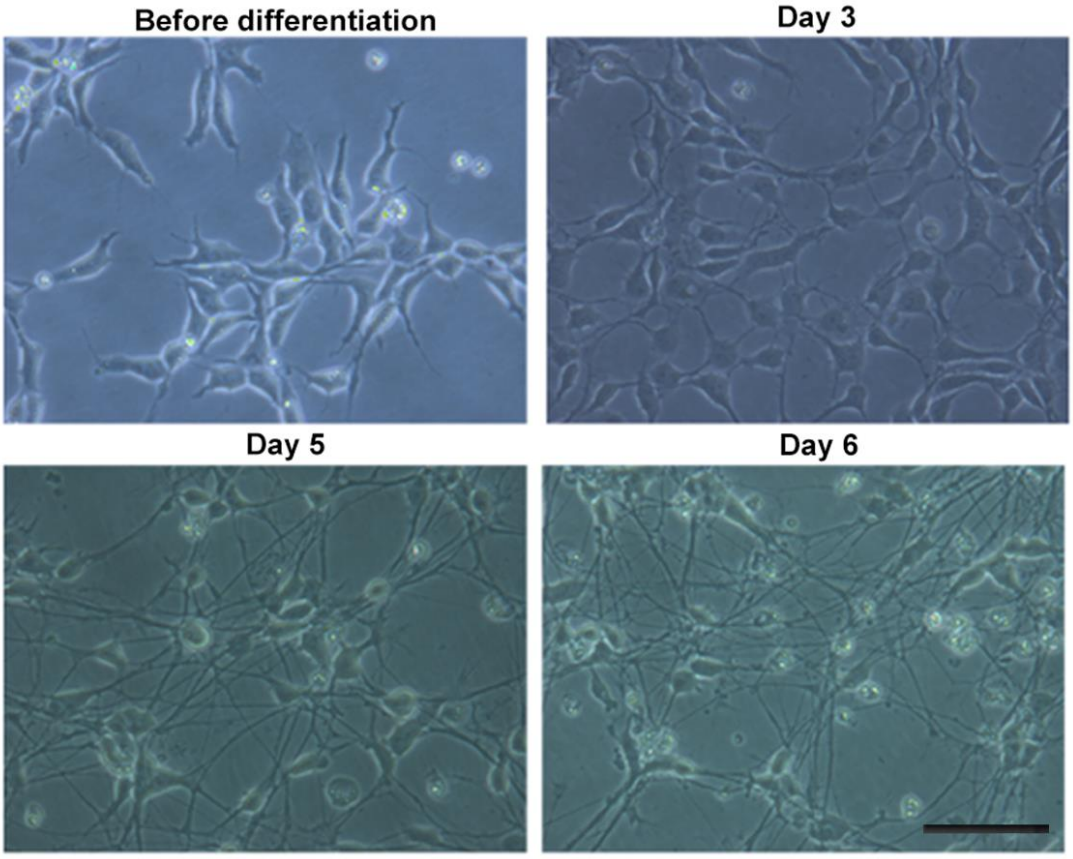

Figure 3.18: Representative brightfield images of LUHMES cells indicating morphological changes during differentiation process.

LUHMES cells are either maintained in normal growth medium or differentiated for 6 days in differentiation medium as described; neurite-like projections were monitored under phase contrast microscope (Zeiss Primo Vert) using 20x Plan Apochromat objective (NA:0.8) Scale bar: 50µm

3.1.2.2. Validation of α-synuclein overexpression in differentiated cells

LUHMES and LUHMES-aSyn-iRES-EGFP cell lines are differentiated in cell culture as described. Differentiated LUHMES-aSyn-iRES-EGFP cells confer diffuse EGFP expression (Figure 3.19). α-synuclein overexpression is confirmed in protein expression levels: Western blot results showed that expression of α-synuclein protein was higher in LUHMES- aSyn-iRES-EGFP cell line compared to naïve LUHMES cells (Figure 3.20).

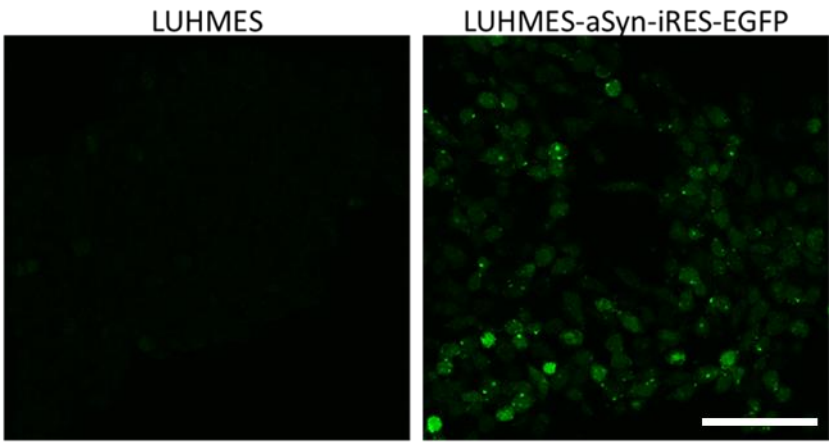

Figure 3.19: Widespread EGFP expression in LUHMES-aSyn cells. Parental LUHMES cells and aSyn-overexpressing aSyn-iRES-EGFP-LUHMES cells were imaged for GFP fluorescence under confocal microscope (Zeiss LSM 880) with 20x objective (NA:0.8) at 488 nm excitation light. Scale bar: 100 µm

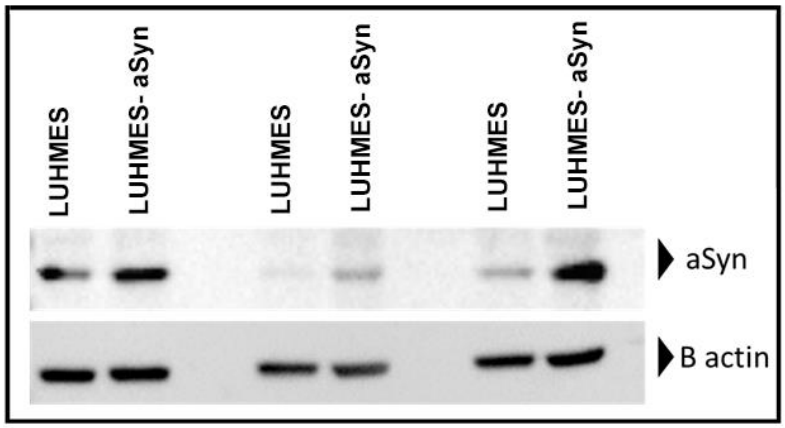

Figure 3.20: Western blot of α-synuclein expression in LUHMES cells. α-synuclein overexpression in parental LUHMES cells vs aSyn-overexpressing LUHMES-aSyn cells is validated by Western blotting using rabbit anti β-actin and mouse anti α-synuclein as primary antibodies.

It has to be emphasized that similar to SH-SY5Y cells overexpressing wildtype or mutant A53T aSyn, LUHMES-aSyn cells did not exhibit any visible aSyn aggregates or any significant cell death due to overexpression of aSyn. In accordance

with our findings, it is shown that aSyn overexpression by itself isn't sufficient to cause significant cell death [86, 106].

3.1.2.3. 6-OHDA induced PD model

As α-synuclein overexpression was not found to be sufficient to cause toxicity in SH-SY5Y or in LUHMES cells, 6-OHDA treatment was preferred in LUHMES-based *in vitro* PD model. Naïve and aSyn overexpressing LUHMES cells were treated with different concentrations of 6-OHDA, and cell viabilities were determined. LUHMES cells were found to be more sensitive to 6-OHDA-induced toxicity compared to SH-SY5Y cells: 100 µM 6-OHDA treatment resulted with 100 % cell death. Therefore, 50 µM 6-OHDA was selected for further experiments (Figure 3.21).

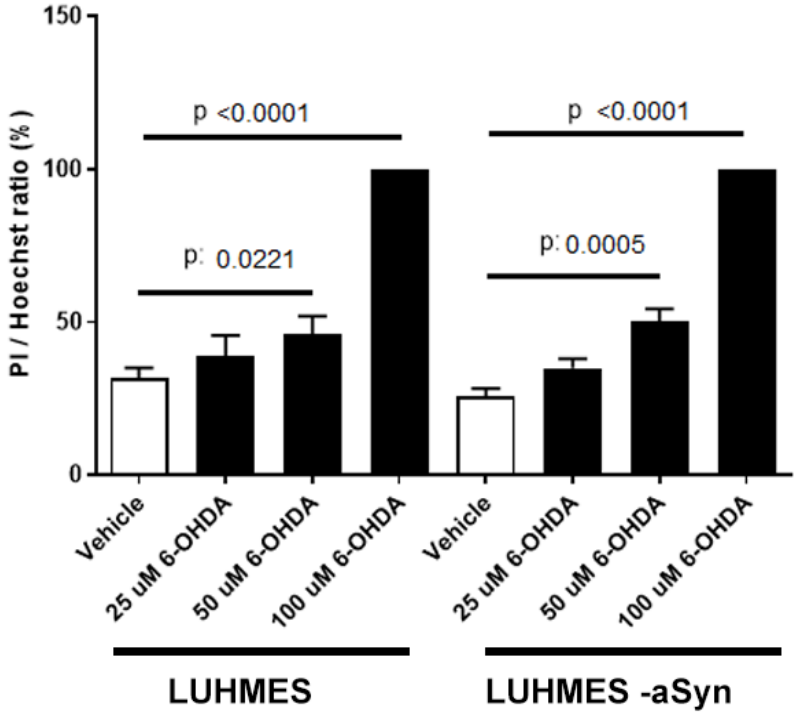

Figure 3.21: Concentration dependent 6-OHDA induced toxicity in LUHMES and LUHMES-aSyn cells.

Parental LUHMES and aSyn-overexpressing LUHMES-aSyn cells were treated with increasing amounts of 6-OHDA, stained for PI and H, and PI/H ratio was calculated as described before. p values were determined by ratio paired t-test (n=3).

3.1.2.4. Transcriptome Analysis in 6-OHDA induced PD model

Differentiated LUHMES and LUHMES-aSyn cells were treated with 50 µM 6-OHDA for 12h, cells were then collected, RNA was isolated and prepared for RNASeq experiments. Bioinformatics analyses have been performed and Benjamini-Hochberg analysis is done with p value <0.01 by Çakır Lab. 5972 genes were determined to be significantly changed between vehicle and 6-OHDA treatments in LUHMES cells and 6-OHDA treated LUHMES-aSyn cells were found to have 6098 significantly changed gene expressions compared to vehicle treated LUHMES cells. CEBPB gene, which is the target of Quercetin, was found to be significantly increased in 6-OHDA treated groups compared to vehicle treatments.

3.1.2.5. Drug treatments in 6-OHDA induced PD model

Quercetin and rutin were previously found to be effective in SH-SY5Y cell model of PD. To test their efficiency also in LUHMES model, LUHMES and LUHMES-aSyn cells were treated with drugs prior to 6-OHDA application. 10 µM rutin was found to significantly decrease 6-OHDA induced toxicity in LUHMES cells (**Figure 3.22**).

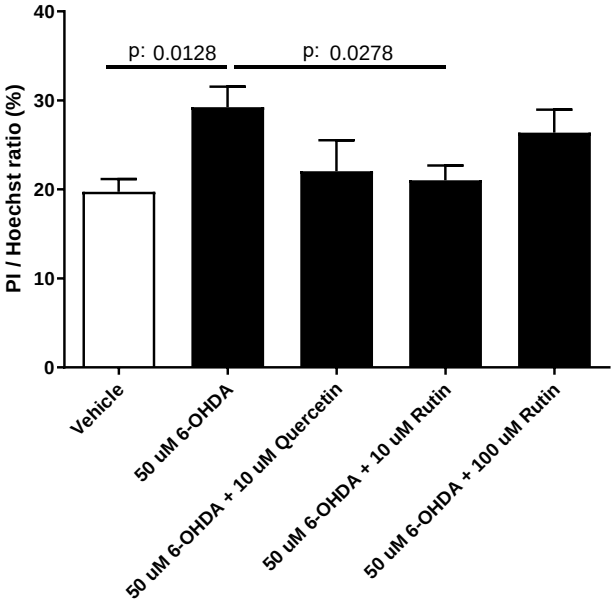

Figure 3.22: Quercetin and rutin pretreatment of LUHMES cells before 6-OHDA application.

Parental LUHMES cells were incubated with either dH_2O and DMSO as vehicle (white bar), 100 uM 6-OHDA, 100 uM 6-OHDA and 10 uM quercetin (6h before 6-OHDA) (black bar) and 100 uM 6-OHDA and 10 or 100 uM rutin (6h before 6-OHDA) (black bar) for a total of 18 hrs, after which cell viability analysis was performed. Cells were stained with PI and Hoechst and PI/H ratio was calculated as before (p values were determined by ratio paired t-test, n=4).

Same approach was applied for LUHMES-aSyn cells and both 10 µM quercetin and rutin treatment and 100 µM rutin treatment significantly decreased 6-OHDA induced toxicity in LUHMES-aSyn cells (Figure 3.23).

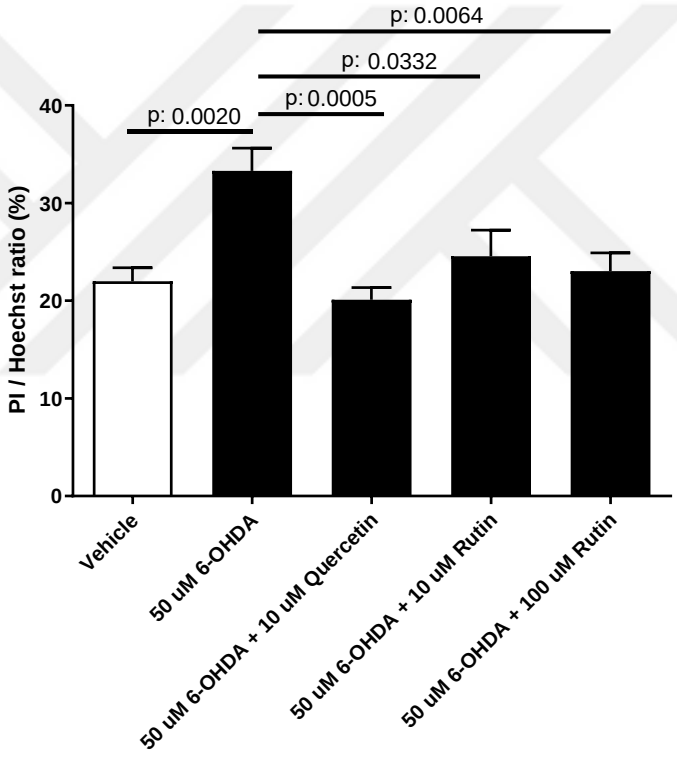

Figure 3.23: Quercetin and rutin pretreatment of LUHMES-aSyn cells before 6-OHDA application.

aSyn overexpressing LUHMES cells were incubated with either dH_2O and DMSO as vehicle (white bar), 100 uM 6-OHDA, 100 uM 6-OHDA and 10 uM quercetin (6h before 6-OHDA) (black bar) and 100 uM 6-OHDA and 10 or 100 uM rutin (6h before 6-OHDA) (black bar) for a total of 18 hrs, after which cell viability analysis was performed. Cells were stained with PI and Hoechst and PI/H ratio was calculated as before (p values were determined by ratio paired t-test, n=6).

3.1.2.6. Transcriptome Analyses in drug treatments

As quercetin and rutin were found to be more effective in protecting against 6-OHDA-induced toxicity in LUHMES-aSyn cells, RNASeq analyses have been performed in drug-treated LUHMES-aSyn cells, and gene expression changes were determined. Bioinformatics analyses were performed in Çakır Lab. Gene onthology (GO) and Kyoto Encyclopedia of Genes and Genomes (KEGG) Pathway analyses were performed on significantly changes genes (compared to vehicle treatment control, adjusted p value<0.05). If p value cutoff applied as p<0.05; 7474, 2199 and 94 significantly changed genes were identified in 6-OHDA applied LUHMES-aSyn cells, Quercetin pretreated 6-OHDA applied and Rutin pretreated 6-OHDA applied LUHMES-aSyn cells respectively. GO enrichment analysis revealed that 6-OHDA treatment mainly affected neural development processes such as axonogenesis, neuron projection development, neurogenesis and neuron development (fold enrichment>1.3, Figure 3.24 – upper panel). On the other hand, quercetin and rutin pretreatment have an effect on mainly neuronal pathways as GO enrichment analysis in drug treated LUHMES-aSyn cells didn't show neuron related pathways (Figure 3.24 – middle and lower panel) possibly indicating that drugs have their effects on these pathways.

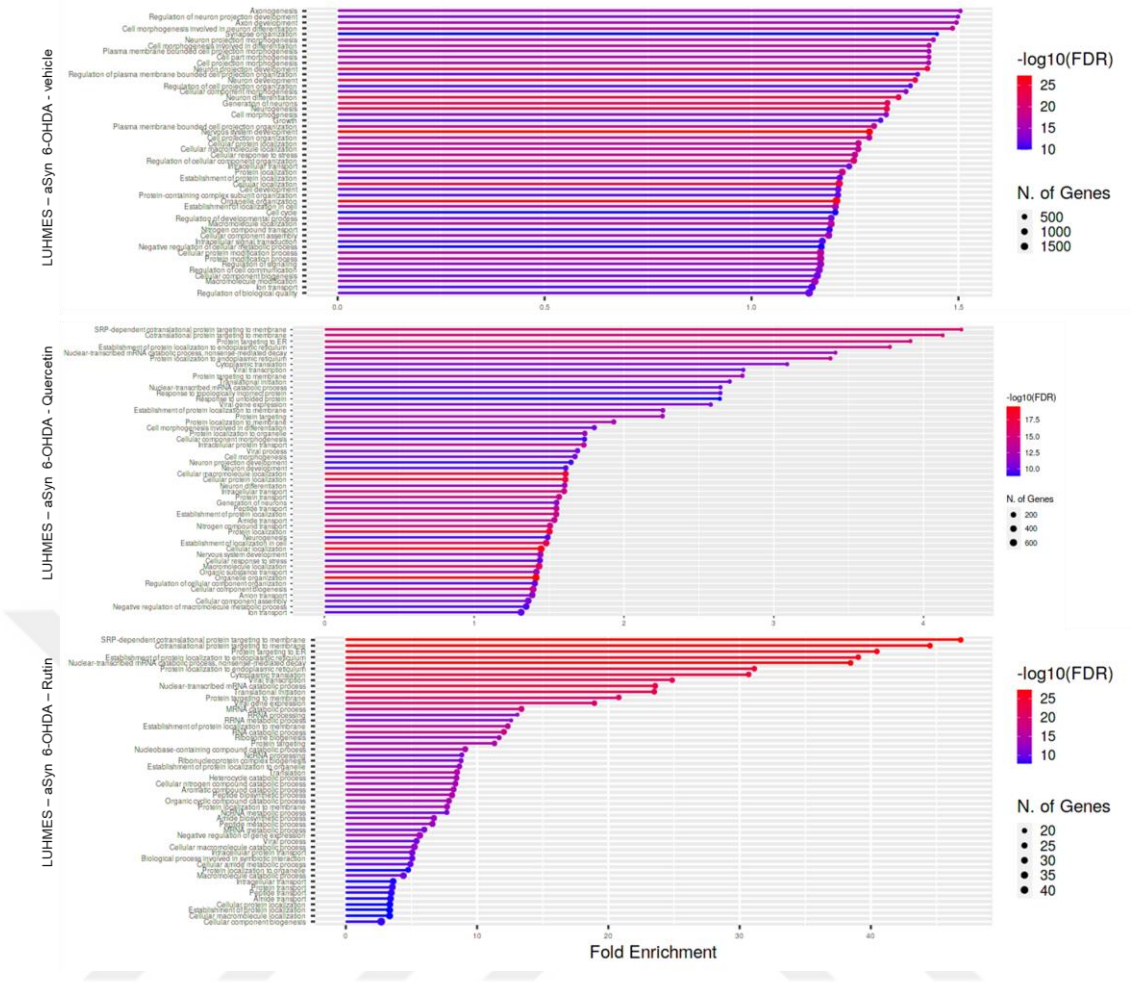

Figure 3.24: GO Analysis in 6-OHDA treated LUHMES-aSyn cells. Differentiated LUHMES-aSyn cells were pretreated with DMSO as vehicle control (upper panel) or 10 µM quercetin (middle panel) and 10 µM rutin (lower panel) before 50 µM 6-OHDA application. RNASeq analysis was performed and GO analysis was constructed compared to vehicle treatments using ShinyGO bioinformatics tool.

KEGG Pathways analysis revealed PD related gene expression changes in LUHMES-aSyn cells treated with 6-OHDA. Mainly affected genes belong to dopaminergic synapse, ubiquitin-proteasome, protein processing in ER, tyrosine metabolism, axonal transport deficit and mitochondrial pathway all leading to cell toxicity and death (Figure 3.25). PD related gene expression pathway couldn't found in KEGG pathway analysis in Quercetin pretreated LUHMES-aSyn cells and rutin

pretreatment affected PD related gene expression changes mostly in the dopaminergic, protein processing in ER and axonal transport pathways (Figure 3.26).

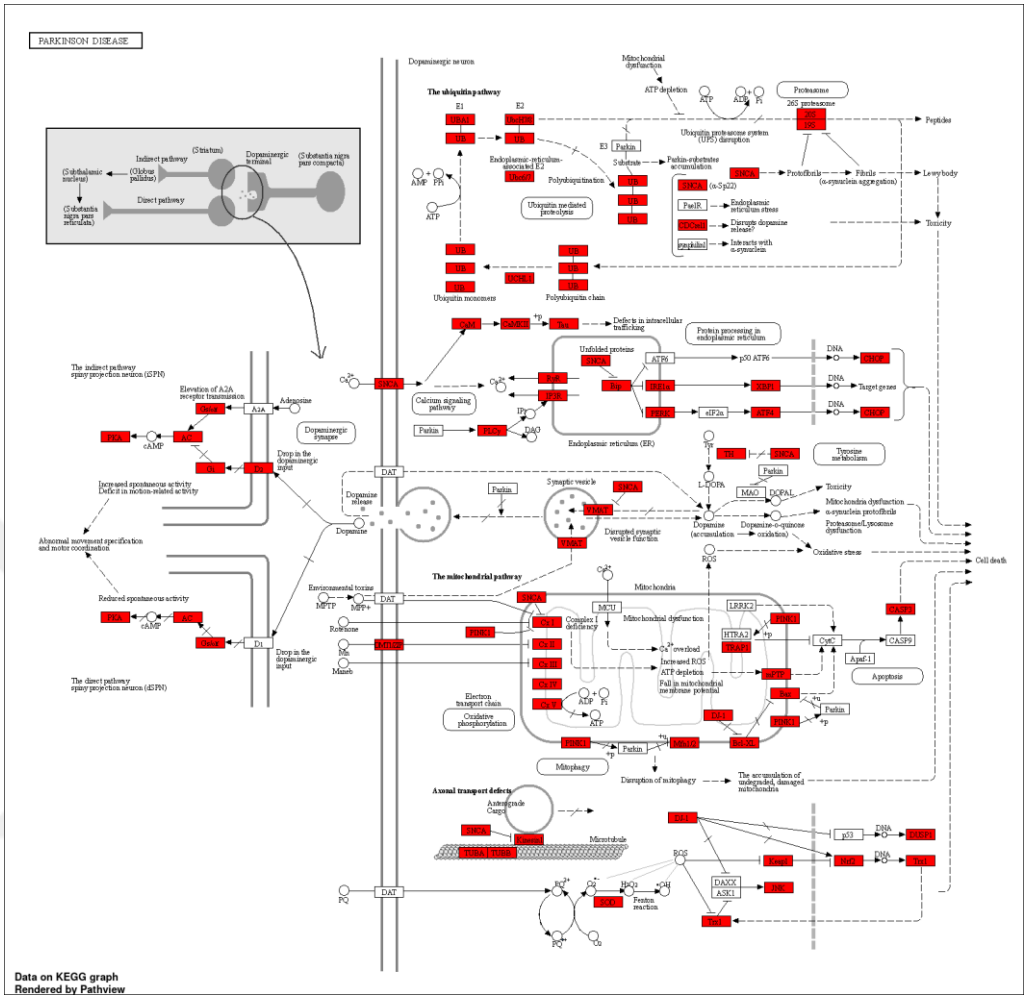

Figure 3.25: KEGG pathway analysis of PD related genes in 6-OHDA treated LUHMES-aSyn cells.

Differentiated LUHMES-aSyn cells were treated with 50 µM 6-OHDA and RNASeq analysis was performed compared to vehicle treatment as control (n=3). KEGG pathway analysis was constructed using ShinyGO bioinformatics tool.

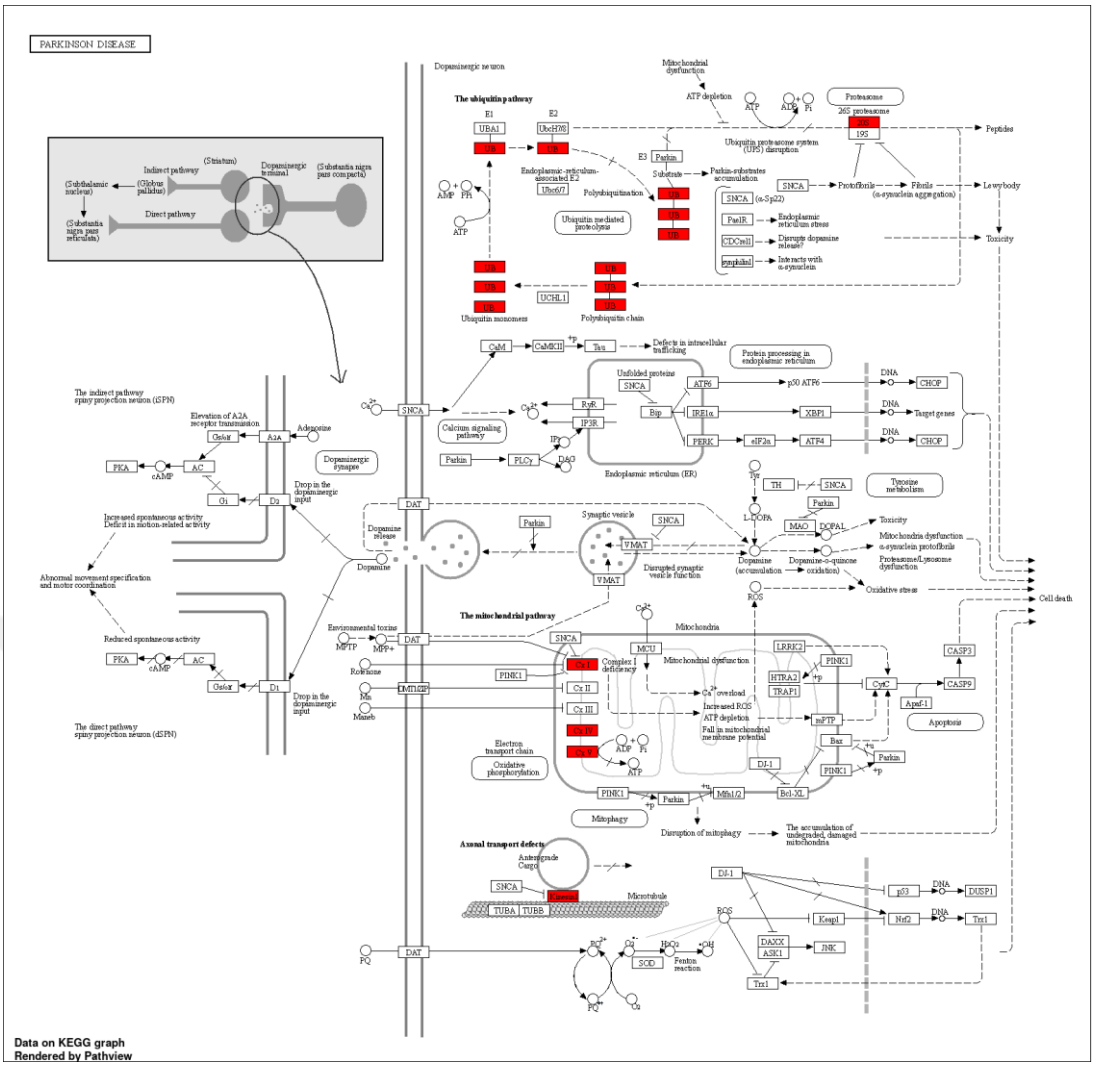

Figure 3.26: KEGG pathway analysis of PD related genes in rutin pretreated, 6-OHDA applied LUHMES-aSyn cells.

Differentiated LUHMES-aSyn cells were pretreated with 10 µM rutin (lower panel) before were treated with 50 µM 6-OHDA and RNASeq analysis was performed compared to vehicle treatment as control (n=3). KEGG pathway analysis was constructed using ShinyGO bioinformatics tool.

3.1.2.7. Common molecular pathways among PD and other Neurodegenerative diseases

Transcriptomic data obtained from 6-OHDA treated LUHMES-aSyn cells were analyzed for discovering possible common degeneration and survival mechanisms between different neurodegenerative conditions. KEGG pathway analysis was done

for pathways of neurodegeneration for multiple diseases. It is found that genes in glutamatergic synapse and calcium signaling pathways were altered (Figure 3.27). Gene expressions of NMDA and AMPA receptors were decreased 0.42 and 0.33 fold changes respectively.

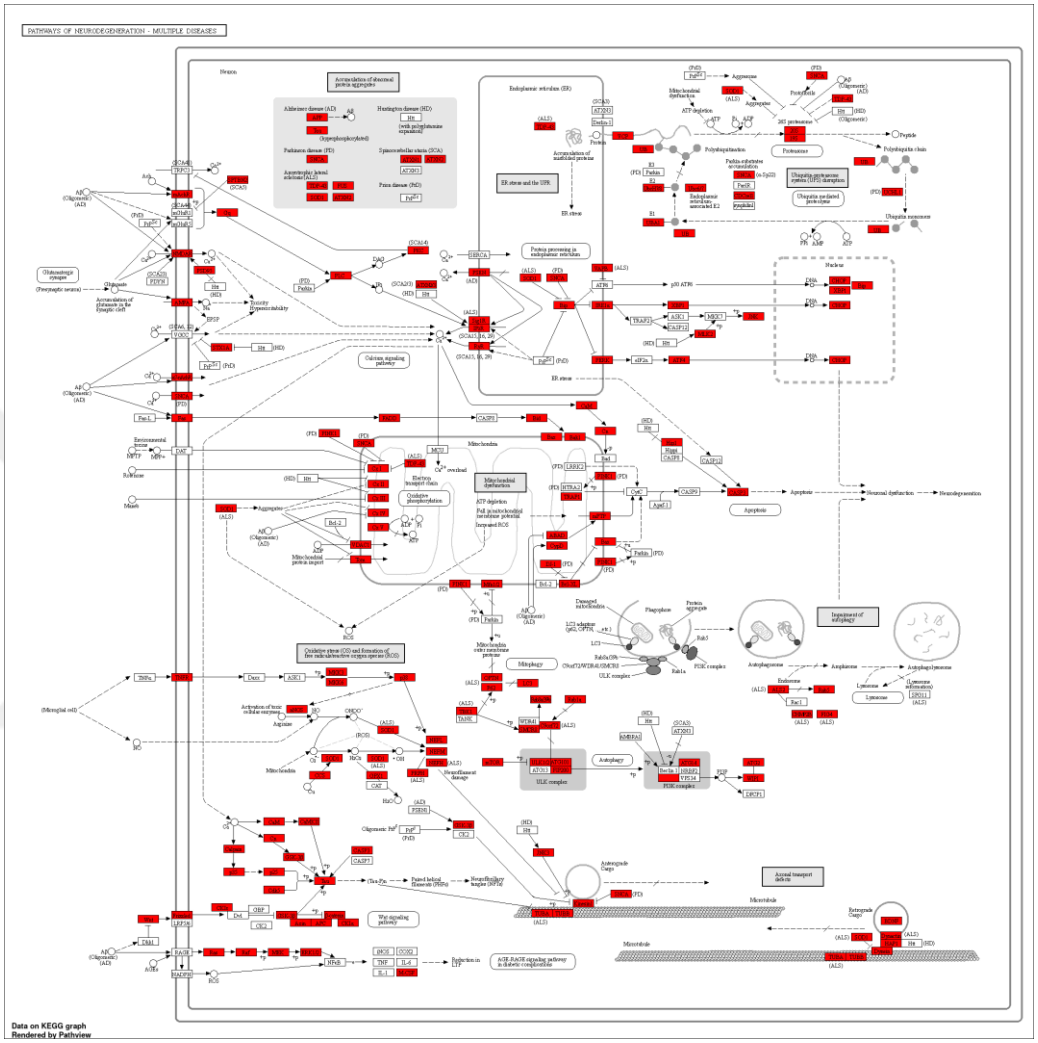

Gene	Ensembl ID	adjusted p value	Fold change
GRIN1	ENSG00000176884	0.005	0.42
GRIN2D	ENSG00000105464	2.61E-4	0.80
GRIN2C	ENSG00000161509	7.20E-4	4.48
GRIA2	ENSG00000120251	2.75E-27	0.33
GRIA4	ENSG00000152578	0.0191	1.86

Figure 3.27: KEGG pathway analysis of genes in neurodegeneration in 6-OHDA treated LUHMES-aSyn cells.

Differentiated LUHMES-aSyn cells were treated with 50 µM 6-OHDA and RNASeq analysis was performed compared to vehicle treatment as control (n=3). KEGG pathway analysis was constructed using ShinyGO bioinformatics tool (upper

panel). Significantly changed gene expression fold changes of NMDA receptor subunits (GRIN1, GRIN2D, GRIN2C) and AMPA receptor subunits (GRIA2, GRIA4) (lower panel).

GO molecular function analysis revealed that ATP binding pathway is altered in 6-OHDA induced PD model in LUHMES-aSyn cells as 1.2-fold enrichment. Purinergic receptors were identified among these molecular pathways and it is found that expression of P2RY1 is increased 2.09-fold change as P2RX5, P2RX3, and P2RX2 receptors decreased 0.64, 0.21 and 0.64 fold changes respectively (Figure 3.28).

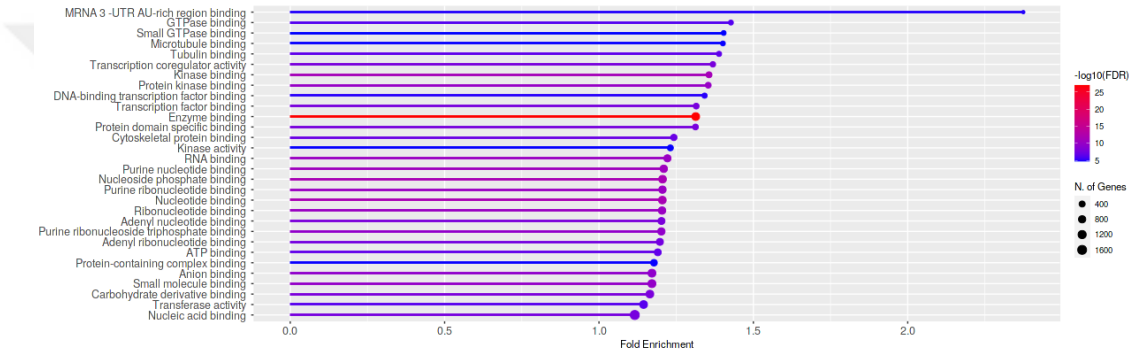

Gene Name	Ensembl ID	adjusted p value	Fold change
P2RY1	ENSG00000169860	0.003	2.09
P2RX5	ENSG00000083454	0.036	0.64
P2RX3	ENSG00000109991	1.62E-50	0.21
P2RX2	ENSG00000187848	0.037	0.64

Figure 3.28: GO molecular function analysis in 6-OHDA treated LUHMES-aSyn cells.

Differentiated LUHMES-aSyn cells were treated with 50 µM 6-OHDA and RNASeq analysis was performed compared to vehicle treatment as control (n=3). GO molecular function analysis was constructed using ShinyGO bioinformatics tool (upper panel). Fold changes and p values of significantly changed genes expressing purinergic receptors (lower panel).

KEGG pathway analysis showed that HD related genes, mainly expressions of glutamatergic pathway, vesicular transport and cytoskeletal components were altered in 6-OHDA induced PD model in LUHMES-aSyn cells, possibly indicating an existence of common mechanisms in the progression of neuropathology (Figure 3.29,

upper panel). Gene expressions of β-tubulin subunits except TUBB6, actin related proteins and dynactin were decreased (Figure 3.29, lower panel).

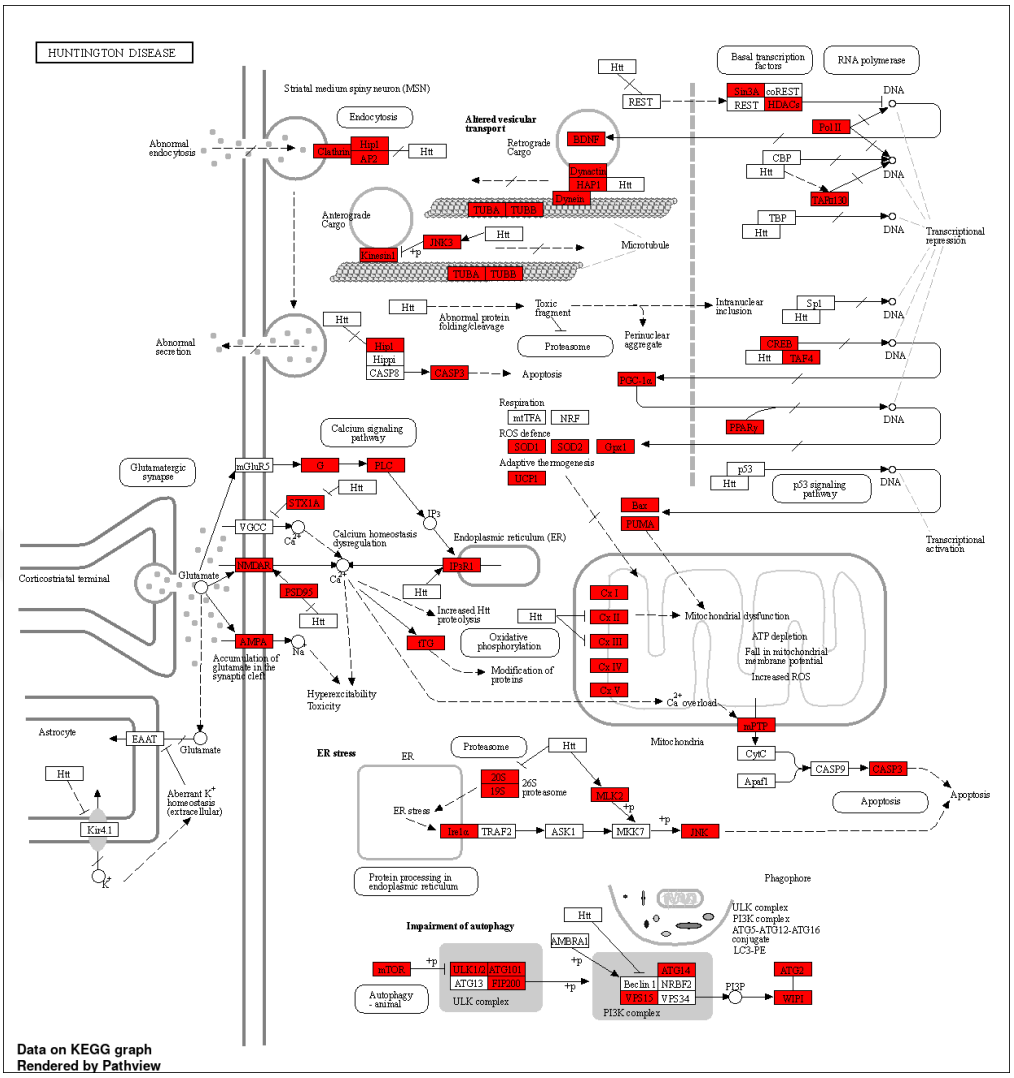

Alpha Tubulin Subunits			
Gene	Ensembl ID	adjusted p value	Fold change
TUBA1B	ENSG00000123416	5.50E-09	0.68
TUBA4A	ENSG00000127824	1.03E-4	1.90
TUBA1A	ENSG00000167552	2.92E-63	0.38
TUBA1C	ENSG00000167553	0.002	1.40
TUBA4B	ENSG00000243910	0.002	21.51

Beta Tubulin Subunits			
Gene	Ensembl ID	adjusted p value	Fold change
TUBB	ENSG00000196230	2.99E-26	0.57
TUBB6	ENSG00000176014	8.01E-06	1.82
TUBB4B	ENSG00000188229	0.009	0.90
TUBB3	ENSG00000258947	1.18E-16	0.65
TUBB4A	ENSG00000104833	9.15E-11	0.60
TUBB2A	ENSG00000137267	4.11E-38	0.52
TUBB2B	ENSG00000137285	1.50E-26	0.62

Actin related proteins			
Gene	Ensembl ID	adjusted p value	Fold change
ACTR1A	ENSG00000138107	3.65E-09	0.73
ACTR1B	ENSG00000115073	8.56E-26	0.50

Dynactin			
Gene	Ensembl ID	adjusted p value	Fold change
DCTN1	ENSG00000204843	1.29E-21	0.65
DCTN3	ENSG00000137100	2.18E-07	0.71

Figure 3.29: KEGG pathway analysis of genes related to HD in 6-OHDA treated LUHMES-aSyn cells.

Differentiated LUHMES-aSyn cells were treated with 50 µM 6-OHDA and RNASeq analysis was performed compared to vehicle treatment as control (n=3).

KEGG pathway analysis was constructed using ShinyGO bioinformatics tool (upper panel). Significantly changed gene expression fold changes of cytoskeletal components and vesicular transport pathway (lower panel).

3.1.3. Calcium activity analysis in 6-OHDA treated primary neurons

KEGG pathway analysis showed that dysregulation of calcium homeostasis is important in the process of progression of PD. To determine the acute effects of 6-OHDA treatment in terms of calcium activity, we recorded spontaneous calcium activities of RCaMP (red calcium indicator) expressing primary neurons before or after 6-OHDA treatment. Calcium imaging revealed that 6-OHDA treatment induced a synchronized burst-like calcium activity in primary neurons at 15 minute of treatment (Figure 3.30).

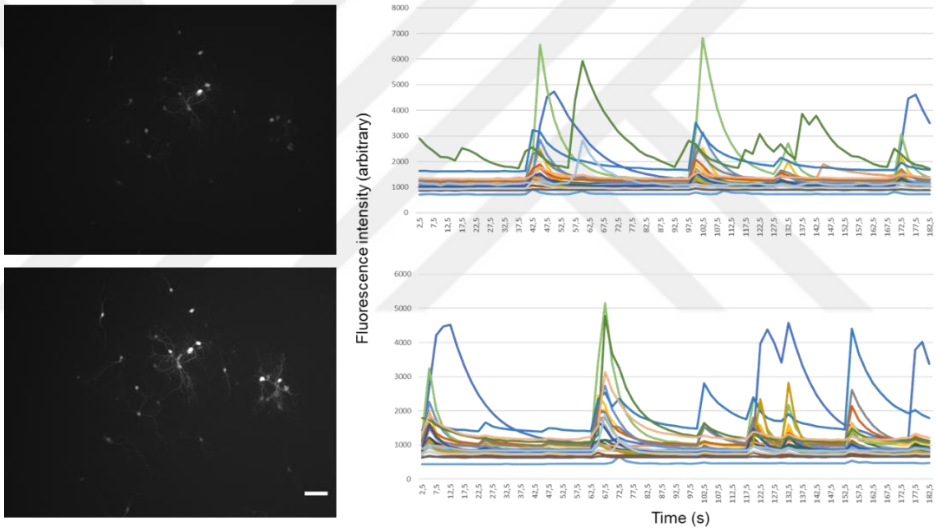

Figure 3.30: Calcium activity analysis before and after 6-OHDA treatment. Primary cortical neurons were isolated from 0-3 days old animals as described in Methods, and transduced with a red calcium indicator AAV-Syn-RCaMP. At 1-week of transduction, fluorescence time lapse images were taken using fluorescence microscope (Zeiss Axio Observer) with 577 nm excitation light for RCaMP (magenta) every 2.5 seconds to record spontaneous activities (upper left and right panel). Cells were treated with 100 µM 6-OHDA and incubated for 15 minutes at physiological conditions. Fluorescence time lapse images were taken from the same area and fluorescence intensities were measured using manual ROI selection with ImageJ for each single neuron and time dependent spontaneous activities were constructed (n=27). Scale bar: 100 µm

3.2. Huntington's Disease

As HD is a monogenic neurodegenerative disorder, it is straightforward to obtain a genetic model. For this reason, mutant Huntingtin (mHtt) expressing *in vitro* models are widely used and can also provide insights for other neurodegenerative diseases with protein aggregations.

3.2.1. Aggregation Profiles of Huntingtin

HEK293T cells were transfected with plasmids expressing either wildtype (Q23) or mutant (Q74) Htt, mutant Htt overexpression was found to result in widespread aggregation in all conditions, whether in complete medium or serum starved conditions (Figure 3.31), as opposed to aSyn overexpression in PD model where no aggregation was observed.

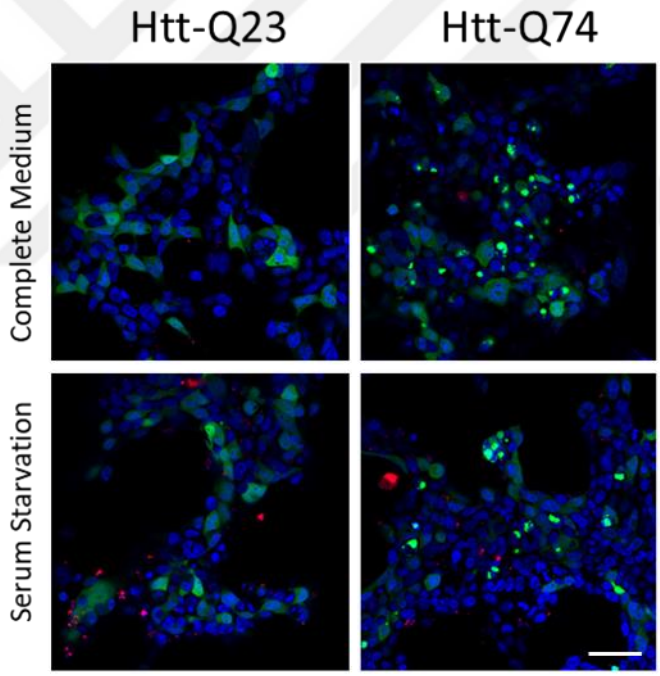

Figure 3.31: Comparison of aggregation profiles of wild type and mutant α-synuclein and Htt in HEK293T cells.

HEK293T cells were transfected expression plasmid encoding either wildtype or Htt (Q23 and Q74 respectively) under either complete medium or serum starvation conditions using 1 % FBS, and imaged with 405 nm and 488 nm excitation lasers using confocal microscope (Zeiss LSM 800) with 40x oil objective (NA:1.4) 120h after transfection. Scale bar: 50 µm

3.2.2. Modelling HD in HEK293T cells

In order to fully study the HD model, HEK293T cells were transfected with EGFP-tagged wildtype (Q23) or mHtt (Q74). EGFP fluorescence in wild-type Htt was found to be diffuse and localized mostly to cytoplasm; on the other hand, mHtt overexpressing cells have exhibited aggregates as depicted by bright and dense EGFP localizations, indicating the sequestration of EGFP-tagged mHtt to the aggregation zones (Figure 3.32).

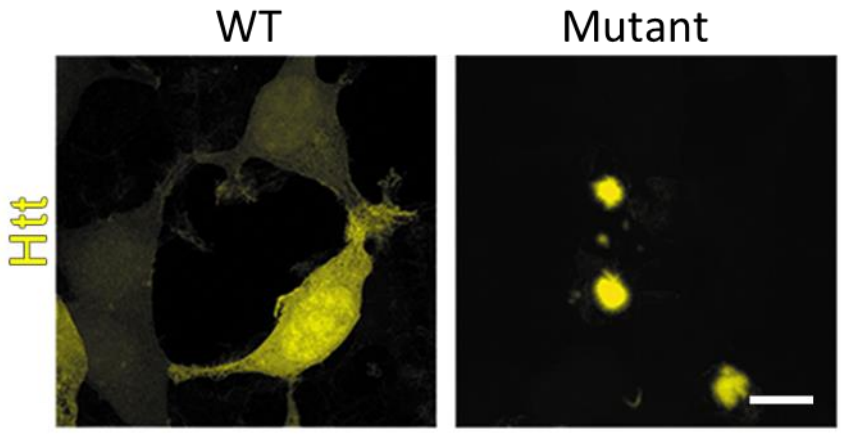

Figure 3.32: Overexpression of EGFP tagged wild-type and mHtt in HEK293T cells. Cells were transfected with either wildtype (Q23) or mutant (Q74) Htt encoding plasmids and imaged 48h after transfection under confocal microscope (Zeiss LSM 880) using 40x oil objective (NA:1.4) with 488nm excitation laser. Scale bar: 10 µm

3.2.2.1 Live imaging of mHtt aggregate formation

To observe mHtt aggregate formation in real time, HEK2393T cells were then transfected with EGFP-Q74 plasmid and time lapse images were taken every 10 min. Most of the aggregates were found to be accumulated in cytoplasm of HEK293T cells, and these cells with mHtt aggregates have mostly died during the course of time lapse imaging (Figure 3.33).

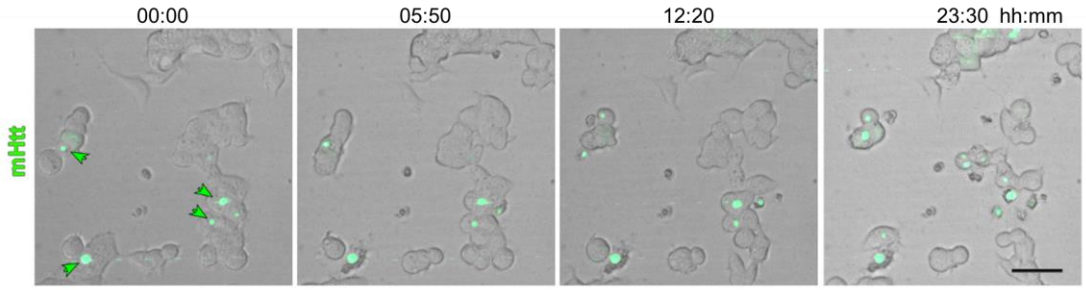

Figure 3.33: Live imaging of mHtt overexpressing HEK293T cells. HEK293T cells were transiently transfected with mHtt and time lapse images were taken at 24h of transfection using spinning disk confocal microscope (Zeiss Spinning Disk) with 10 min interval. EGFP tagged mHtt (green) is accumulated into subcellular aggregates in time. Cells with mHtt aggregates are depicted as green arrows. Scale bar: 50 µm

3.2.2.2 Ultrastructural properties of mHtt aggregates and surrounding cellular environment

We have then determined to observe mHtt aggregates in electron microscope via label-free approach to study the ultrastructural properties of these cells. In this assay, aggregates were depicted as electron-dense regions composed of complex membranous and filamentous structures. In addition, electron microscopy images and corresponding segmentations revealed increased mitochondrial accumulation and ER network around mHtt aggregates, which could be due to disrupted organelle trafficking around the microenvironment of aggregates (Figure 3.34).

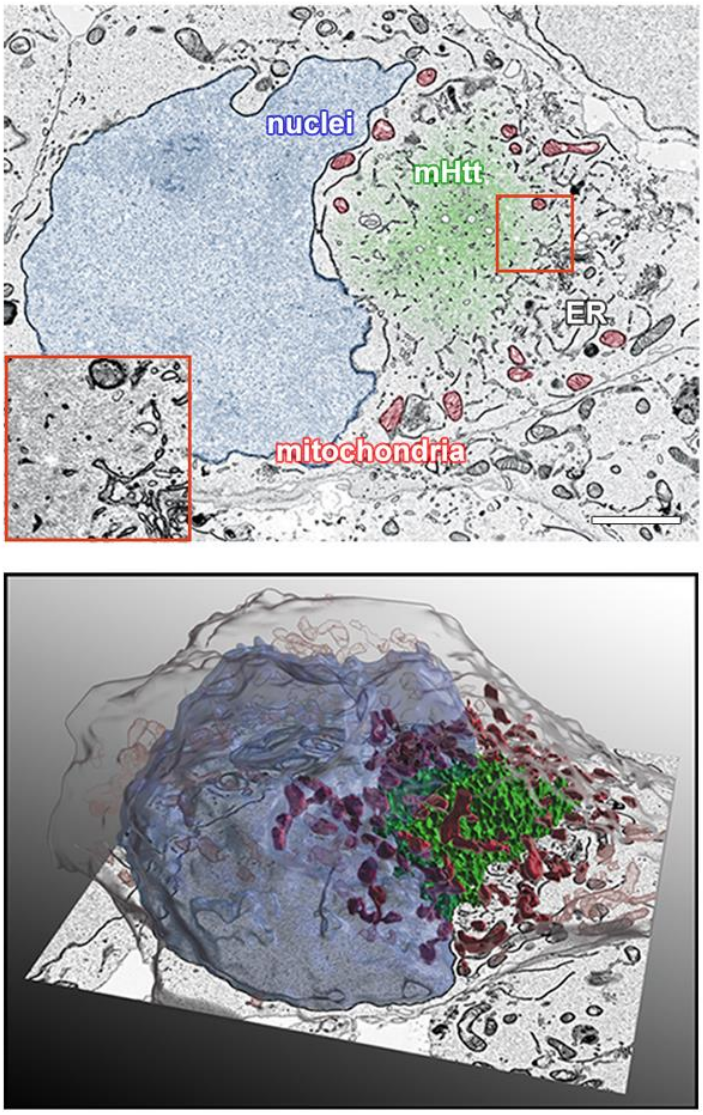

Figure 3.34: EM image and corresponding segmentation of a mHtt overexpressing HEK293T cell.

HEK293T cells were transiently transfected with expression plasmids encoding wild-type and mHtt. mHtt aggregates were identified as dense EGFP signals as described before and imaged with electron microscope (Zeiss Gemini SEM 500) using 3.00 kV accelerating voltage and backscatter detector with 6.00 K X magnification and 4096 x 3072 resolution. Perinuclear mHtt aggregate (green) can be observed in EM image as a complex filamentous and fibrillary structure with surrounding mitochondrial accumulation (red) and ER network (black) (upper panel). Red insert shows the close up image of the aggregate with visible fibrillary structures. Segmentation of mitochondria, aggregates and nuclei indicates accumulation of mitochondria near mHtt aggregate (lower panel). Scale bar: 2 µm

3.2.2.3 Correlation of mHtt aggregates with cytoskeletal components

Huntingtin protein function is not clear, although a range of functions from transactivation, vesicle trafficking and axonal transport have been proposed. In this thesis, we have investigated how mutant mHtt protein interacted with cytoskeletal elements. In order to characterize filamentous structures accompanying mHtt aggregates, mHtt-overexpressing HEK293T cells were fixed and stained with antibodies against cytoskeletal components. β-tubulin and vimentin immunoreactivities were determined to be higher at the site of aggregates. Vimentin was highly colocalized to mHtt aggregates but β-tubulin was not. Phalloidin staining showed that F-actin immunoreactivity was increased at the periphery of aggregates but not directly colocalized to mHtt (Figure 3.35).

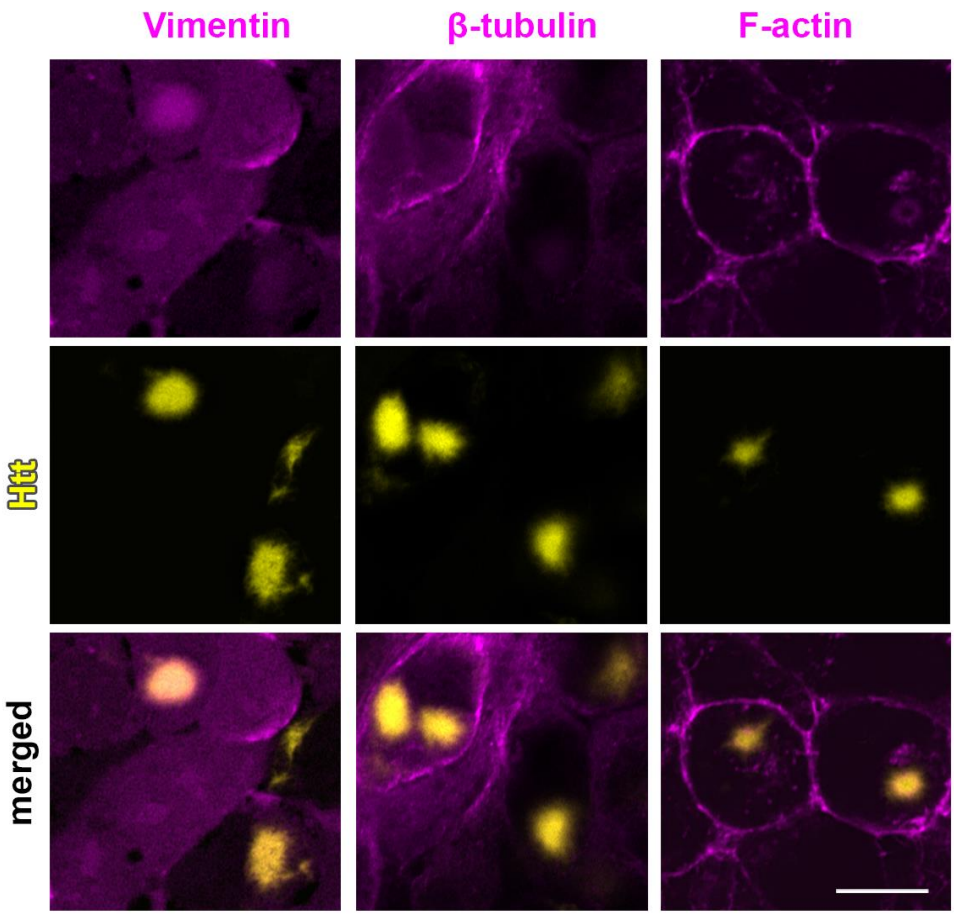

Figure 3.35: Immunoreactivities of cytoskeletal components in mHtt overexpressing HEK293T cells.

HEK293T cells were transiently transfected with expression plasmids encoding mHtt and fixed 48h after transfection. Fixed cells were stained with mouse anti-

Vimentin, rabbit anti-β-tubulin primary antibodies following Alexa Fluor Plus 555 goat anti-rabbit and Alexa Fluor Plus 647 goat anti-mouse secondary antibodies and phalloidin for F-actin detection. Immunostained cells were imaged with confocal microscope (Zeiss LSM 880) using 40x oil objective (NA:1.4) with 633 nm and 543 nm excitation lasers. Colocalization of mHtt aggregates (yellow) with cytoskeletal components (magenta) were determined using Pearson correlation analysis (n>3) (Pearson correlation coefficients: Vimentin:0.69, β-tubulin: 0.039, F-actin: -0.08.). Scale bar: 10 µm

Since intermediate filament protein vimentin was found to be colocalized with mHtt aggregates, and it was previously shown to modify mHtt aggregation (Bauer et al 2012), we wanted further to investigate its interaction with mHtt aggregates in ultrastructural detail. For this purpose, we cotransfected HEK293T cells with mHtt and miniSOG-Vimentin. Cotransfected cells were fixed, photo-oxidized and vimentin presence within mHtt aggregates was verified as dark spots (Figure 3.36).

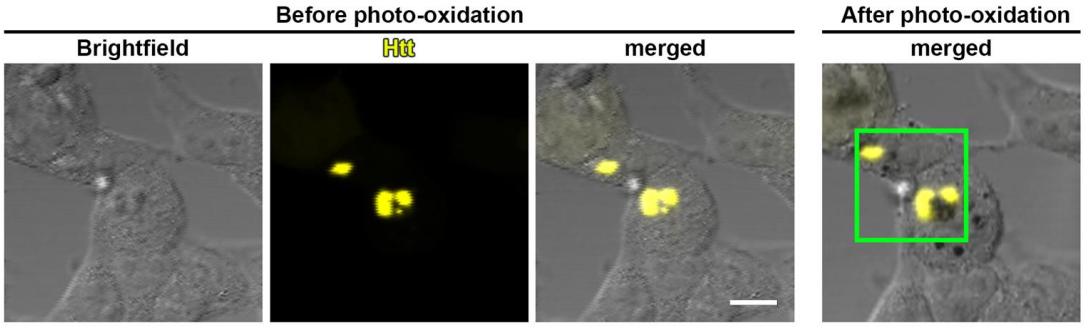

Figure 3.36: Photo oxidation of miniSOG tagged Vimentin in mHtt aggregates. HEK293T cells were cotransfected with expression plasmids encoding mHtt and Vimentin-miniSOG.

Cells were imaged at 48h of transfection with confocal microscope (Zeiss LSM 880) using 40x oil objective (NA:1.4). mHtt aggregates are localized in fixed HEK293T cells and photooxidation is performed using 488 nm LED light (Colibri) using 40x oil objective for 1-2 min. Vimentin-miniSOG expression is confirmed via dark spots detected in brightfield images. Scale bar: 10 µm

Next, ultra-thin sections were taken from labelled cells and colocalization of vimentin with mHtt aggregates was confirmed via electron micrographs. EM images

showed that vimentin proteins were indeed intertwined into mHtt aggregates (Figure 3.37).

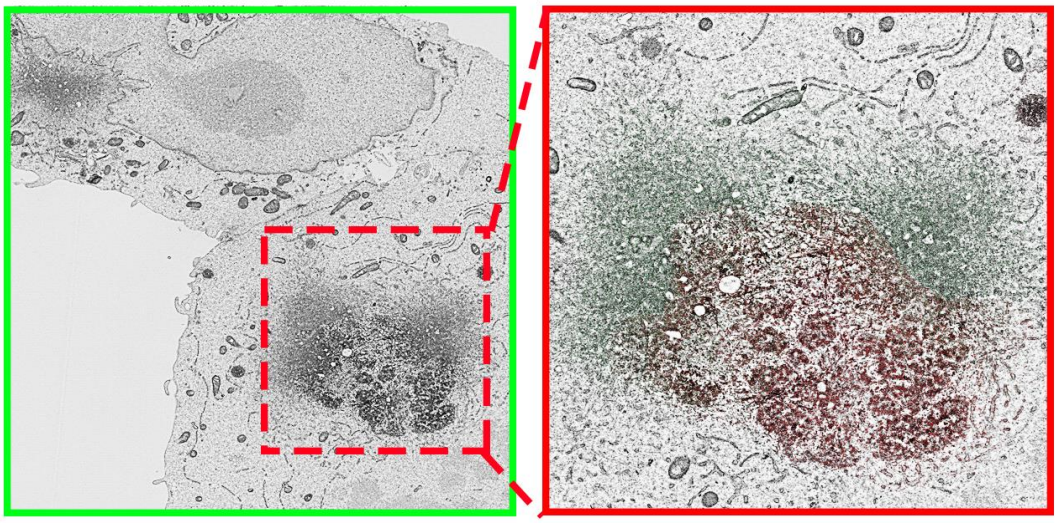

Figure 3.37: Representative EM image of miniSOG tagged Vimentin (red) with mHtt aggregate (green) in HEK293T cells.

HEK293T cells were cotransfected with plasmids encoding mHtt and Vimentin-miniSOG and electron microscopy (Zeiss Gemini SEM 500) images were taken at 48h of transfection using 3.00 kV accelerating voltage and backscatter detector with 6.00 K X magnification and 4096 x 3072 resolution. EM image of HEK293T cell with a mHtt aggregate with vimentin expression detected as electron dense regions caused by photooxidized miniSOG.

3.2.2.4 Live imaging of mHtt aggregate interaction with filamentous actin

To further investigate F-actin accumulation around mHtt aggregates, we have cotransfected HEK293T cells with mHtt and Lifeact-tdTom and time lapse images were taken during mHtt aggregation process. We have observed that 43.67± 1.03 % of total mHtt aggregates were surrounded with F-actin 24h after transfection (t=0) which increased to 71.98± 0.80 % 4 hr after (Figure 3.38). In addition, it was found that mHtt aggregates that have F-actin accumulation around them are larger in volume compared to those that do not (Figure 3.38).

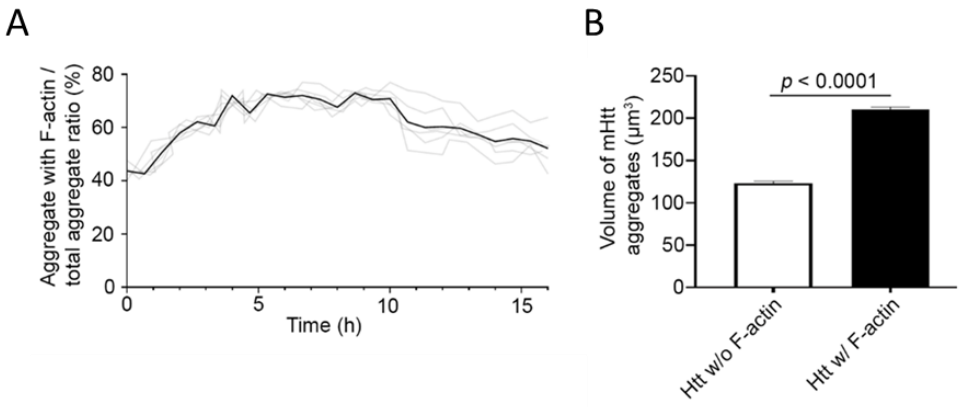

Figure 3.38:Time dependent F-actin accumulation and volume analysis of mHtt aggregates.

HEK293T cells were cotransfected with plasmids encoding mHtt and LifeAct-tdTom and Z-stack time lapse images were taken for a total of 15hrs. with 40 min intervals. after 24h of transfection (t=0). aggregates containing F-actin accumulation are increased during time lapse imaging. A) mHtt aggregates with F-actin accumulation are larger in volume compared to mHtt aggregates without F-actin. Aggregates with F-actin percentages were calculated for each time point (n=6). B) Volumetric analysis was done using segmentation and p value was determined using t-test (n>500).

Using fluorescence time-lapse imaging, we found that F-actin accumulation towards the center of the cells is prominent in mHtt aggregate zones even before the aggregation is visible. F-actin intensity in HEK293T cells without mHtt aggregates is observed in periphery of the cell and centrifugal accumulation was not present (Figure 3.39).

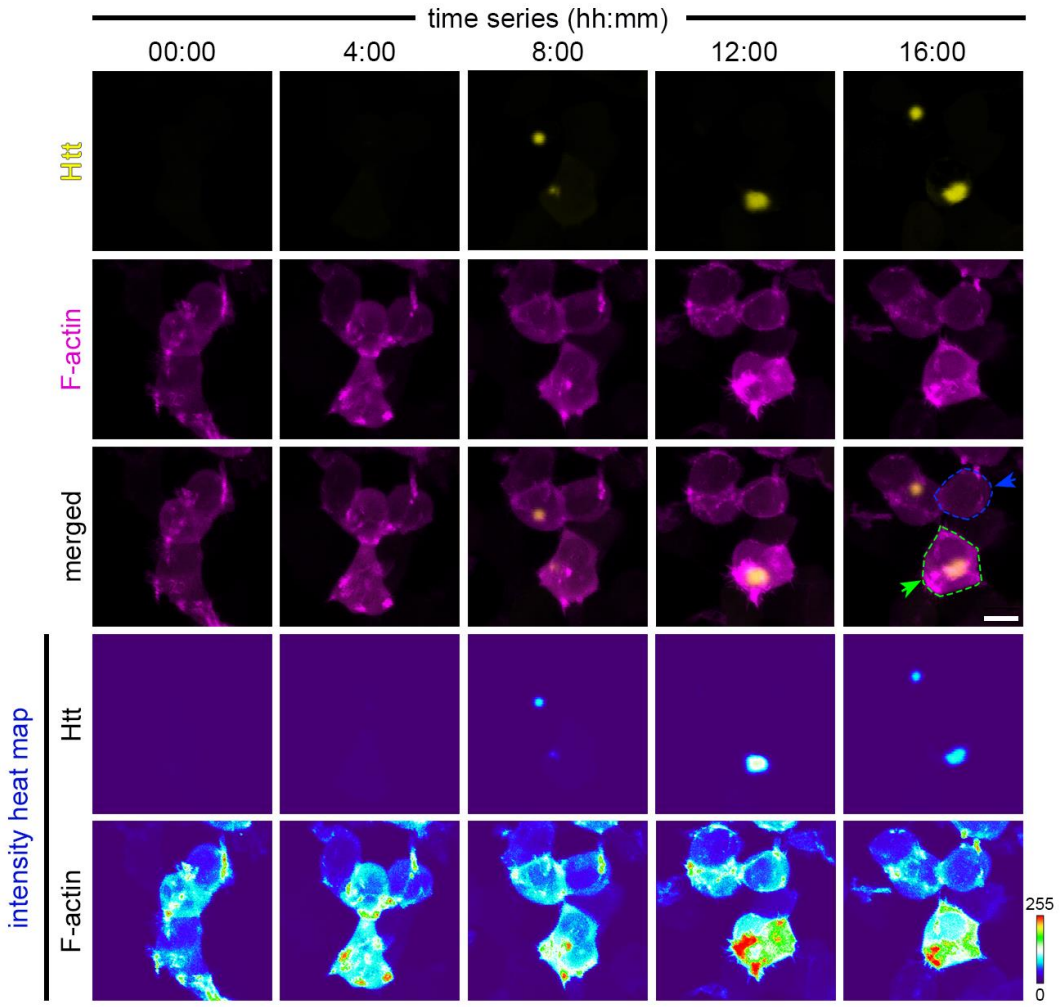

Figure 3.39: Fluorescence time lapse imaging and heat map representation of F-actin accumulation during mHtt aggregate formation in HEK293T cells. HEK293T cells were cotransfected with plasmids encoding mHtt (yellow) and LifeAct-tdTom (magenta). Time lapse images were taken during the course of aggregate formation using confocal microscope (Zeiss LSM 880) and 20x objective (NA:0.8) with 488 nm and 543 nm excitation lasers. Fluorescence intensity heat map is constructed for each channel with red and dark blue. Cell with mHtt aggregate is denoted with green dashed line and cell without mHtt aggregate is denoted with blue dashed line. Scale bar: 10 µm

Next, we investigated if F-actin accumulation in mHtt aggregation zone is due to relocalization of actin filaments from the periphery. Time lapse imaging and distance to cell membrane analysis revealed that peripheral F-actin was indeed transported from cell membrane to aggregate zones during the aggregation process (Figure 3.40, Figure 3.41). To that end, we have first calculated the distance of F-actin

and Htt proteins from cell membrane as described in the Methods section. In control cells that do not overexpress mHtt, we have observed that the distance of F-actin from membrane does not greatly increase over time, indicating that most of the actin filaments are membrane-proximal, while cells overexpressing mHtt exhibit F-actin relocation away from the membrane, even before Htt accumulation is observed (Figure 3.39, Figure 3.40).

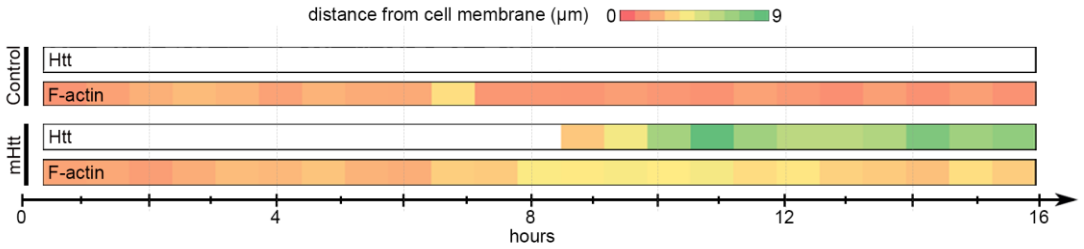

Figure 3.40: Distance to cell membrane analysis of F-actin in HEK293T cells with mHtt aggragates compared to control cells.

HEK293T cells were either cotransfected with plasmids encoding mHtt protein (mHtt-GFP) with LifeAct-tdTom or not transfected (control) and imaged for 16 hr. Distance to cell membrane is calculated by determining the closest distance of F-actin rich spots to cell perimeter and was represented on 0-9 um scale over time.

We have further studied the relocation of F-actin by time lapse imaging and segmentation analysis, where possible routes for F-actin relocalization to mHtt aggregate zones were identified (Figure 3.41).

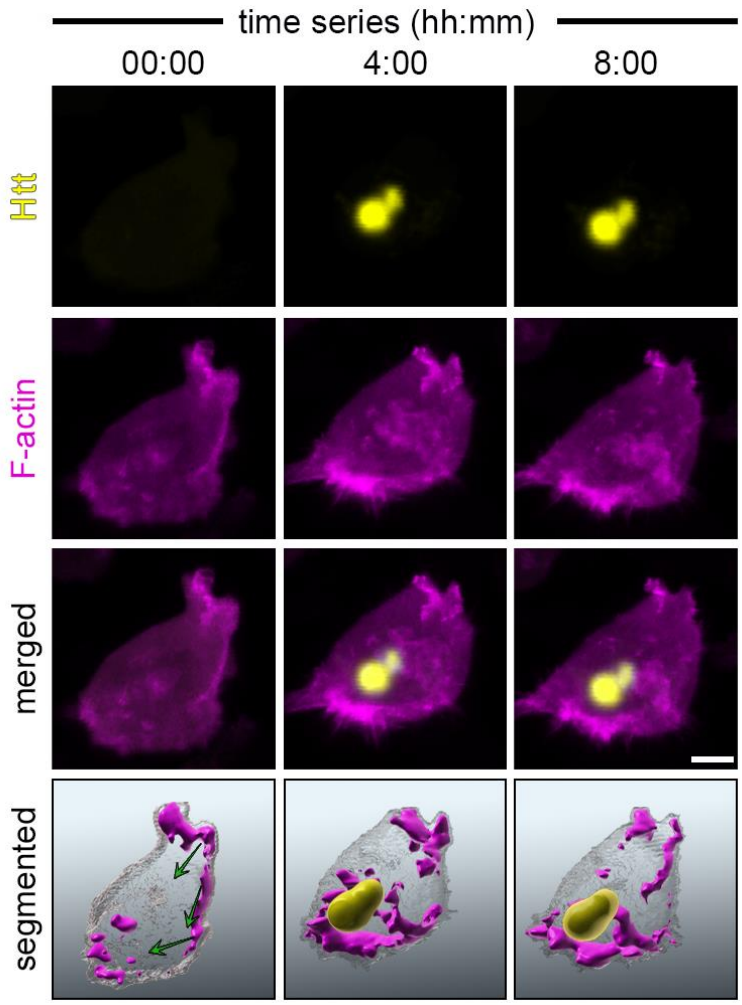

Figure 3.41: Relocation of F-actin from cell membrane to mHtt aggregation zone.

High resolution image (upper three panels) and segmentation (bottom panel) of mHtt (yellow) and F-actin (magenta) in LifeAct- and mHtt-cotransfected HEK293T cells. F-actin is relocated from cell membrane to mHtt aggregation zone. Green arrows in the segmentation panel indicate possible transportation route of actin filaments. Scale bar: 5 µm

3.2.2.5 Ultrastructure of mesh-like F-actin structure surrounding mHtt aggregates and mitochondria

Given these findings, we have hypothesized that F-actin accumulation around mHtt aggregates may also cause disruption in organelle trafficking. To that end we have carried out correlative light and electron microscopy (CLEM) in LifeAct- and

mHtt-cotransfected HEK293T cells. EM images showed that F-actin that has relocalized from membrane to aggregate zone has formed a mesh-like structure around mHtt aggregates; we have further observed mitochondria-rich zones in these cells in close proximity to mHtt aggregates (Figure 3.42).

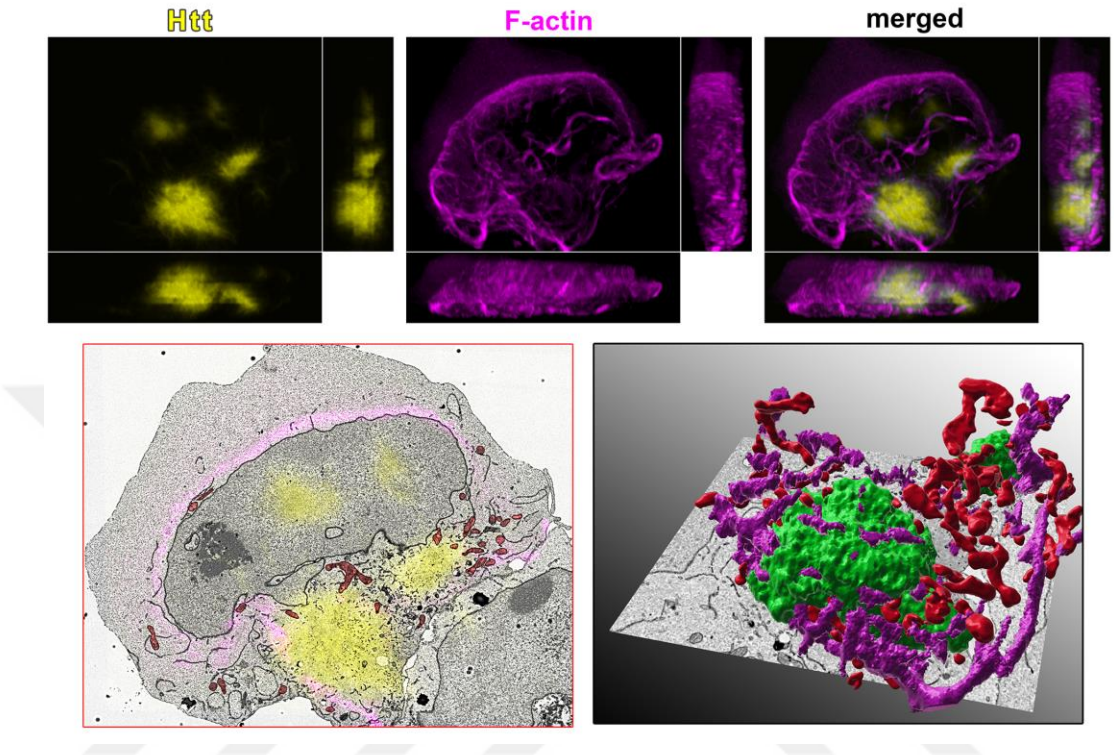

Figure 3.42: Ultrastructural imaging and segmentation of mHtt aggregate (green), mitochondria (red) and F-actin (magenta).

Correlative light and electron microscopy (CLEM) in LifeAct- and mHtt-cotransfected HEK293T cells (upper panels). EM image (yellow: mHtt aggregate, red: mitochondria, magenta: F-actin) and segmentation (green: mHtt aggregate, red: mitochondria, magenta: F-actin) of mHtt aggregate in HEK293T cell.

3.2.2.6 Effect of Elk1 overexpression in mHtt aggregate formation and F-actin dependence

Since Elk1 overexpression was found to have a neuroprotective effect in our PD model, we have also investigated whether it exhibited a similar protective effect in HD model, and whether such a neuroprotection could be through affecting the process of mHtt aggregate formation. To that end, HEK293T cells were transfected with plasmids expressing Elk1 or its phospho mutants (S324A, S383A, T417A), and mHtt protein (Figure 3.43). Similar to PD model, we further wanted to investigate how this function

related to the timing of disease onset, by transfecting Elk-1 expression plasmids either before, during or after mHtt expression plasmid transfection (Figure 3.43). Multiple tile scan images are taken from Hoechst stained cells, aggregates are analyzed and calculated values are normalized against mock transfections in each group.

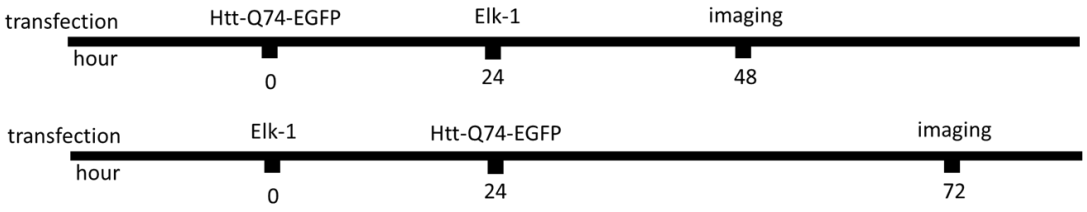

Figure 3.43: Timeline of mHtt and Elk1 cotransfections.
Elk1 and its different phospho-mutants are overexpressed in HEK293T cells before or after mHtt overexpression.

Our analyses have shown that transfection of Elk-1 expression plasmid 24 hr after transfection with mHtt expression plasmid did not affect aggregate number, while overexpression of Elk-1 S324A and S383A phosphomutants but not wildtype Elk-1 when transfected 24 hr before mHtt transfection decreased the total number of aggregates (Figure 3.44A vs B, respectively).

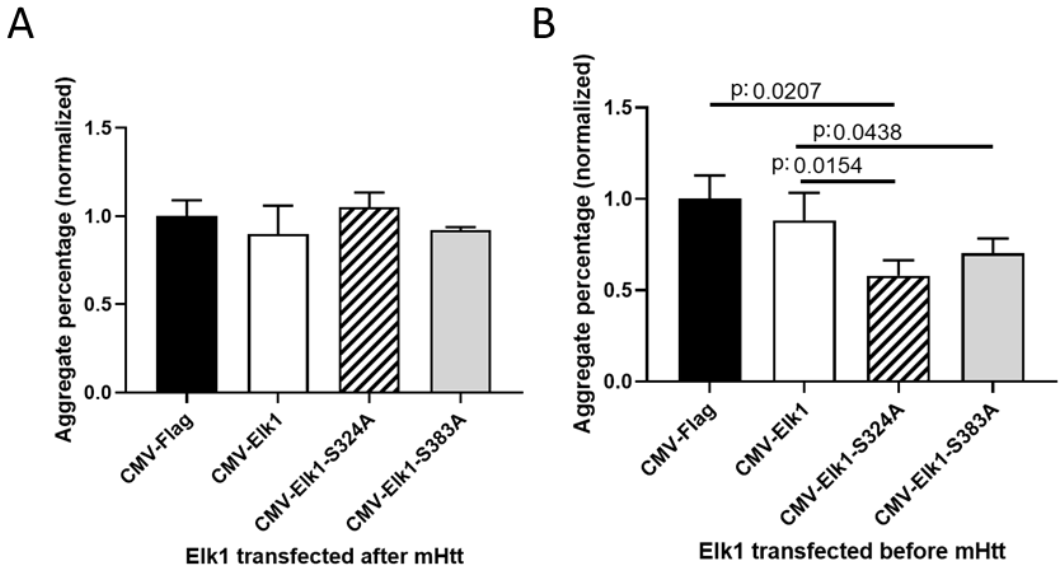

Figure 3.44: Total number of mHtt aggregates normalized against total cell numbers.

HEK293T cells were transfected with plasmids encoding either wildtype or phosphomutants of Elk-1 (A) 24 hr after transfection with mHtt expressing plasmid or (B) 24 hr before transfection with mHtt expressing plasmid. Aggregate numbers per cell were determined for 5000< cells for a total of 25 field of view (5x5), and 3 biological replicates. P values were calculated according to the mean percentage values of each biological replicate using t-test.

To determine if the decline in number of aggregates is correlated with expression level of wildtype or mutant Elk-1 proteins, Western blot experiments were performed. We have found that there was no significant change in mHtt accumulation in cells when Elk-1 plasmids were transfected 24 hr after mHtt expression plasmid was transfected to the cells (Figure 3.44). However, when Elk1-S324A phosphomutant was transfected before mHtt transfection, the levels of mHtt protein aggregation was significantly lower than those in mock-transfected cells or cells transfected with wildtype of S383A mutant Elk1 (Figure 3.45). S324 motif of Elk-1 has been determined previously in our laboratory to be target for mitotic kinases (Ari Uyar et al, submitted manuscript), hence the neuroprotective effect of this phosphomutant is intriguing and needs to be further investigated to understand the relation of Elk-1 phosphorylation and mHtt aggregation.

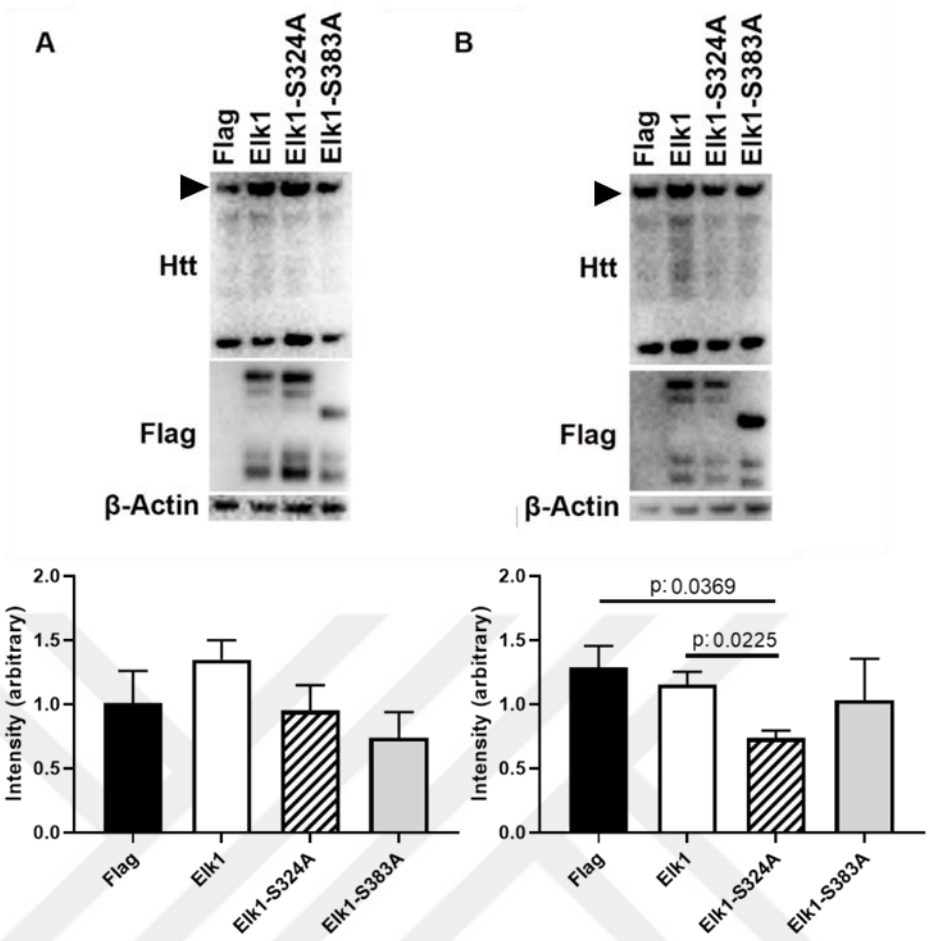

Figure 3.45: Protein expression levels in Elk1- and mHtt- cotransfected HEK293T cells.

A) Expression plasmids for wildtype Elk1 or its phosphomutants were transfected 24h after cells were transfected with mHtt expression plasmid. Western blot analysis was carried out, and Htt protein levels were normalized to those of β-actin and p values were quantified using t-test (n>2). Western blot for Flag antibody was carried out as Elk-1 transfection control. B) Expression plasmids for wildtype Elk1 or its phosphomutants were transfected 24h before cells were transfected with mHtt expression plasmid. Western blot analysis was carried out, and Htt protein levels were normalized to those of β-actin and p values were quantified using t-test (n>2). Western blot for Flag antibody was carried out as Elk-1 transfection control.

As subcellular localization of Elk1 has previously been shown to change depending on its phosphorylation state in mitotic cells [109], (Arı Uyar et al, in submission), and since in neurons both cytoplasmic and nuclear localization of Htt aggregates were observed in HD, we have next analyzed the subcellular colocalization

of mHtt aggregates where plasmids encoding Elk-1 isoforms have been transfected to the cells either before or after mHtt transfection, however we have not observed any significant changes under either condition (Figure 3.46).

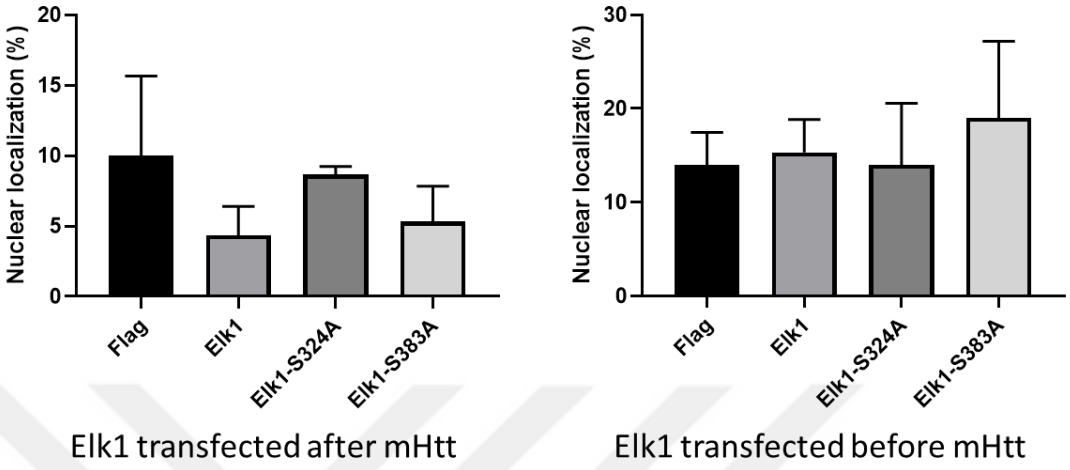

Figure 3.46: Nuclear localization of mHtt in HEK293T cells.

Expression plasmids for wildtype Elk1 or its phosphomutants were transfected either (A) 24 hr after or (B) 24h before cells were transfected with mHtt expression plasmid. Cells were stained with Hoechst and images were taken using confocal microscope (Zeiss LSM 780) under 40x oil objective (NA:1.4) with 488 nm and 405 nm excitation lasers. Segmentations were done for both Hoechst stained nucleus and EGFP tagged mHtt aggregates and nuclear localization were determined using surface to surface interaction. The percentages of nuclear aggregates were calculated with respect to total number of aggregates in each field of view and p values were determined using t-test (n=3).

Next, we have sought to analyze whether there was a relationship between Elk-1 overexpression and the previously determined F-actin caging of mHtt aggregates. To that end, HEK293T cells were cotransfected first with expression plasmids encoding Elk-1 isoforms, and 24 hrs after with plasmids encoding LifeAct-tdTom and mHtt. Neither Elk-1 nor its phosphomutants did not have any significant effect on the volume of mHtt aggregates (Figure 3.47A), although total mHtt protein levels were previously shown to decrease when Elk-1-S324A was overexpressed (Figure 3.47B). Furthermore, no significant changes were determined in the number of F-actin-associated aggregates in cells (Figure 3.47B).

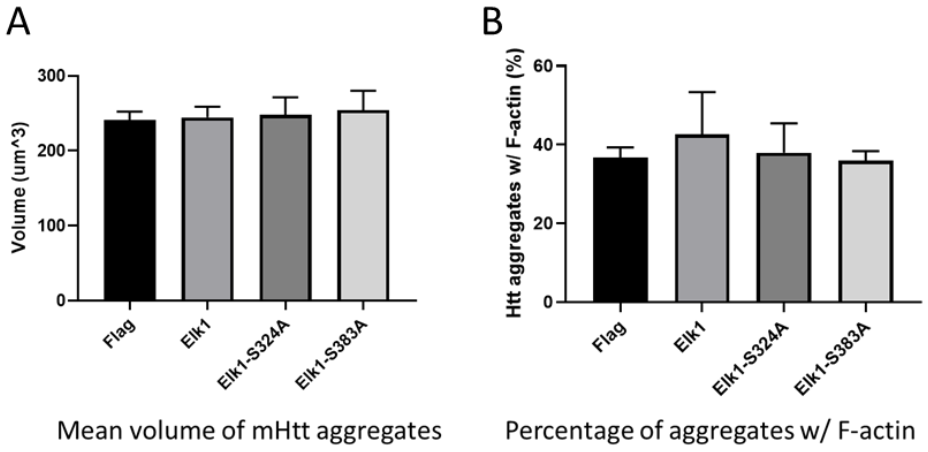

Figure 3.47: Aggregation and F-actin analysis in Elk1 overexpressed HEK293T cells.

Expression plasmids for wildtype Elk1 or its phosphomutants were transfected 24h before HEK293T cells were cotransfected with mHtt and LifeAct-tdTom expression plasmids. A) Aggregate volumes were calculated by segmentation of EGFP tagged mHtt aggregates and statistical analysis was done using t-test (n=3) B) Segmentation of EGFP tagged mHtt aggregates and tdTom tagged F-actin. Surface to surface analysis was done to calculate percentage of Htt aggregates associated with F-actin and statistical analysis was done using t-test (n=3)

3.2.3. Modelling HD in primary neurons

In order to validate our results in a more physiologically relevant HD model, we have overexpressed EGFP-tagged wildtype and mutant Htt in primary cortical and hippocampal neurons. Similar to our results in HEK293T cells, wildtype Htt was found to exhibit a diffuse signal, indicating no toxic oligomerization in cells, while mHtt formed into the aggregates that are hallmarks of HD, however the aggregate formation pattern was different from HEK293T cells (Figure 3.32, Figure 3.48). mHtt in HEK293T cells tend to form singular/larger aggregates as cortical or hippocampal neurons do not show a simple pattern and exhibit multiple aggregates.

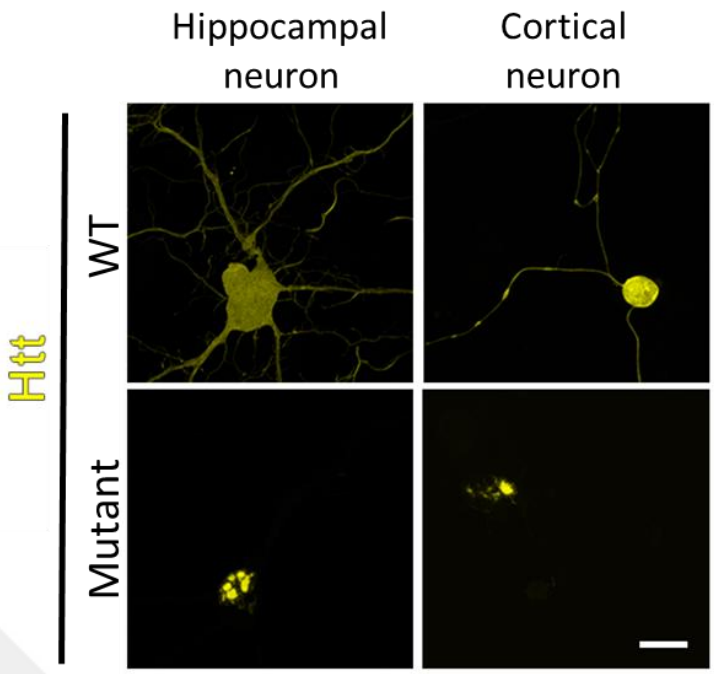

Figure 3.48: Overexpression of wild type and mHtt in hippocampal and cortical neurons.

Primary hippocampal and cortical neurons were isolated from 0-3 day old animals as described in Methods, and transfected with plasmid expressing wildtype or mutant Htt using lipofectamine 2000. Cells were imaged 24 hr after transfection using confocal microscope (Zeiss LSM 880) with 488 nm excitation laser. Scale bar: 10 µm

3.2.3.1 Localization of mHtt aggregates and its relation with cell type dependent distribution of F-actin

We have next carried out a series of analyses in order to make detailed comparison of *in vitro* HD models with primary neurons vs cell lines. To that end, we have first analyzed nuclear vs cytoplasmic Htt aggregate numbers in both primary cortical and hippocampal neuron models. Aggregates in neurons were found to be mostly localized into nucleus (over 60 %) compared to HEK293T cells (14.00 % ± 2.00) (data taken from Figure 3.46). Interestingly, cortical neurons have significantly higher percentage of nuclear aggregates (89.66 % ± 1.85) compared to those in hippocampal neurons (75.85 ± 4.09 %) (Figure 3.49).

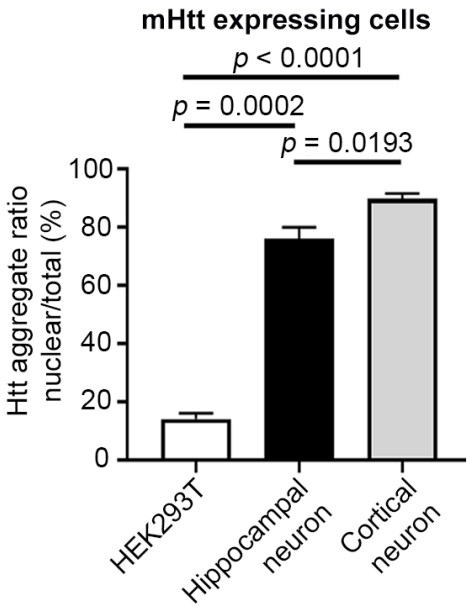

Figure 3.49: Nuclear mHtt aggregate distribution in HEK293T cells, hippocampal and cortical neurons.

Primary hippocampal and cortical neurons were isolated from 0-3 day old animals as described in Methods, and transfected with plasmid expressing wildtype or mutant Htt using lipofectamine 2000. Cells were stained with Hoechst 24 hr after transfection and imaged using confocal microscope (Zeiss LSM 880) using 405 nm and 488 nm excitation lasers. Aggregates in both nuclear and cytoplasmic compartments were determined through segmentation of EGFP tagged mHtt aggregates and Hoechst stained nucleus from at least 5 number of fields per experiment, in at least 3 repeats of experiments; and percentage of nuclear aggregates were then calculated per cell nuclei and biological replicates (n=3) were used for determination of p values using t-test.

When a more detailed study was performed in both HEK293T cell line and primary cell models, it was found that aggregates were more fragmented and smaller in primary neurons as compared to those in HEK293T cells, where aggregates were larger and generally clustered in one focal point (Figure 3.50).

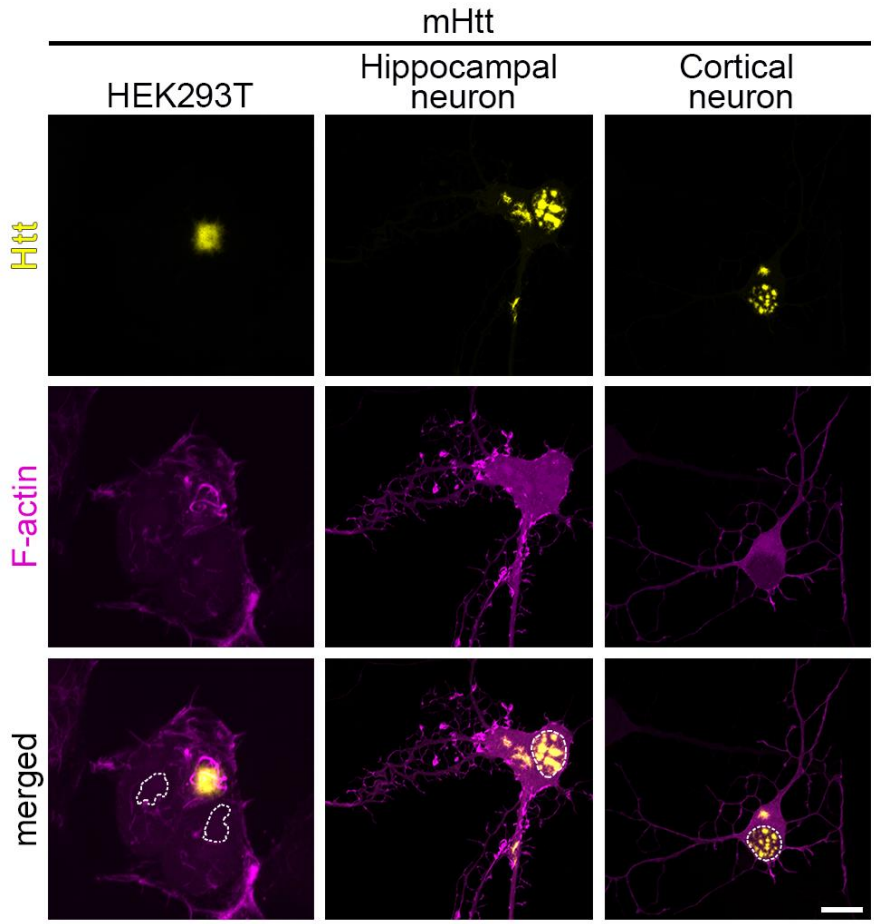

Figure 3.50: LifeAct and mHtt expression in HEK293T cells, hippocampal and cortical neurons.

Primary hippocampal and cortical neurons were isolated from 0-3 day old animals as described in Methods, and cotransfected with plasmids expressing mutant Htt and LifeAct-tdTom using lipofectamine 2000; HEK293T cells were transfected with the same plasmids using PEI. Cells were imaged 24 hr after transfection using confocal microscope (Zeiss LSM 880) for F-actin (tdTomato fluorescence at 543 nm; magenta) and Htt (GFP fluorescence at 488 nm; yellow). Nucleus are circled with dashed lines in merged images. Scale = 5 µm

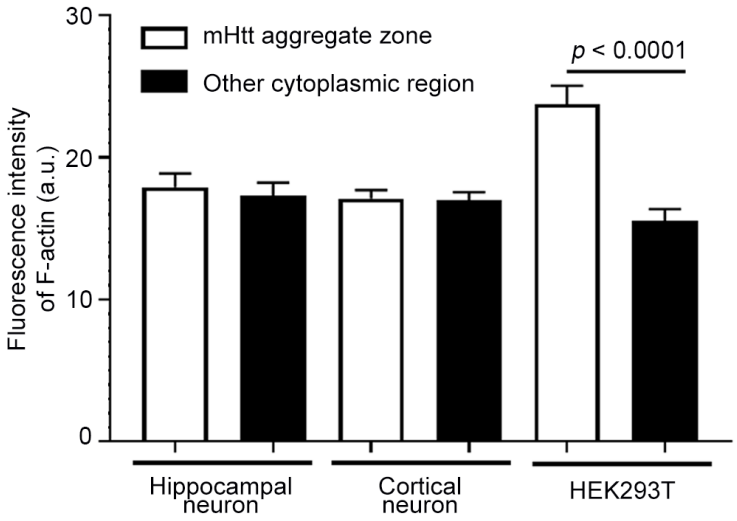

Figure 3.51: F-actin accumulation near mHtt aggregates.

Primary hippocampal and cortical neurons were isolated from 0-3 day old animals as described in Methods, and cotransfected with plasmids expressing mutant Htt and LifeAct-tdTom using lipofectamine 2000; HEK293T cells were transfected with the same plasmids using PEI. Cells were imaged 24 hr after transfection using confocal microscope (Zeiss LSM 880) for F-actin (tdTomato fluorescence at 543 nm; magenta) and Htt (GFP fluorescence at 488 nm; yellow). Nucleus are circled with dashed lines in merged images. F-actin intensity associated with mHtt aggregates in aggregate zones (white bars) vs other cytoplasmic regions (black bars) were analyzed and quantified for each single cell (n=20). Statistical analysis was carried out using t-test.

We have next analyzed whether the profile of F-actin association of aggregates was different in primary neurons as compared to HEK293T cells. To that end, we have transfected both HEK293T cell line and primary neurons with mHtt and LifeAct-tdTom expression plasmids and 24 hr after transfection we have analyzed the F-actin intensity that is associated with aggregate zones as well as that in other cytoplasmic regions. Our analysis has revealed that cytoplasmic aggregates in neurons did not exhibit the mesh-like structure of actin filaments observed in HEK293T cells (Figure 3.50, Figure 3.51).

Since one of the major structural differences between HEK293T cells and primary neurons is the neuronal morphology in the latter, we have next investigated whether axonal vs somatic aggregation profiles were different among the two primary

neuron models. We have observed that primary hippocampal neurons had axonal aggregates while cortical neurons don't (Figure 3.50). Axonal aggregates in hippocampal cells have F-actin accumulation (Figure 3.50). We thought that this cell type dependent differences may be arisen from the F-actin distribution in healthy cells. Analysis of subcellular distribution of F-actin in cortical and hippocampal neurons revealed that hippocampal neurons have significantly higher axonal F-actin ratio compared to cortical neurons in both wild-type Htt or mHtt overexpression conditions (Figure 3.52).

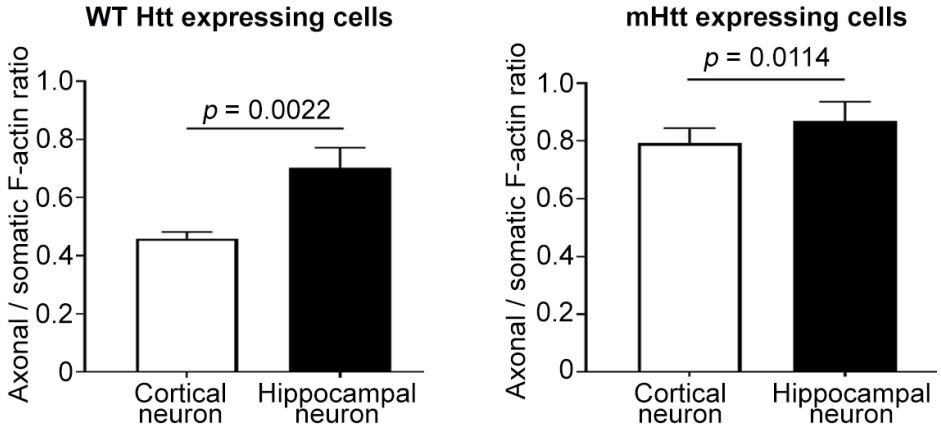

Figure 3.52: Axonal F-actin ratio in cortical and hippocampal neurons.

Primary hippocampal and cortical neurons were isolated from 0-3 day old animals as described in Methods, and cotransfected with plasmids expressing mutant Htt and LifeAct-tdTom using lipofectamine 2000. Cells were imaged 24 hr after transfection using confocal microscope (Zeiss LSM 880) for F-actin (tdTomato fluorescence at 543 nm; magenta) and Htt (GFP fluorescence at 488 nm; yellow). Wildtype or mutant Htt expressing cells were determined from the EGFP fluorescence intensity. Axonal and somatic F-actin intensities (total) were analyzed from LifeAct-tdTom fluorescence using manual ROI selection in ImageJ. Statistical analysis was done for each single cell and p values are quantified using t-test (n>3).

In addition to F-actin distribution differences (axonal/somatic F-actin ratio) among different types of neurons, we wanted to investigate F-actin expression level differences in HEK293T cells and neurons. As transfection efficiencies of each cell differs from each other, we stained cells with phalloidin and performed F-actin

intensity analysis. F-actin intensity analysis revealed that HEK293T cells have significantly higher F-actin expression compared to hippocampal neurons both in their cytoplasm or membrane (Figure 3.53).

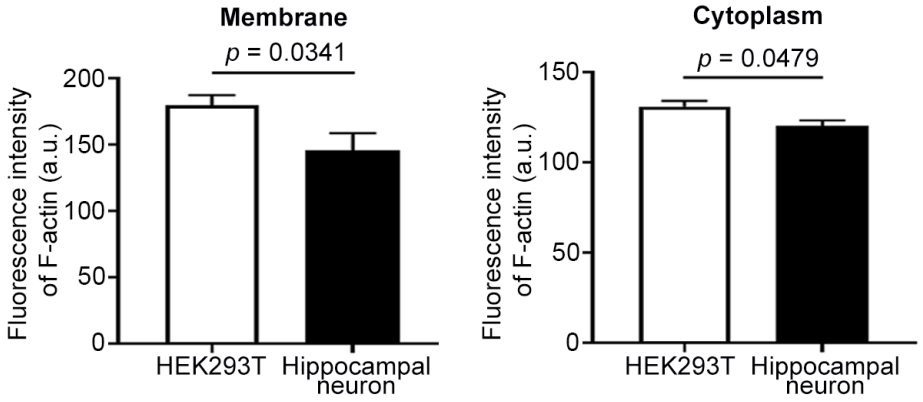

Figure 3.53: F-actin intensity analysis in HEK293T cells and hippocampal neurons.

HEK293T cells and primary hippocampal neurons were fixed and stained with phalloidin to determine F-actin intensities. Stained cells were imaged using confocal microscope (Zeiss LSM 880) with 543 nm excitation laser using 40x oil objective (NA:1.4). Cell membranes and cytoplasm were selected manually using ImageJ and fluorescence intensities were measured for each single cell. P values were determined using t-test (n>5).

3.2.3.2 Motility analysis of axonal mHtt aggregates

As axonal mHtt aggregates are correlated with F-actin intensity, we wanted to investigate the formation of axonal aggregates and F-actin accumulation in real time. Time lapse motility analysis revealed that, axonal mHtt aggregates have higher velocity at the start of their formation and as they get bigger and sequestered together (indicated as increased fluorescence intensity), their velocity is decreased. Decrease in velocity is negatively correlated with fluorescence intensity of axonal mHtt aggregates (Figure 3.54).

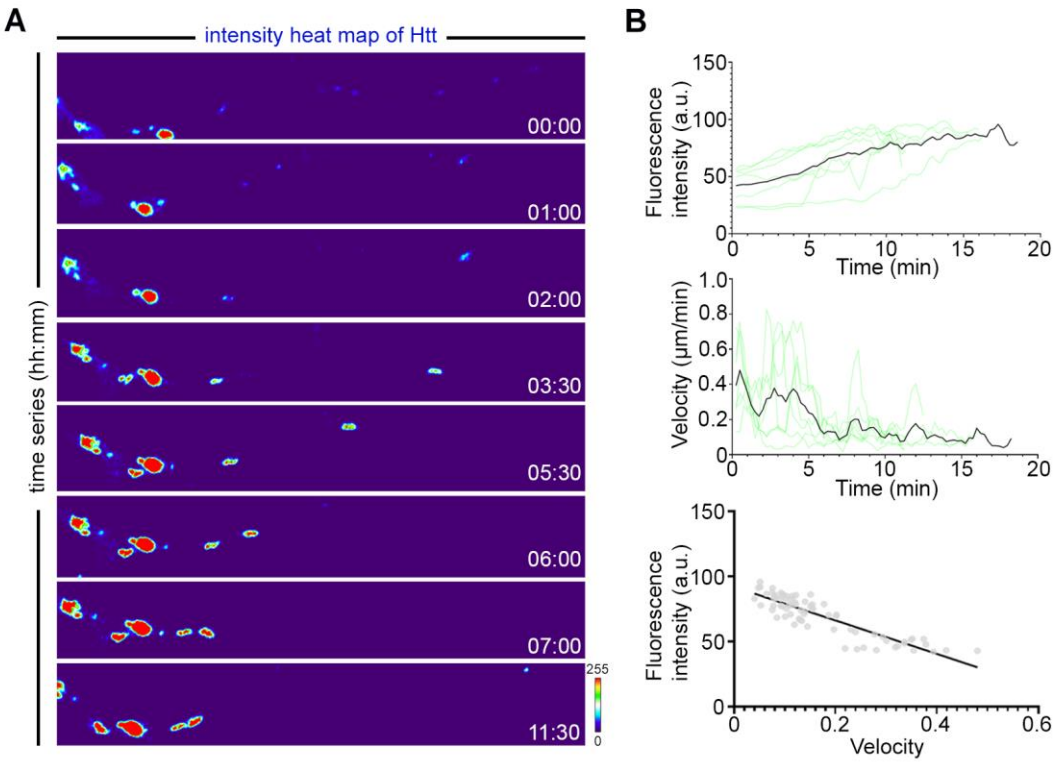

Figure 3.54: Motility analysis of axonal mHtt aggregates.

Primary hippocampal neurons were isolated from 0-3 day old animals as described in Methods, and cotransfected with plasmids expressing mutant Htt using lipofectamine 2000. Time lapse images were taken 24 hr after transfection using confocal microscope (Zeiss LSM 880) for F-actin (tdTomato fluorescence at 543 nm; magenta) and Htt (GFP fluorescence at 488 nm; yellow). mHtt aggregates were tracked by Track Mate plugin of ImageJ. A) Fluorescence intensity heat map was constructed using EGFP channel in ImageJ and represented for each time frame. B) Fluorescence intensities were measured over time for each tracked mHtt aggregate and velocities of were measured as travelled distance (μm) over time (min) (n=7).

As mHtt aggregates are sequestered together and grow larger, F-actin and mHtt aggregates are accumulated into axonal varicosities (Figure 3.55A). Time dependent fluorescence intensity of mHtt and F-actin are positively correlated (Figure 3.55B).

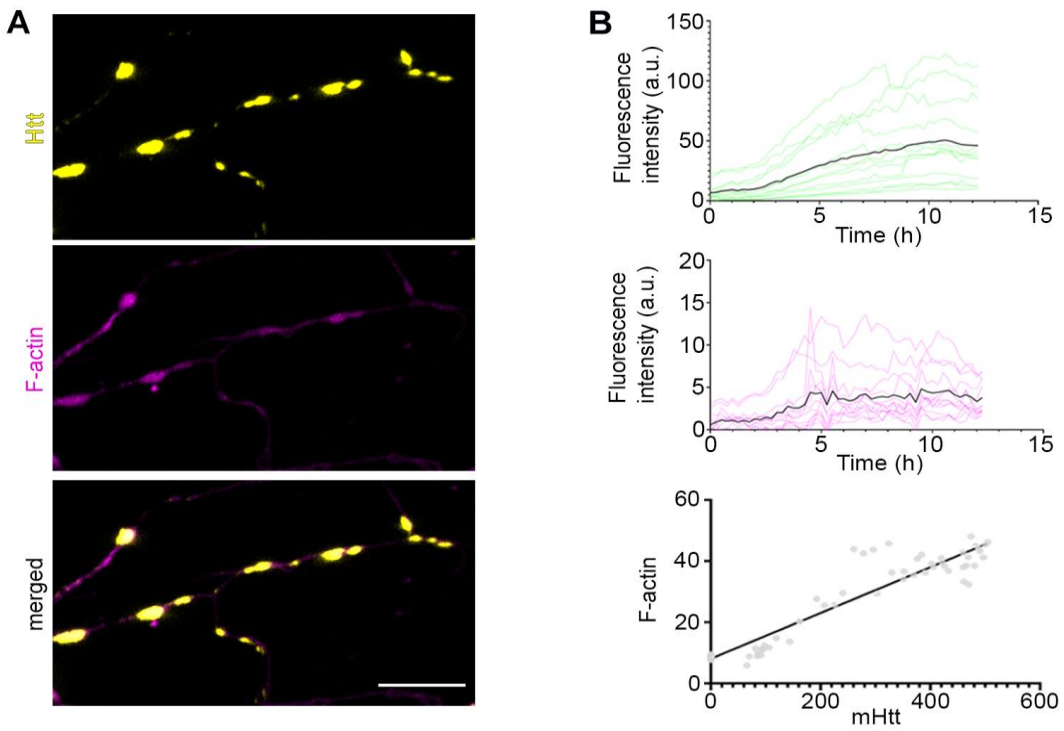

Figure 3.55: mHtt and F-actin accumulation into axonal varicosities. Primary hippocampal neurons were isolated from 0-3 day old animals as described in Methods, and cotransfected with plasmids expressing mutant Htt and LifeAct-tdTom using lipofectamine 2000. Time lapse images were taken 24 hr after transfection using confocal microscope (Zeiss LSM 880) for F-actin (tdTomato fluorescence at 543 nm; magenta) and Htt (GFP fluorescence at 488 nm; yellow). mHtt aggregates were tracked by Track Mate plugin of ImageJ and fluorescence intensity analysis was done for both channel to determine colocalization. A) Fluorescence image indicating colocalization of mHtt aggregation (yellow) and F-actin (magenta) accumulation. B) Fluorescence intensities of EGFP and tdTomato channels were measured over time for each tracked mHtt aggregate (n=11). Scale bar: 10 µm

3.2.3.3 Ultrastructural properties of Axonal mHtt aggregates

We further wanted to determine if co-accumulation of mHtt with F-actin disrupts axonal organelle trafficking. For this purpose, we took ultra-thin sections from hippocampal cells. EM images revealed increased mitochondrial accumulation near mHtt and F-actin aggregates similar to those seen in HEK293T cell cytoplasm (

Figure **3.56**).

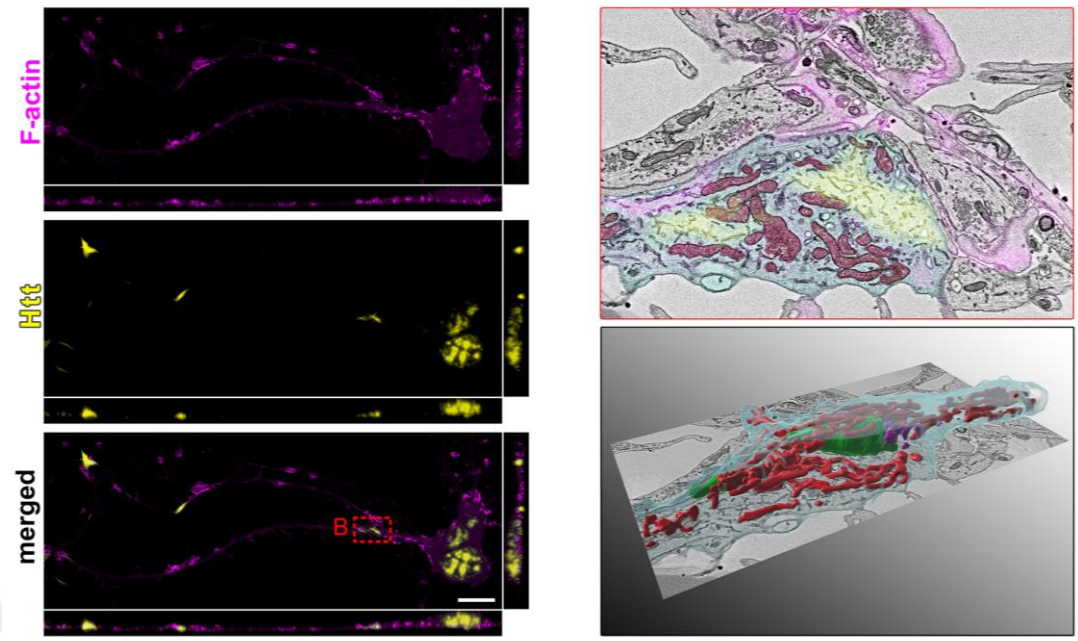

Figure 3.56: Ultrastructural imaging and segmentation of axonal mHtt in hippocampal cells.

Primary hippocampal neurons were isolated from 0-3 days old animals as described in Methods, and cotransfected with plasmids expressing mutant Htt and LifeAct-tdTom using lipofectamine 2000. Fluorescence images were taken 24 hr after transfection using confocal microscope (Zeiss LSM 880) with 543 nm excitation laser for F-actin (magenta) and 488 nm excitation laser for mHtt (yellow), followed by fixation and preparation for correlative electron microscopy. A) Fluorescence image (left panel) and corresponding EM image (right, upper panel) and segmentation (right, lower panel) of axonal aggregates (yellow in fluorescence and EM image, green in segmentation), F-actin (magenta) and mitochondrial accumulation (red) in axonal varicosities. Scale bar: 10 µm

3.2.3.4 Using mHtt overexpressing neurons as TND model

Our studies have shown that mHtt aggregates were not dissolved or lost in time, instead it was observed that they stayed as immotile and/or insoluble bulk components even after neurons or HEK293T cells degenerated and eventually died (Figure 3.57). We have hypothesized that this phenomenon may contribute to the spread of degeneration. To investigate this, we have transfected hippocampal neurons with mHtt and carried out imaging using confocal microscope (Zeiss LSM 880). We have then

taken tile scan images from mHtt overexpressing primary neurons 1 week after transfection. Astrocytes were left in the culture as transfected or untransfected neurons appeared unhealthy (Figure 3.58). We propose that the results of this study indicates that mHtt aggregates released from dying cells induce spreading degeneration in the surrounding cells, which will be discussed further in the next chapter.

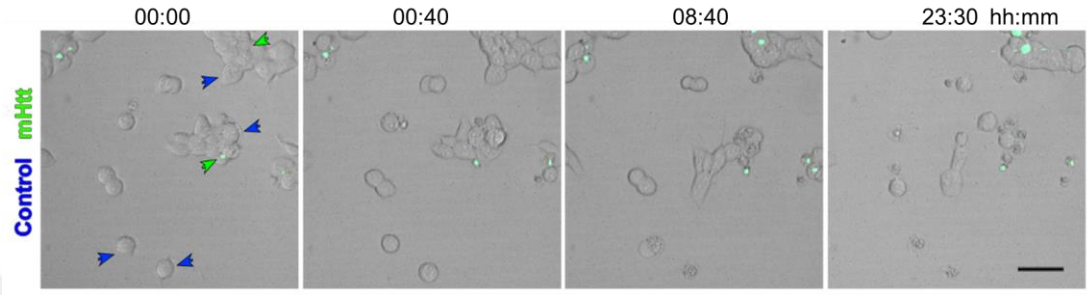

Figure 3.57: Spreading degeneration observed in mHtt overexpressing HEK293T cells.

HEK293T cells were transfected with mHtt and time lapse images of cells with mHtt aggregates (green arrowheads) and cells without mHtt aggregates (blue arrowheads) were taken 24h after transfection using spinning disk confocal microscope (Zeiss Spinning Disk). Scale bar: 50 µm

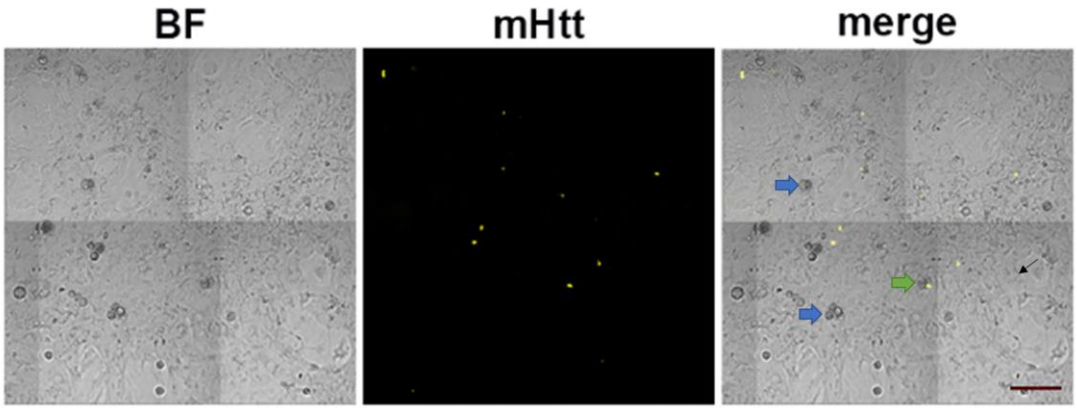

Figure 3.58: mHtt aggregates present 1-week after formation of mHtt aggregates in hippocampal neurons.

Hippocampal neurons (blue and green arrows) and astrocytes (black arrow) cells were imaged 1-week after formation of mHtt aggregates. Neurons with (green arrow) or without aggregates (blue arrow) were observed to be unhealthy. Scale bar: 100um

3.2.3.5 Calcium Activity Analysis in response to Wildtype and Mutant Htt Overexpression

Calcium excitotoxicity is known to play a crucial role in the process of spreading of neurodegeneration. To determine if overexpression of mHtt alters calcium activity in primary neurons, we transduced primary neurons with AAV-Syn-RCaMP and transfected RCaMP expressing primary neurons with plasmids encoding wild type or mutant Htt. Calcium imaging revealed that spontaneous activity of naïve neurons neighboring to mHtt overexpressing cells is altered compared to wildtype Htt overexpressing cells (Figure 3.59). Spontaneous activity frequency is increased in neurons neighboring mHtt overexpressing cells and they exhibit a synchronized behavior (Figure 3.60).

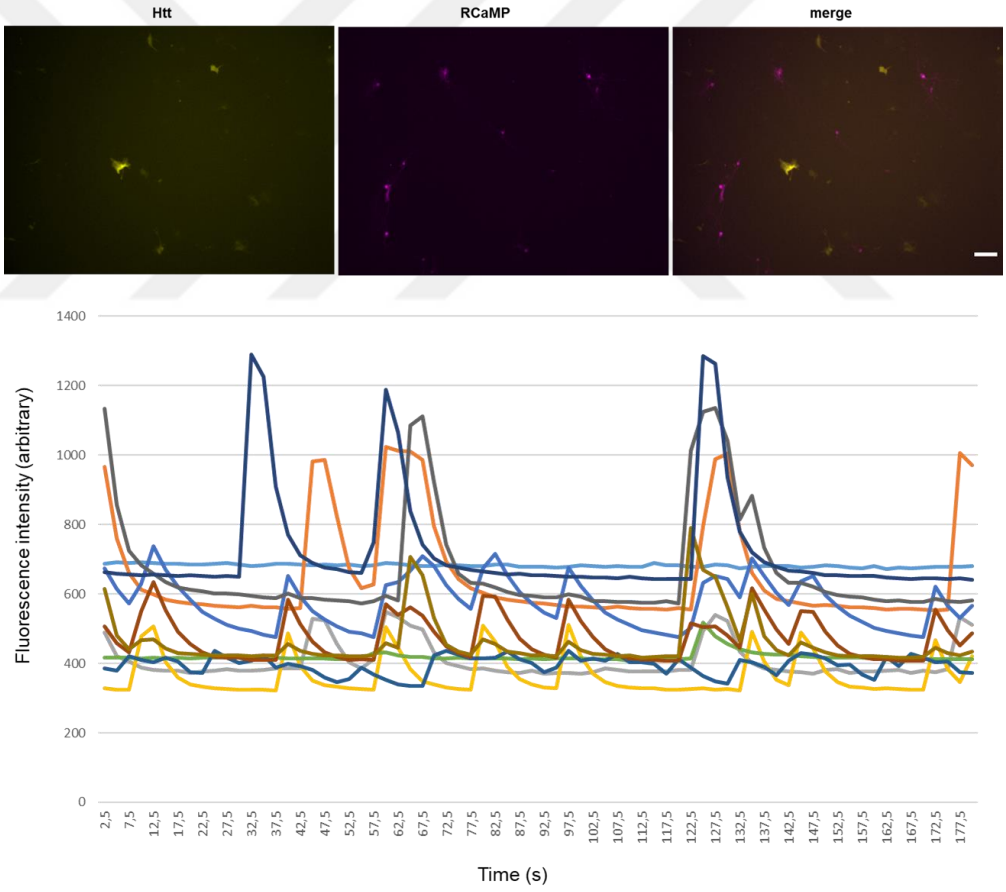

Figure 3.59: Spontaneous calcium activity of neurons neighboring wildtype Htt expressing cells.

Primary cortical neurons were isolated from 0-3 days old animals as described in Methods, and transduced with a red calcium indicator AAV-Syn-RCaMP. At 1-

week of transduction, cells were transfected with plasmids encoding wildtype Htt using lipofectamine 2000. Fluorescence time lapse images were taken 24 hr after transfection using fluorescence microscope (Zeiss Axio Observer) with 577 nm excitation light for RCaMP (magenta) and 488 nm excitation light for mHtt (yellow) every 2.5 seconds (upper panel). Fluorescence intensities were measured using manual ROI selection with ImageJ for each single neuron and time dependent spontaneous activities were constructed (n=11). Scale bar: 100 µm

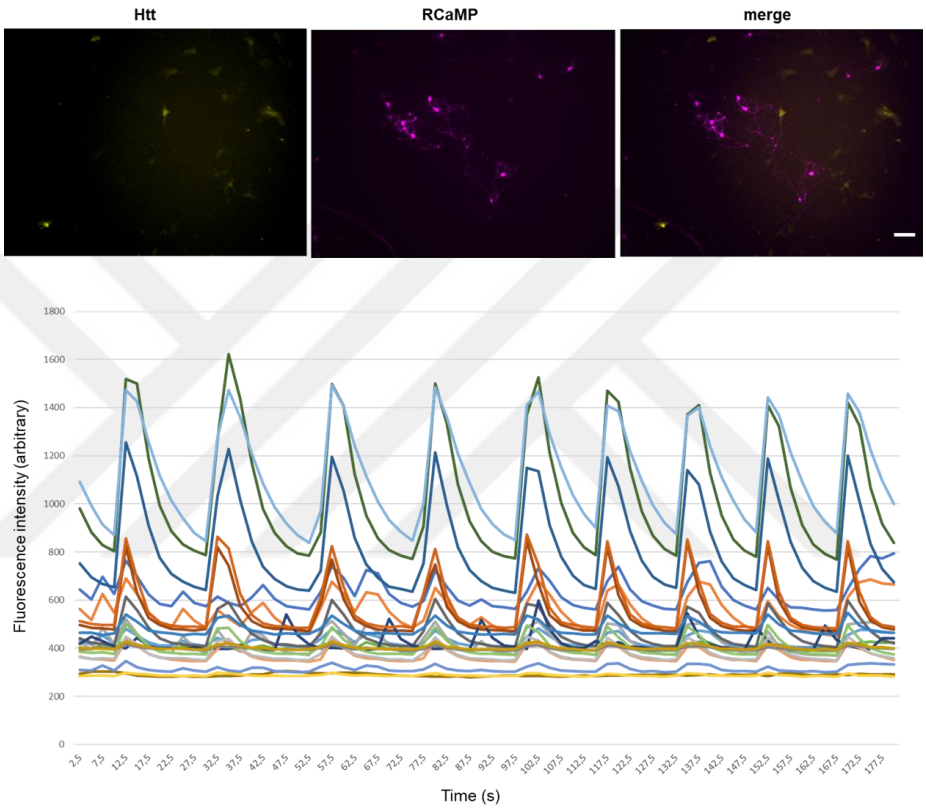

Figure 3.60: Spontaneous calcium activity of neurons neighboring mutant Htt expressing cells.

Primary cortical neurons were isolated from 0-3 days old animals as described in Methods, and transduced with a red calcium indicator AAV-Syn-RCaMP. At 1-week of transduction, cells were transfected with plasmids encoding mutant Htt using lipofectamine 2000. Fluorescence time lapse images were taken 24 hr after transfection using fluorescence microscope (Zeiss Axio Observer) with 577 nm excitation light for RCaMP (magenta) and 488 nm excitation light for mHtt (yellow) every 2.5 seconds (upper panel). Fluorescence intensities were measured using manual ROI selection with ImageJ for each single neuron and time dependent spontaneous activities were constructed (n=22). Scale bar: 100 µm

3.3. *In vitro* and *in vivo* Modelling of Transneuronal Degeneration

3.3.1. TND in primary DRG neuron culture

For modelling TND using DRG neurons, we first wanted to determine if single DRG neurons form a functional network in culture conditions. To show this, we have cultured primary mouse DRG neurons on multi-electrode arrays, performed single cell level electrical stimulation, and recorded calcium activity from surrounding GCaMP6s expressing neurons. We have found that single cell level electrical stimulation induced calcium events in neighboring neurons, which can be blocked by NMDA, AMPA and Kainate receptor antagonists (published data) [110]. Additionally, using immunocytochemistry we have shown that individual DRG neurons form axo-somatic as well as axo-axonal synaptic connections (**Figure 3.61**) (published data) [110].

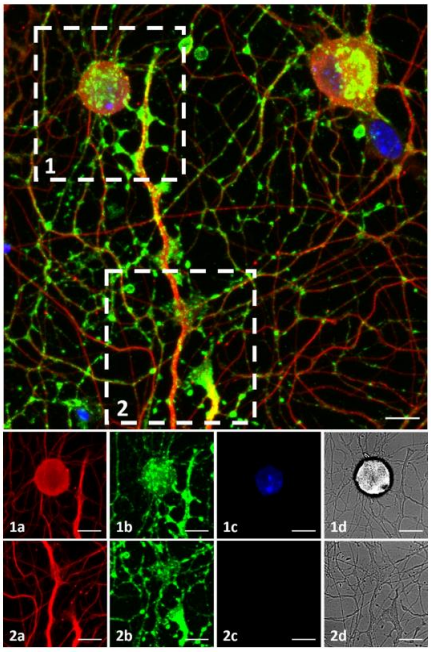

Figure 3.61: Synaptophysin immunoreactivity in DRG cultures.

Primary mouse/rat DRG neurons were isolated from adult mice and analyzed for synaptic connectivity using neuronal marker (anti-β-III-Tubulin; red; 1a,2a) and synaptic marker (anti-synaptophysin; green; 1b,2b). Localized synaptophysin immunoreactivity were detected near axo-somatic (dashed rectangle 1, 1a-1d) or axo-axonal (dashed rectangle 2, 2a-2d) connections. Hoechst staining was performed to identify nuclei (1c,2c), and all images were taken in confocal microcope (Zeiss LSM 780). Scale bar: 10 µm

As we hypothesized that spreading of neurodegeneration occurs through purinergic signaling activated in response to traumatic injury, DRG neurons from wildtype and P2X7KO mice are cultured on marked glass bottomed dishes and single cell axotomies (a total of 10 neurons in each petri dishes) were performed at 48h of culture as described in the Methods section (Figure 3.62).

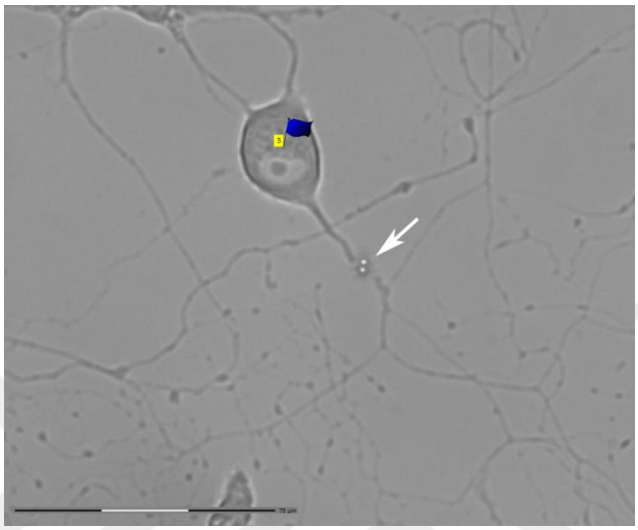

Figure 3.62: Representative brightfield image of an axotomized DRG cell. DRG neurons were isolated from adult mice and cultured for 48h. Single cell axotomies were performed (total 10 neurons were axotomized from each petri dish) using UV laser under phase contrast imaging using PALM microscope (Zeiss). Scale bar: 75 µm.

Cells were then stained with propidium iodide and tile scan images were taken to determine spontaneous cell death. Total of 10 axotomies were performed in each culture dish using UV laser, after which cells were cultured for an additional 24h. Pre- and post-axotomy cell viability analyses were performed for each non-axotomized cells as a measure of transneuronal death. Under these conditions, transneuronal cell death was found to be significantly decreased in P2X7KO neurons compared to wildtype neurons in (Figure 3.63), indicating that the purinergic receptor P2X7 indeed is important for TND in DRG axotomy paradigm.

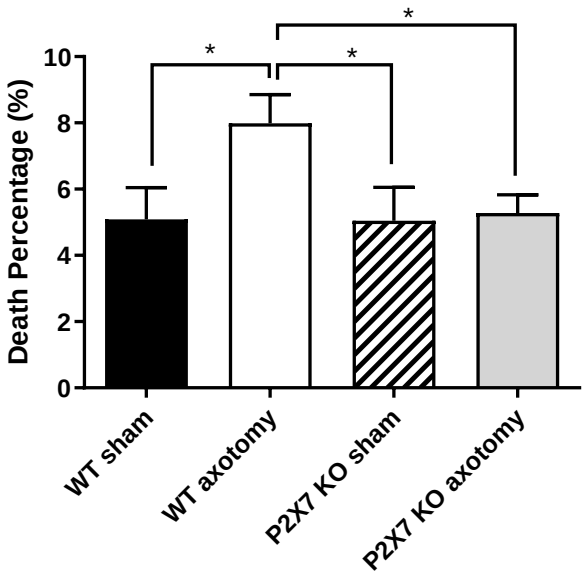

Figure 3.63: Cell viability analysis of DRG neurons in response to axotomized neurons nearby.

DRG neurons were isolated from adult mice and cultured for 48h. Cells were stained with PI and tile scan images (8x8) were taken from each petri dish using fluorescence/phase contrast microscope (Zeiss PALM) to determine baseline of cell viability. A total of 10 neurons were axotomized using UV laser in each petri dish and tile scan images were taken from the same locations 24h after axotomies. UV laser shot at empty locations as sham controls in separate petri dishes. Viability analysis of neighboring neurons is performed 24h after single cell axotomies. Live (PI negative) and dead (PI positive) neurons were counted and cell viability percentages were calculated from at least 2 petri dishes in each in 3 biological repeats. Statistical analysis was done using t test from single cells (n>500).

3.3.2. TND in Primary Hippocampal Neuron Culture

3.3.2.1 Heterogeneity of Hippocampal Cultures

Neurons can vary greatly in structure and specialization. In order to analyze whether the results observed above are specific to DRG neurons, we have repeated our analyses in primary hippocampal neurons. Hippocampal cells were isolated from p1-p3 newborn mice and cultured in glass bottomed petri dishes. Cultures were found to be mainly composed of neuronal and glial (primarily astrocyte) cells (Figure 3.64).

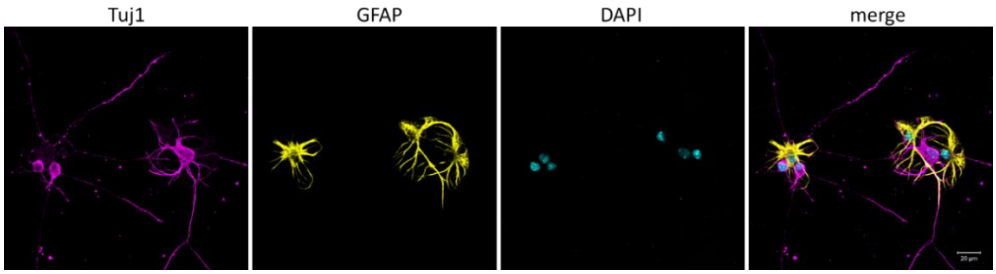

Figure 3.64: Confocal images of hippocampal cell culture.

Immunostaining is performed on day 2 of cell culture, showing astrocytes (GFAP, yellow) and neurons (Tuj1, magenta). DAPI (cyan) was used to stain nuclei of cells. Images were taken using confocal microscope (Zeiss LSM 780) using 40x oil objective (NA:1.4). Scale bar: 30 µm

3.3.2.2 Calcium Activity Analysis During Single Cell Axotomies

Calcium signaling is highly increased in neurons undergoing axotomy. In order to monitor calcium signaling profile in neurons surrounding the axotomized cell, we have transduced primary hippocampal neurons with AAV-Syn-GCaMP6s, a genetically encoded calcium sensor. Cells were essentially incubated for 1 week to achieve GCaMP6s expression. Time lapse images were then taken in order to measure spontaneous calcium activities in axotomized as well as surrounding neurons before (Figure 3.65) and after (Figure 3.66, Figure 3.67) axotomy.

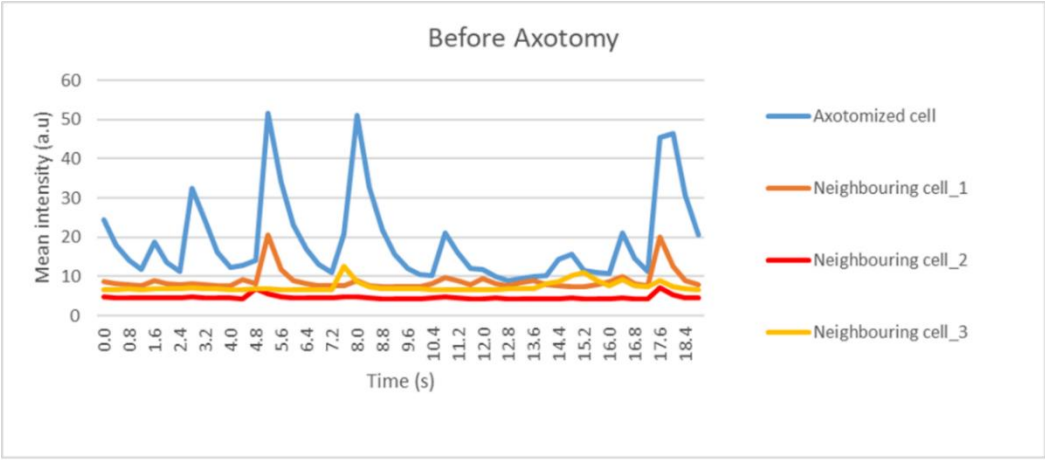

Figure 3.65: Spontaneous calcium activities of hippocampal neurons.

Live imaging of spontaneous calcium activity in GCaMP6s expressing hippocampal neurons showing active network between cells taken each 8 seconds. Time lapse

images were taken using confocal microscope (Zeiss LSM 880) and laser axotomies were performed with UV laser (Rapp Optoelectronics) during time lapse imaging. (a.u.: arbitrary units)

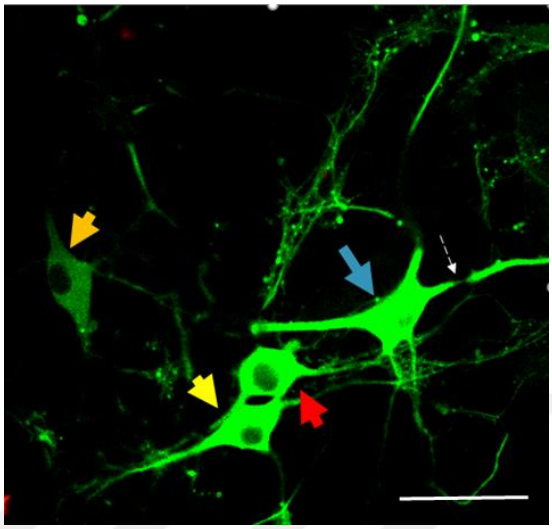

Figure 3.66: Calcium imaging of single cell axotomy and neighboring neurons. Primary hippocampal neurons were isolated from 0-3 days old animals as described in Methods, and transduced with a green calcium indicator AAV-Syn-GCaMP6s. At 1-week of transduction, confocal images were taken with 488 nm excitation laser for GCaMP (yellow) imaging (Zeiss LSM 880). Blue arrow corresponds to the axotomized cell and white arrow indicates axotomy point. Yellow, orange and red arrows indicating neighboring cells. Scale bar: 50 µm

Time lapse recordings revealed that intracellular calcium signaling intensity in axotomized neuron was increased to over 80a.u right after axotomy and stayed at a plateau at around 70 a.u (Figure 3.67). Intracellular calcium signaling intensity was much lower and oscillated in waves (between 10 and 50 au) in this neuron before axotomy (Figure 3.65). Calcium activities of neighboring neurons were at baseline before axotomy (Figure 3.65), however the signaling activity was greatly increased and oscillations were synchronized (Figure 3.67).

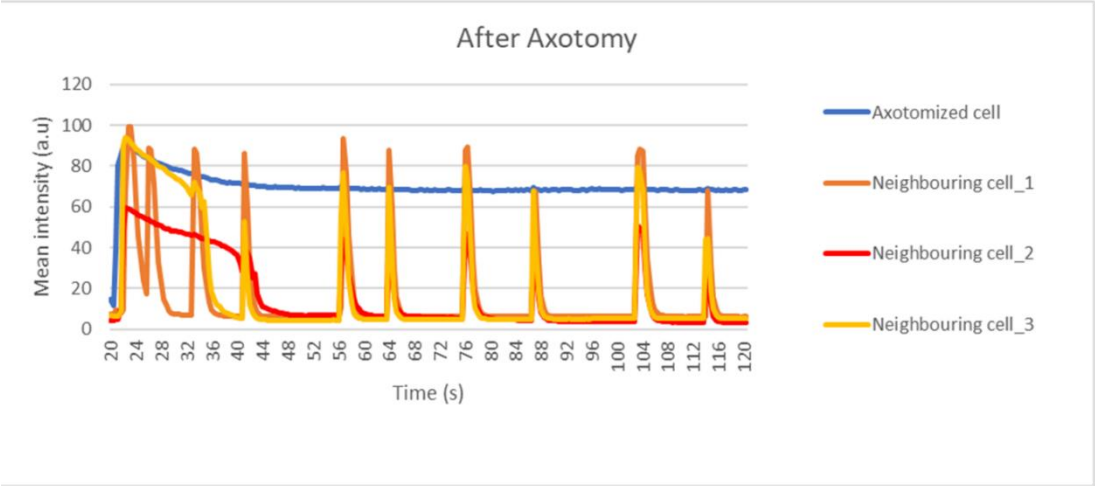

Figure 3.67: Calcium activities of axotomized and neighboring healthy hippocampal neurons during and after axotomy.

Axotomy of a single neuron in an active network resulted with synchronized calcium activity in neighboring uninjured neurons (a.u.: arbitrary units).

3.3.3. *In vivo* Modelling of TND

In vitro experimentation showed that injury of a single neuron can affect neighboring (otherwise healthy) cells in terms of calcium signaling activity, cell death, and changes in gene expression. To validate these results under *in vivo* conditions, we have implemented a model that enables us to simultaneously perform and monitor single cell axotomies in live mice. To that end, we have used B3TUB-EGFP transgenic mice (mice with EGFP expressing neurons to identify neurons under fluorescence imaging). Hence in these mice; neurons in DRG can be spotted as EGFP signal in live animals. Using this paradigm, we have been able to simultaneously monitor cell death by intravenous injection of PI. In order to determine whether our experimental setup or the surgical procedure itself caused cell death, we have imaged the same DRGs 4h after mock surgery and confirmed that no neuronal death was present (Figure 3.68).

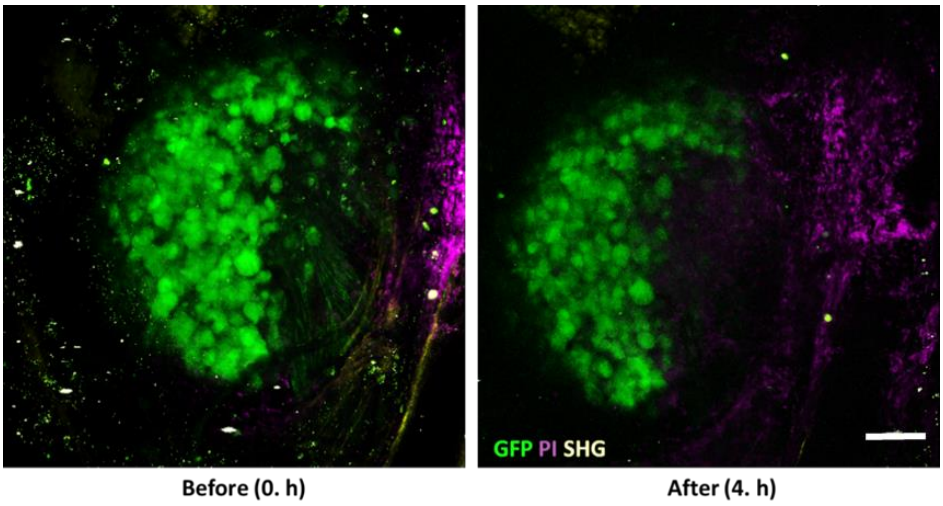

Figure 3.68: Mock surgery of 2p imaging of DRG in live mice. B3TUB-EGFP mice were anesthetized and PI was injected intravenously from tail vein. Afterwards DRG was exposed surgically. 2p images were taken using 10x dry objective (NA:0.45). DRG neurons were appeared as EGFP positive (green), dead cells were identified as PI positive (magenta) cells and DRG capsule was imaged as SHG of collagen layer. Images were taken 5 min after (left panel) and 4h after (right panel) mock surgery. Scale bar: 100 µm

To implement single cell injury model *in vivo,* we have used these animals to injure a single DRG neuron with IR laser (Figure 3.69white arrow) and imaged the same DRG 4 hr after axotomy for TND. We have found that, similar to *in vitro* conditions, single cell injury indeed caused death in neurons surrounding the axotomized neuron (Figure 3.69, white arrow). Such an *in vivo* model would be valuable to investigate the role of purinergic receptors in TND in future studies.

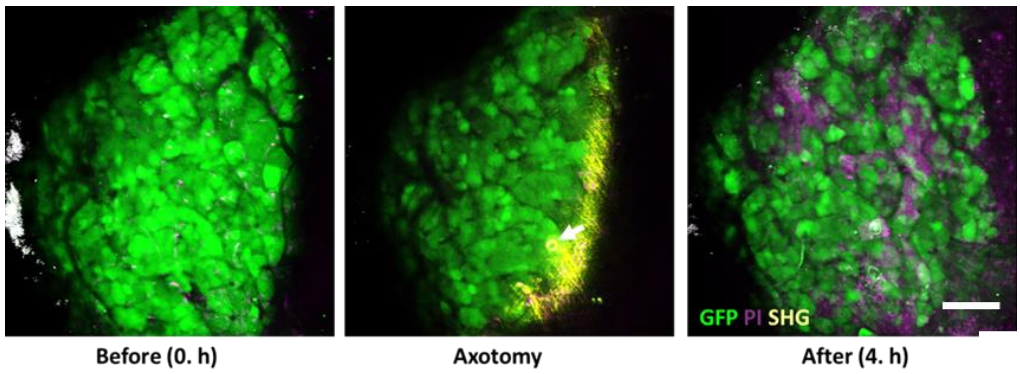

Figure 3.69: 2p imaging of DRG in live mice after single cell injury.

B3TUB-EGFP mice were anesthetized and PI was injected intravenously from tail vein. Afterwards DRG was exposed surgically. 2p images were taken using 10x dry objective (NA:0.45). DRG neurons were appeared as EGFP positive (green), dead cells were identified as PI positive (magenta) cells and DRG capsule was imaged as SHG of collagen layer. Images were taken 5 min after (left panel) surgery, during single cell injury (center panel) and 4h after (right panel) single cell axotomy. Scale bar: 100 µm

4. DISCUSSION

In traditional point of view, neurotoxicity in different neurodegenerative diseases has been linked to distinct genetic and molecular events. These factors are well defined specifically in most neurodegenerative conditions such as AD, PD, HD. Although the protein aggregations, symptoms and affected brain areas are different in each condition, recent approaches revealed that common pathways such as inflammation, oxidative stress or mitochondrial deficits are observed through the progression of pathology in both sporadic or familial cases in most of the neurodegenerative diseases [111]. Computational analysis using human protein-protein interaction network data in AD, HD and PD confirmed a total of 81 enriched KEGG pathways which are also involved in other diseases such as cancer or inflammatory diseases [112]. Discovery of common pathways between related or even unrelated diseases is crucial for application of drug repositioning approach. Genome-wide association studies (GWAS) based network analysis revealed that genes that are associated with AD and PD intersect on Jun/Fos transcription factor pathways [113]. A recent multi –OMICS study utilizing transcriptomic and proteomics data in AD, HD, PD and ALS revealed that a total of 139 genes are differentially expressed in all of these diseases [114]. Each neurodegenerative model has its own advantages and disadvantages. In example, protein aggregation is best studied in HD model as it offers a stable and reproducible system and allows simple microscopic monitoring of the process. Findings in HD on the other hand may contribute to the identification of molecular pathways that play roles in other progressive proteinopathies. Therefore, we proposed that studying multiple neurodegenerative conditions may offer broader perspective for identifying common pathways among progression of neurodegeneration.

This thesis is composed of three main chapters, each one based on a different neurodegenerative condition. Common or distinct neuroprotection mechanisms are determined in PD, HD and traumatic injury.

In the scope of first chapter, we utilized different *in vitro* models of PD based on literature, compared them and chose the most convenient ones for further experimentation. Firstly, we overexpressed wild-type and mutant α-synuclein in SH-SY5Y cells and performed aggregation and cell viability analysis. Wild-type or mutant α-synuclein overexpression did not cause any significant cell toxicity or visible

aggregation (Figure 3.4). Contrary to these findings, Iwata et al. shows that expression of both wild-type and mutant α-synuclein leads to death of Neuro2a cells [85]. In a study with PC12 cells, wild-type α-synuclein expression did not affect cell viability, while mutant α-synuclein expression caused cell death after day 5 [115]. As opposed to these studies and supportive to our findings, a study using SH-SY5Y cells showed that wild-type or mutant α-synuclein did not cause cell death, but increased oxidative stress, thus making cells more sensitive to an external toxic effect [86]. To test this finding, we treated wild-type or mutant α-synuclein overexpressing and SH-SY5Y cells with 6-OHDA and observed that 6-OHDA induced toxicity is increased in α-synuclein overexpressing cells though this increase was not significant (Figure 3.7). These findings lead us to decide to use 6-OHDA induced PD model as it has more consistent results in literature compared to α-synuclein overexpression. As chemical treatment is not suitable for studying single cell scale, and α-synuclein overexpression by itself is not sufficient to induce toxicity, we decided not to use PD as a TND model in the scope of this thesis.

We found that 24h treatment of 6-OHDA resulted with significant cell toxicity in SH-SY5Y cells and performed microarray analysis in 12h and 18h of treatment 6-OHDA to determine gene expression changes in SH-SY5Y cells prior to death. Bioinformatics analysis was performed in Çakır. Lab and RT-PCR validations were performed by Ekin Sönmez (Figure 3.8, Figure 3.9). Different drugs targeting the overexpressed genes in response to 6-OHDA treatment are determined and a total of 5 drugs (Indomethacin, Quercetin, Rutin, Pentagastrin and Simvastatin) are selected for further experimentation based on their usages in literature. Target genes of Indomethacin and Rutin is aldo-keto reductase family 1, member C3 (AKR1C3), Simvastatin acts on integrin beta 2 complement complement 3 receptor 3 and 4 subunit (ITGB2), and Quercetin is effective on CCAAT/enhancer binding protein beta (CEBPB) genes (Table 3.1). Upregulations of these genes in response to 6-OHDA treatments are confirmed by RT-PCR (Figure 3.9). Drug targets are prepared and used in varied concentrations described in literature. Pentagastrin is known to bind to cholecystokinin B receptor and increases neuronal excitability [116]. It didn't confer significant changes in cell viability in any of the applications. Indomethacin is a non-steroidal anti-inflammatory drug which inhibits AKR1C3 [117]. Simvastatin is used for treatment of hypercholesterolemia as it inhibits cholesterol synthesis and it is a

potential regulator of ITGB2. We could not validate the microarray findings of ITGB2 with RT-PCR as it didn't show significant gene expression change compared to vehicle treatment (Figure 3.9). Nevertheless we wanted to test its efficacy as literature holds many data about its protective effects in 6-OHDA or MPP induced toxicities [118-121]. It is shown that Indomethacin is protective against nitric oxide dependent toxicity through scavenging activity and it is also found to be protective against amyloid beta induced toxicity in human neuroblastoma cells and 6-OHDA induced toxicity in PC12 cells [122-125]. Conversely, it didn't confer any neuroprotection in an MPP induced PD model in SH-SY5Y cells [126]. Also, we did not observe any neuroprotective effect of indomethacin in response to 6-OHDA toxicity. Besides, Rutin, which is a flavonoid is determined as another potential inhibitor of AKRC13 [127]. Rutin is found to be neuroprotective against 6-OHDA induced cell toxicity in SH-SY5Y cells when applied at low or high concentrations. It is effective as a pre-treatment or post-treatment application (Figure 3.12, Figure 3.13). We selected Quercetin as CEBPB inhibitor as it was shown to protect neuronal cell lines from toxicity arisen in PD or AD models [128-131]. Upregulation of CEBPB in microarray data is confirmed by RT-PCR (Figure 3.9). Pre-treatment of SH-SY5Y cells with low doses of Quercetin is protective against 6-OHDA induced toxicity while it is toxic when applied at high concentration (Figure 3.13). We further confirmed the downregulation of AKR1C3 and CEBPB in quercetin and rutin pretreated cells. As expected, Rutin downregulated AKR1C3 expression while quercetin didn't have any effect on it. Interestingly, CEBPB expression is downregulated in both quercetin and rutin treated cells (Figure 3.14). Possibly, this is caused by bioconversion of rutin to quercetin by rutinosidase [132]. In addition to expression of target genes and cell viability analysis, we determined the efficacies of quercetin and rutin by investigating PD related genes. We determined that, both quercetin and rutin pre-treatments decreased the expression of SNCA, LRRK1 and LRRK2 which are upregulated in response to 6-OHDA application (Figure 3.15). We previously showed that, Elk1 is correlated with neuronal survival in injured or uninjured DRG neurons [133]. Additionally, we recently found that Elk1 expression is increased in dentate gyrus of rats in response to maximal electroconvulsive shock treatment, which is used as a depression treatment [134]. We thought that upregulation of Elk1 may be an important endogenous neuroprotection mechanism. As we wanted to determine common

neuroprotection mechanisms in different neurodegenerative conditions, we overexpressed Elk1 in SH-SY5Y cells and treated them with 6-OHDA (Figure 3.16). Cell viability of Elk1 overexpressing cells are significantly increased compared to mock transfection (Figure 3.17).

It is shown that, exhibiting dopaminergic phenotype is an important factor for α-synuclein-related toxicity in cells, and opposed to this, α-synuclein presence acts as a neuroprotective factor in non-dopaminergic cells [87]. LUHMES cells were created by immortalizing cells isolated from 8-week-old embryonic human mesencephalic tissue with the LINX v-myc retrovirus and differentiated into a dopaminergic phenotype as a result of tetracycline-dependent activation of myc expression [135]. In order to confirm our findings in SH-SY5Y cells and findings in literature, we differentiated LUHMES cells (Figure 3.18) and used them as a reliable dopaminergic model [107, 135]. Normal and α-synuclein overexpressing LUHMES cells (LUHMES-aSyn-iRES-GFP) are differentiated and α-synuclein overexpression is confirmed via EGFP signal and western blotting (Figure 3.19, Figure 3.20). Normal or α-synuclein overexpressing differentiated LUHMES cells are treated with different concentrations of 6-OHDA and cell viability analysis is performed (Figure 3.21). α-synuclein overexpression did not have any significant effect on cell viability in the presence or absence of 6-OHDA (Figure 3.21). Additionally, 6-OHDA toxicity is higher in LUHMES cells compared to SH-SY5Y cells when applied in same concentrations. A study confirmed that α-synuclein overexpression did not increase MPP induced toxicity in LUHMES cells but found to be protective. Besides, MPP toxicity is increased when α-synuclein was silenced with siRNA [106]. In order to determine gene expression changes in 6-OHDA induced PD model in normal and α-synuclein overexpressing LUHMES cells, RNASeq analysis is performed. Similar to SH-SY5Y cells, CEBPB is upregulated in 6-OHDA treated LUHMES cells. In order to test efficacies of quercetin and rutin in LUHMES cells, pretreatment of drugs is done before 6-OHDA application. It is found that low dose of rutin is decreased 6-OHDA induced toxicity in normal LUHMES cells (Figure 3.22). Interestingly, both doses of rutin and low dose quercetin significantly decreased 6-OHDA induced toxicity in α-synuclein overexpressing LUHMES cells (Figure 3.23). GO molecular function enrichment analysis in 6-OHDA treated LUHMES-aSyn cells revealed alterations in ATP binding pathway including increased expression of P2RY1 and

decreased expression of P2RX5, P2RX3 and P2RX2 significantly. We thought that purinergic signaling may be a common mechanism among different neurodegenerative conditions and investigated the presence of purinergic pathway as a neuroprotection mechanism in traumatic injury in third chapter. Additionally, KEGG pathway analysis in 6-OHDA treated LUHMES-aSyn cells showed mutual pathways between HD and PD, in particular, cytoskeletal components and glutamatergic signaling. We investigated these mechanisms in the context of second chapter.

Second chapter of this thesis includes modelling HD in *in vitro* systems. We overexpressed exon-1 of wild-type and mHtt in HEK293T and neuronal cells to study its interaction with cytoskeletal elements. Our results showed that, overexpression of EGFP-Htt-exon1-Q74 (mHtt) caused aggregate formation which can be depicted by localized bright condensed EGFP accumulation whereas EGFP-Htt-axon1-Q23 (wild-type Htt) showed a diffuse EGFP signal in whole cell (Figure 3.32). We confirmed aggregate formation using electron microscopy via label-free approach and used CLEM to examine the ultrastructural properties of mHtt aggregates and their vicinity in detail. Array tomography and CLEM revealed the complex fibrillary structure of mHtt aggregates containing membrane residues, presence of fibrillary structures around mHtt aggregates and mitochondrial accumulation within those structures (Figure 3.34). High resolution confocal images revealed that those fibrillary structures are composed of three types of main cytoskeletal proteins. Vimentin is an intermediate filament protein which is mainly responsible for cellular strength and mechanical stability. It is shown that direct interaction of vimentin stabilizes microtubules and contribute to cellular integrity in physiological conditions [136]. In addition, vimentin and F-actin is shown to localize along insoluble protein aggregates in response to aggresome formation [137, 138]. Similarly, our immunocytochemistry analysis showed that Vimentin co-localized to mHtt aggregates (Figure 3.35). Additionally, Contanzo et. al. and Waelter et. al. showed that vimentin filaments are redistributed around mHtt aggregates like a cage structure [47, 48]. Besides, vimentin overexpression increased mHtt aggregation through its phosphorylation by Rho-associated protein kinase (ROCK) resulting with sequestration and immobilization of IRBIT protein to mHtt aggregates [49]. Depending on these findings, we wanted to determine mHtt aggregate-vimentin relation in detail using ultrastructural analysis. CLEM analysis of mHtt and vimentin-miniSOG revealed that vimentin filaments are

intertwined with mHtt aggregates, probably contributing to the aggregate stability (Figure 3.36, Figure 3.37).

It is well known that wild-type Htt is involved in intracellular trafficking through interaction with motor machinery or direct binding to tubulin [42-45]. Gauthier et. al. showed that wild type Htt mediates vesicular transport through interaction with Huntingtin associated protein – 1 (HAP-1) and $p150^{Glued}$ subunit of dynactin. In the presence of polyglutamine expansion, mHtt - HAP-1 and $p150^{Glued}$ interaction is increased which resulted in sequestration of those proteins and decreased microtubule binding hereby impaired vesicular transport [46]. Conversely, Smith et. al. showed that mutation in Htt increases its binding to beta-tubulin and disrupts vesicular transport [139]. We have observed increased beta tubulin expression in mHtt aggregates whereas expression was decreased at its core and surrounding environment (Figure 3.35). Increased binding of beta-tubulin may cause its accumulation within mHtt aggregates and disrupted motor machinery may have impaired its stability at the surrounding environment.

Ultrastructural analysis revealed that mitochondria accumulated at the periphery of mHtt aggregates. This observation confirmed the previous findings that showed ER and mitochondria accumulation at the periphery of aggregates [138]. In addition, we observed fibrillary structures in mitochondria rich zones yet beta-tubulin and vimentin immunoreactivity was low in those regions. Kwan et. al. showed that, microglia from HD patients have motility and migration deficiencies due to disruption of actin remodeling [140]. Another study stated that mHtt impairs actin stress response through transglutaminase 2 activation and defective actin turnover caused by high actin-cofilin cross-linkage [50]. Based on the data from previous work, we thought that filamentous structure among mitochondria rich zone are F-actin filaments and we confirmed this by F-actin staining or LifeAct-tdTom (Figure 3.35, Figure 3.42). 3D segmentation analysis revealed that 40-70 % of aggregates have increased F-actin near them and aggregates with F-actin were larger than those that do not have F-actin accumulation (Figure 3.38). Time-lapse imaging of HEK293T cells revealed that F-actin accumulation starts even before mHtt aggregates are visible, we termed this phenomenon as “coaggregation” (Figure 3.39, Figure 3.40). Besides this, we observed that actin filaments which normally stays at the cell periphery, are relocalized to the aggregation zone (Figure 3.40, Figure 3.41).

As Elk1 is found to be neuroprotective in traumatic injury and PD, we wanted to investigate if this is a common neuroprotection mechanism and determine its effects in the process of mHtt aggregate formation. We co-transfected Elk1 and its different phospho-mutants with mHtt in different time points (Figure 3.43). Overexpression of phospho-mutants of Elk1 but not normal form decreased mHtt aggregation compared to mock transfections (Figure 3.44), To determine if this is due to decrease in total mHtt protein levels we performed western blot analysis and found that S324A phospho-mutant significantly decreased total mHtt level compared to mock transfections (Figure 3.45). As subcellular localization of Elk1 depends its phosphorylation state, we investigated if Elk1 overexpression has an effect on mHtt localization, we did subcellular localization analysis but couldn't detect any differences in nuclear or cytoplasmic localization of mHtt (Figure 3.46). Further, we determined if neuroprotection of Elk1 is associated with cytoskeletal rearrangements in mHtt overexpressing cells. It is found that Elk1 is acting through an F-actin independent mechanism (Figure 3.47).

To confirm our findings in HEK293T cells in primary neurons, we overexpressed wild-type and mHtt in cortical and hippocampal neurons. Similar to HEK293T cells, overexpression of wild-type Htt exhibits diffuse EGFP signal while mHtt forms into subcellular aggregates in hippocampal or cortical neurons (Figure 3.48). Formation and distribution of mHtt aggregates differ depending on the cell type. Riguet et. al. showed that mHtt tends to form cytoplasmic aggregates in HEK293T cells while aggregates are mostly nuclear in primary cortical neurons [138]. Our findings confirmed this data. We observed that aggregates in HEK293T cells were mainly cytoplasmic while nuclear aggregations were higher in neurons (Figure 3.49). Moreover, we observed that nuclear localization in hippocampal neurons is significantly lower compared to cortical neurons. In accordance with this, hippocampal neurons have higher number of axonal aggregates compared to cortical neurons. It is shown that, first 17 aa sequence of Htt (N17) regulates its nuclear localization and cellular toxicity [141]. Phosphorylation of S16 residue is necessary for nuclear accumulation of mHtt aggregates and its phosphorylation is preferably increased in striatal tissue [142]. Tissue based differences in phosphorylation levels may regulate this process. Another study showed that Htt mRNA is specifically located to nucleus in cortical neurons, which may facilitate the perinuclear translation of Htt

and ease trafficking to nucleus [143]. Furthermore, higher spike activity and longer neurite length of cultured hippocampal neurons compared to cortical neurons may result in increased vesicular trafficking and cytoskeletal remodeling [144, 145] which in turn increase axonal accumulation of mHtt aggregates. In addition, we observed that; aggregate formation in hippocampal or cortical astrocytes were smaller, less dense and more diffuse in cytoplasm compared to neurons, possibly due to a more rapid clearance of mHtt in astrocytes via ubiquitin-proteasome system [146]. Similarly, Jansen et. al. showed that nuclear localization of mHtt aggregation is different in glial or neuronal cells [147] . Also, another study showed that nuclear localization of mHtt is cell cycle dependent and it selectively localizes to nucleus in non-dividing cells, even in non-neuronal cells [148]. Further, we analyzed F-actin accumulation near cytoplasmic mHtt aggregates and found that HEK293T have significantly higher F-actin accumulation compared to other cytoplasmic regions but this is not the case in neurons (Figure 3.50, Figure 3.51).

We hypothesized that subcellular localization of F-actin may determine localization of mHtt aggregates. To test this hypothesis, we analyzed subcellular F-actin intensity in HEK29T cells and hippocampal neurons and found that HEK293T cells have higher F-actin intensity in cytoplasm compared to hippocampal neurons (Figure 3.53). Additionally hippocampal neurons have higher axonal aggregates compared to cortical neurons, which supports this finding as hippocampal neurons have significantly higher axonal F-actin intensity compared to cortical neurons (Figure 3.52).

Axonal mHtt aggregation in hippocampal neurons resulted in aggregate containing F-actin rich axonal varicosities which are motile until mHtt aggregates grow larger in size and F-actin intensity is increased (Figure 3.54, Figure 3.55). Tourette et. al. constructed an Htt interaction network which showed that Htt may act as a scaffolding protein by interacting with Rho GTPase signaling and actin remodeling and these interactions are impaired in the presence of mutant Htt [149]. Ultrastructural analysis combined with high resolution airy scan imaging revealed that F-actin filaments form a lattice-like structure at the periphery of mHtt aggregates and cage mitochondria in cell soma or axons (

Figure **3.56**). Based on these findings, we thought that actin filamentation plays an active role in the aggregation process, mitochondrial accumulation and aggregate

size determination. Besides, primary neurons are imaged 1-week after mHtt aggregate imaging and mHtt expressing neurons are dead while aggregates itself are stayed in cultures and not dissolved. Additionally, even if 10% of neurons are mHtt+, most of the neurons are found to be dead which implies existence of TND mechanism in HD.

As a result, we hypothesize that all three types of cytoskeletal elements including beta-tubulin, vimentin and F-actin are involved in mHtt aggregation and have different roles in terms of disrupted intracellular trafficking causing mitochondrial accumulation and aggregate stability. Intertwined vimentin filaments in mHtt aggregates may cause increased aggregate stability together with lattice-like F-actin increase in beta-tubulin poor and mitochondria rich zones can indicate decreased intracellular trafficking.

In the last chapter of this thesis, we investigated transneuronal degeneration in response to traumatic injury in primary neurons. We optimized single cell axotomy using UV laser and simultaneous imaging (Figure 3.62). A total of 10 neurons are axotomized in a single petri dish of DRG culture and cells are imaged 24h after axotomy. Cell viability analysis is performed 24h after axotomies. Cell death of neighboring healthy cells in axotomized group is significantly increased compared to sham injuries (Figure 3.63). The same experimental procedure is repeated in P2X7KO DRG neurons and cell death is decreased to same levels with sham injury (Figure 3.63). Primary hippocampal neurons are cultured and calcium activities are recorded with time-lapse confocal imaging. A single neuron is axotomized in each frame and calcium response of surrounding healthy cells are recorded before (spontaneous activity) or after axotomy. It is determined that axotomy of a neuron caused the surrounding healthy neurons to synchronize in terms of calcium activities for at least 2 min after injury (Figure 3.65, Figure 3.67). A similar pattern was observed in both 6-OHDA model of PD and mHtt overexpression model of HD (Figure 3.30, Figure 3.60). We thought this common phenomenon as an emergency signal among cells in injury zone which probably results with increased cell death. Supporting this, we previously found that increased calcium activity in the close proximity neurons are correlated with cell death observed afterwards (unpublished data). As we modelled neurodegenerative conditions in different types of cell cultures, we also wanted to obtain an *in vivo* model for real-time monitoring of TND. We used a transgenic mouse with EGFP+ neurons for observation and detection of neurons. We constructed a DRG

window for real time observation of DRG neurons in live mice and we confirmed that no death is arisen due to surgical procedures (Figure 3.68). A single neuron injured in DRG caused death of surrounding healthy neurons, which confirms our *in vitro* findings to further (Figure 3.69).

In conclusion, we constructed 6 different *in vitro* neurodegeneration models and one *in vivo* model, all of them allowing the real time monitoring of the progression of neurodegeneration. We determined quercetin and rutin as promising therapeutic drugs as neuroprotection in PD. We used mHtt as a model for investigation of protein aggregation and found its interaction with cytoskeletal elements. Additionally, using distinct methodologies allows us to offer purinergic signaling as a crucial factor in traumatic injury induced TND and propose Elk1 as a common neuroprotective factor in PD and HD.

REFERENCES

[1] Gao H. M., Hong J. S., (2008), "Why neurodegenerative diseases are progressive: uncontrolled inflammation drives disease progression", Trends Immunol, 29(8):357-65.

[2] Castillo X., Castro-Obregon S., Gutierrez-Becker B., Gutierrez-Ospina G., Karalis N., Khalil A. A., et al., (2019), "Re-thinking the Etiological Framework of Neurodegeneration", Front Neurosci, 13:728.

[3] Borgens R. B., Liu-Snyder P., (2012), "Understanding secondary injury", Q Rev Biol, 87(2):89-127.

[4] Sullivan P. G., Rabchevsky A. G., Hicks R. R., Gibson T. R., Fletcher-Turner A., Scheff S. W., (2000), "Dose-response curve and optimal dosing regimen of cyclosporin A after traumatic brain injury in rats", Neuroscience, 101(2):289-95.

[5] Park E., Bell J. D., Baker A. J., (2008), "Traumatic brain injury: can the consequences be stopped?", CMAJ, 178(9):1163-70.

[6] Gitler A. D., Dhillon P., Shorter J., (2017), "Neurodegenerative disease: models, mechanisms, and a new hope", Dis Model Mech, 10(5):499-502.

[7] Avila J., (2010), "Common mechanisms in neurodegeneration", Nat Med, 16(12):1372.

[8] Brettschneider J., Del Tredici K., Lee V. M., Trojanowski J. Q., (2015), "Spreading of pathology in neurodegenerative diseases: a focus on human studies", Nat Rev Neurosci, 16(2):109-20.

[9] Smith D. M., (2018), "Could a Common Mechanism of Protein Degradation Impairment Underlie Many Neurodegenerative Diseases?", J Exp Neurosci, 12:1179069518794675.

[10] Gan L., Cookson M. R., Petrucelli L., La Spada A. R., (2018), "Converging pathways in neurodegeneration, from genetics to mechanisms", Nat Neurosci, 21(10):1300-9.

[11] Masnata M., Cicchetti F., (2017), "The Evidence for the Spread and Seeding Capacities of the Mutant Huntingtin Protein in in Vitro Systems and Their Therapeutic Implications", Front Neurosci, 11:647.

[12] Werner C., Engelhard K., (2007), "Pathophysiology of traumatic brain injury", Br J Anaesth, 99(1):4-9.

[13] Matsushita Y., Shima K., Nawashiro H., Wada K., Tsuzuki N., Miyazawa T., (2000), "Real time monitoring of glutamate following fluid percussion brain injury with hypoxia in the rat", Acta Neurochir Suppl, 76:207-12.

[14] Weber J. T., (2012), "Altered calcium signaling following traumatic brain injury", Front Pharmacol, 3:60.

[15] Pettus E. H., Christman C. W., Giebel M. L., Povlishock J. T., (1994), "Traumatically induced altered membrane permeability: its relationship to traumatically induced reactive axonal change", J Neurotrauma, 11(5):507-22.

[16] Weber J. T., (2004), "Calcium homeostasis following traumatic neuronal injury", Curr Neurovasc Res, 1(2):151-71.

[17] Brookes P. S., Yoon Y., Robotham J. L., Anders M. W., Sheu S. S., (2004), "Calcium, ATP, and ROS: a mitochondrial love-hate triangle", Am J Physiol Cell Physiol, 287(4):C817-33.

[18] Adam-Vizi V., Starkov A. A., (2010), "Calcium and mitochondrial reactive oxygen species generation: how to read the facts", J Alzheimers Dis, 20 Suppl 2:S413-26.

[19] Canty A. J., Huang L., Jackson J. S., Little G. E., Knott G., Maco B., et al., (2013), "In-vivo single neuron axotomy triggers axon regeneration to restore synaptic density in specific cortical circuits", Nat Commun, 4:2038.

[20] Hu G., Huang K., Hu Y., Du G., Xue Z., Zhu X., et al., (2016), "Single-cell RNA-seq reveals distinct injury responses in different types of DRG sensory neurons", Sci Rep, 6:31851.

[21] Dickson D. W., Braak H., Duda J. E., Duyckaerts C., Gasser T., Halliday G. M., et al., (2009), "Neuropathological assessment of Parkinson's disease: refining the diagnostic criteria", Lancet Neurol, 8(12):1150-7.

[22] Wakabayashi K., Tanji K., Odagiri S., Miki Y., Mori F., Takahashi H., (2013), "The Lewy body in Parkinson's disease and related neurodegenerative disorders", Mol Neurobiol, 47(2):495-508.

[23] Thomas B., Beal M. F., (2007), "Parkinson's disease", Hum Mol Genet, 16 Spec No. 2:R183-94.

[24] Klein C., Westenberger A., (2012), "Genetics of Parkinson's disease", Cold Spring Harb Perspect Med, 2(1):a008888.

[25] Bertoncini C. W., Fernandez C. O., Griesinger C., Jovin T. M., Zweckstetter M., (2005), "Familial mutants of alpha-synuclein with increased neurotoxicity have a destabilized conformation", J Biol Chem, 280(35):30649-52.

[26] Chai C., Lim K. L., (2013), "Genetic insights into sporadic Parkinson's disease pathogenesis", Curr Genomics, 14(8):486-501.

[27] Chartier-Harlin M. C., Kachergus J., Roumier C., Mouroux V., Douay X., Lincoln S., et al., (2004), "Alpha-synuclein locus duplication as a cause of familial Parkinson's disease", Lancet, 364(9440):1167-9.

[28] Ulmer T. S., Bax A., Cole N. B., Nussbaum R. L., (2005), "Structure and dynamics of micelle-bound human alpha-synuclein", J Biol Chem, 280(10):9595-603.

[29] Nuscher B., Kamp F Fau - Mehnert T., Mehnert T Fau - Odoy S., Odoy S Fau - Haass C., Haass C Fau - Kahle P. J., Kahle Pj Fau - Beyer K., et al., "Alpha-synuclein has a high affinity for packing defects in a bilayer membrane: a thermodynamics study", (0021-9258 (Print)).

[30] Cook D. A., Kannarkat G. T., Cintron A. F., Butkovich L. M., Fraser K. B., Chang J., et al., (2017), "LRRK2 levels in immune cells are increased in Parkinson's disease", NPJ Parkinsons Dis, 3:11.

[31] Narendra D., Walker J. E., Youle R., (2012), "Mitochondrial quality control mediated by PINK1 and Parkin: links to parkinsonism", Cold Spring Harb Perspect Biol, 4(11).

[32] McLelland G. L., Soubannier V., Chen C. X., McBride H. M., Fon E. A., (2014), "Parkin and PINK1 function in a vesicular trafficking pathway regulating mitochondrial quality control", EMBO J, 33(4):282-95.

[33] Zhang L., Wang J., Wang J., Yang B., He Q., Weng Q., (2020), "Role of DJ-1 in Immune and Inflammatory Diseases", Front Immunol, 11:994.

[34] Taira T., Saito Y., Niki T., Iguchi-Ariga S. M., Takahashi K., Ariga H., (2004), "DJ-1 has a role in antioxidative stress to prevent cell death", EMBO Rep, 5(2):213-8.

[35] Wang Z., Liu J., Chen S., Wang Y., Cao L., Zhang Y., et al., (2011), "DJ-1 modulates the expression of Cu/Zn-superoxide dismutase-1 through the Erk1/2-Elk1 pathway in neuroprotection", Ann Neurol, 70(4):591-9.

[36] Blumenstock S., Dudanova I., (2020), "Cortical and Striatal Circuits in Huntington's Disease", Front Neurosci, 14:82.

[37] Jakab K., Gárdián G., Endreffy E., Kalmár T., Bachrati C., Vécsei L., et al., (1999), "Analysis of CAG repeat expansion in Huntington's disease gene (IT 15) in a Hungarian population", European neurology, 41(2):107-10.

[38] Myers R. H., Vonsattel J. P., Stevens T. J., Cupples L. A., Richardson E. P., Martin J. B., et al., (1988), "Clinical and neuropathologic assessment of severity in Huntington's disease", Neurology, 38(3):341-7.

[39] Cattaneo E., Rigamonti D., Goffredo D., Zuccato C., Squitieri F., Sipione S., (2001), "Loss of normal huntingtin function: new developments in Huntington's disease research", Trends Neurosci, 24(3):182-8.

[40] Caviston J. P., Ross J. L., Antony S. M., Tokito M., Holzbaur E. L., (2007), "Huntingtin facilitates dynein/dynactin-mediated vesicle transport", Proc Natl Acad Sci U S A, 104(24):10045-50.

[41] Reiner A., Dragatsis I., Zeitlin S., Goldowitz D., (2003), "Wild-type huntingtin plays a role in brain development and neuronal survival", Mol Neurobiol, 28(3):259-76.

[42] Brandstaetter H., Kruppa A. J., Buss F., (2014), "Huntingtin is required for ER-to-Golgi transport and for secretory vesicle fusion at the plasma membrane", Dis Model Mech, 7(12):1335-40.

[43] Caviston J. P., Holzbaur E. L., (2009), "Huntingtin as an essential integrator of intracellular vesicular trafficking", Trends Cell Biol, 19(4):147-55.

[44] Hoffner G., Kahlem P., Djian P., (2002), "Perinuclear localization of huntingtin as a consequence of its binding to microtubules through an interaction with beta-tubulin: relevance to Huntington's disease", J Cell Sci, 115(Pt 5):941-8.

[45] McGuire J. R., Rong J., Li S. H., Li X. J., (2006), "Interaction of Huntingtin-associated protein-1 with kinesin light chain: implications in intracellular trafficking in neurons", J Biol Chem, 281(6):3552-9.

[46] Gauthier L. R., Charrin B. C., Borrell-Pages M., Dompierre J. P., Rangone H., Cordelieres F. P., et al., (2004), "Huntingtin controls neurotrophic support and survival of neurons by enhancing BDNF vesicular transport along microtubules", Cell, 118(1):127-38.

[47] Costanzo M., Abounit S., Marzo L., Danckaert A., Chamoun Z., Roux P., et al., (2013), "Transfer of polyglutamine aggregates in neuronal cells occurs in tunneling nanotubes", J Cell Sci, 126(Pt 16):3678-85.

[48] Waelter S., Boeddrich A., Lurz R., Scherzinger E., Lueder G., Lehrach H., et al., (2001), "Accumulation of Mutant Huntingtin Fragments in Aggresome-like Inclusion Bodies as a Result of Insufficient Protein Degradation", Molecular Biology of the Cell, 12(5):1393-407.

[49] Bauer P. O., Hudec R., Goswami A., Kurosawa M., Matsumoto G., Mikoshiba K., et al., (2012), "ROCK-phosphorylated vimentin modifies mutant huntingtin aggregation via sequestration of IRBIT", Mol Neurodegener, 7:43.

[50] Munsie L., Caron N., Atwal R. S., Marsden I., Wild E. J., Bamburg J. R., et al., (2011), "Mutant huntingtin causes defective actin remodeling during stress: defining a new role for transglutaminase 2 in neurodegenerative disease", Human molecular genetics, 20(10):1937-51.

[51] Burnstock G., (1997), "The past, present and future of purine nucleotides as signalling molecules", Neuropharmacology, 36(9):1127-39.

[52] Burnstock G., (2009), "Purinergic cotransmission", Exp Physiol, 94(1):20-4.

[53] Toth A., Antal Z., Bereczki D., Sperlagh B., (2019), "Purinergic Signalling in Parkinson's Disease: A Multi-target System to Combat Neurodegeneration", Neurochem Res, 44(10):2413-22.

[54] Krugel U., Kittner H., Franke H., Illes P., (2003), "Purinergic modulation of neuronal activity in the mesolimbic dopaminergic system in vivo", Synapse, 47(2):134-42.

[55] Poelchen W., Sieler D., Wirkner K., Illes P., (2001), "Co-transmitter function of ATP in central catecholaminergic neurons of the rat", Neuroscience, 102(3):593-602.

[56] Burnstock G., (2007), "Purine and pyrimidine receptors", Cell Mol Life Sci, 64(12):1471-83.

[57] Jacobson K. A., Jarvis M. F., Williams M., (2002), "Purine and pyrimidine (P2) receptors as drug targets", J Med Chem, 45(19):4057-93.

[58] Surprenant A., North R. A., (2009), "Signaling at purinergic P2X receptors", Annu Rev Physiol, 71:333-59.

[59] Liu H., Han X., Li Y., Zou H., Xie A., (2013), "Association of P2X7 receptor gene polymorphisms with sporadic Parkinson's disease in a Han Chinese population", Neurosci Lett, 546:42-5.

[60] Amadio S., Montilli C., Picconi B., Calabresi P., Volonte C., (2007), "Mapping P2X and P2Y receptor proteins in striatum and substantia nigra: An immunohistological study", Purinergic Signal, 3(4):389-98.

[61] Gan M., Moussaud S., Jiang P., McLean P. J., (2015), "Extracellular ATP induces intracellular alpha-synuclein accumulation via P2X1 receptor-mediated lysosomal dysfunction", Neurobiol Aging, 36(2):1209-20.

[62] Marcellino D., Suarez-Boomgaard D., Sanchez-Reina M. D., Aguirre J. A., Yoshitake T., Yoshitake S., et al., (2010), "On the role of P2X(7) receptors in dopamine nerve cell degeneration in a rat model of Parkinson's disease: studies with the P2X(7) receptor antagonist A-438079", J Neural Transm (Vienna), 117(6):681-7.

[63] Wilkaniec A., Gassowska M., Czapski G. A., Cieslik M., Sulkowski G., Adamczyk A., (2017), "P2X7 receptor-pannexin 1 interaction mediates extracellular alpha-synuclein-induced ATP release in neuroblastoma SH-SY5Y cells", Purinergic Signal, 13(3):347-61.

[64] Parvathenani L. K., Tertyshnikova S., Greco C. R., Roberts S. B., Robertson B., Posmantur R., (2003), "P2X7 mediates superoxide production in primary microglia and is up-regulated in a transgenic mouse model of Alzheimer's disease", J Biol Chem, 278(15):13309-17.

[65] McLarnon J. G., Ryu J. K., Walker D. G., Choi H. B., (2006), "Upregulated expression of purinergic P2X(7) receptor in Alzheimer disease and amyloid-beta peptide-treated microglia and in peptide-injected rat hippocampus", J Neuropathol Exp Neurol, 65(11):1090-7.

[66] Sanz J. M., Chiozzi P., Ferrari D., Colaianna M., Idzko M., Falzoni S., et al., (2009), "Activation of microglia by amyloid {beta} requires P2X7 receptor expression", J Immunol, 182(7):4378-85.

[67] Lee H. G., Won S. M., Gwag B. J., Lee Y. B., (2011), "Microglial P2X(7) receptor expression is accompanied by neuronal damage in the cerebral cortex of the APPswe/PS1dE9 mouse model of Alzheimer's disease", Exp Mol Med, 43(1):7-14.

[68] Diaz-Hernandez M., Diez-Zaera M., Sanchez-Nogueiro J., Gomez-Villafuertes R., Canals J. M., Alberch J., et al., (2009), "Altered P2X7-receptor level and function in mouse models of Huntington's disease and therapeutic efficacy of antagonist administration", FASEB J, 23(6):1893-906.

[69] Sharrocks A. D., (2002), "Complexities in ETS-domain transcription factor function and regulation: lessons from the TCF (ternary complex factor) subfamily. The Colworth Medal Lecture", Biochem Soc Trans, 30(2):1-9.

[70] Yang S. H., Bumpass D. C., Perkins N. D., Sharrocks A. D., (2002), "The ETS domain transcription factor Elk-1 contains a novel class of repression domain", Mol Cell Biol, 22(14):5036-46.

[71] Lavaur J., Bernard F., Trifilieff P., Pascoli V., Kappes V., Pages C., et al., (2007), "A TAT-DEF-Elk-1 peptide regulates the cytonuclear trafficking of Elk-1 and controls cytoskeleton dynamics", J Neurosci, 27(52):14448-58.

[72] Demir O., Korulu S., Yildiz A., Karabay A., Kurnaz I. A., (2009), "Elk-1 interacts with neuronal microtubules and relocalizes to the nucleus upon phosphorylation", Mol Cell Neurosci, 40(1):111-9.

[73] Tong L., Balazs R., Thornton P. L., Cotman C. W., (2004), "Beta-amyloid peptide at sublethal concentrations downregulates brain-derived neurotrophic factor functions in cultured cortical neurons", J Neurosci, 24(30):6799-809.

[74] Pastorcic M., Das H. K., (2003), "Ets transcription factors ER81 and Elk1 regulate the transcription of the human presenilin 1 gene promoter", Brain Res Mol Brain Res, 113(1-2):57-66.

[75] Sharma A., Callahan L. M., Sul J. Y., Kim T. K., Barrett L., Kim M., et al., (2010), "A neurotoxic phosphoform of Elk-1 associates with inclusions from multiple neurodegenerative diseases", PLoS One, 5(2):e9002.

[76] Roze E., Betuing S., Deyts C., Marcon E., Brami-Cherrier K., Pages C., et al., (2008), "Mitogen- and stress-activated protein kinase-1 deficiency is involved in expanded-huntingtin-induced transcriptional dysregulation and striatal death", FASEB J, 22(4):1083-93.

[77] Anglada-Huguet M., Giralt A., Perez-Navarro E., Alberch J., Xifro X., (2012), "Activation of Elk-1 participates as a neuroprotective compensatory mechanism in models of Huntington's disease", J Neurochem, 121(4):639-48.

[78] Vibha D., Sureshbabu S., Shukla G., Goyal V., Srivastava A. K., Singh S., et al., (2010), "Differences between familial and sporadic Parkinson’s disease", Parkinsonism & Related Disorders, 16(7):486-7.

[79] Dickson D. W., (2018), "Neuropathology of Parkinson disease", Parkinsonism Relat Disord, 46 Suppl 1:S30-S3.

[80] Blum D., Torch S., Lambeng N., Nissou M., Benabid A. L., Sadoul R., et al., (2001), "Molecular pathways involved in the neurotoxicity of 6-OHDA, dopamine and MPTP: contribution to the apoptotic theory in Parkinson's disease", Prog Neurobiol, 65(2):135-72.

[81] Hasegawa T., Matsuzaki M., Takeda A., Kikuchi A., Akita H., Perry G., et al., (2004), "Accelerated alpha-synuclein aggregation after differentiation of SH-SY5Y neuroblastoma cells", Brain Res, 1013(1):51-9.

[82] Tofaris G. K., Layfield R., Spillantini M. G., (2001), "alpha-synuclein metabolism and aggregation is linked to ubiquitin-independent degradation by the proteasome", FEBS Lett, 509(1):22-6.

[83] Colapinto M., Mila S., Giraudo S., Stefanazzi P., Molteni M., Rossetti C., et al., (2006), "alpha-Synuclein protects SH-SY5Y cells from dopamine toxicity", Biochem Biophys Res Commun, 349(4):1294-300.

[84] da Costa C. A., Ancolio K., Checler F., (2000), "Wild-type but not Parkinson's disease-related ala-53 --> Thr mutant alpha -synuclein protects neuronal cells from apoptotic stimuli", J Biol Chem, 275(31):24065-9.

[85] Iwata A., Maruyama M., Kanazawa I., Nukina N., (2001), "alpha-Synuclein affects the MAPK pathway and accelerates cell death", J Biol Chem, 276(48):45320-9.

[86] Junn E., Mouradian M. M., (2002), "Human alpha-synuclein over-expression increases intracellular reactive oxygen species levels and susceptibility to dopamine", Neurosci Lett, 320(3):146-50.

[87] Xu J., Kao S. Y., Lee F. J., Song W., Jin L. W., Yankner B. A., (2002), "Dopamine-dependent neurotoxicity of alpha-synuclein: a mechanism for selective neurodegeneration in Parkinson disease", Nat Med, 8(6):600-6.

[88] Henstridge C. M., Spires-Jones T. L., (2018), "Modeling Alzheimer's disease brains in vitro", Nat Neurosci, 21(7):899-900.

[89] Choi Y. R., Cha S. H., Kang S. J., Kim J. B., Jou I., Park S. M., (2018), "Prion-like Propagation of alpha-Synuclein Is Regulated by the FcgammaRIIB-SHP-1/2 Signaling Pathway in Neurons", Cell Rep, 22(1):136-48.

[90] Oakley H., Cole S. L., Logan S., Maus E., Shao P., Craft J., et al., (2006), "Intraneuronal beta-amyloid aggregates, neurodegeneration, and neuron loss in transgenic mice with five familial Alzheimer's disease mutations: potential factors in amyloid plaque formation", J Neurosci, 26(40):10129-40.

[91] Giasson B. I., Duda J. E., Quinn S. M., Zhang B., Trojanowski J. Q., Lee V. M., (2002), "Neuronal alpha-synucleinopathy with severe movement disorder in mice expressing A53T human alpha-synuclein", Neuron, 34(4):521-33.

[92] Mangiarini L., Sathasivam K., Seller M., Cozens B., Harper A., Hetherington C., et al., (1996), "Exon 1 of the HD gene with an expanded CAG repeat is sufficient to cause a progressive neurological phenotype in transgenic mice", Cell, 87(3):493-506.

[93] Lin C. H., Tallaksen-Greene S., Chien W. M., Cearley J. A., Jackson W. S., Crouse A. B., et al., (2001), "Neurological abnormalities in a knock-in mouse model of Huntington's disease", Hum Mol Genet, 10(2):137-44.

[94] Menalled L. B., Sison J. D., Dragatsis I., Zeitlin S., Chesselet M. F., (2003), "Time course of early motor and neuropathological anomalies in a knock-in mouse model of Huntington's disease with 140 CAG repeats", J Comp Neurol, 465(1):11-26.

[95] Slow E. J., van Raamsdonk J., Rogers D., Coleman S. H., Graham R. K., Deng Y., et al., (2003), "Selective striatal neuronal loss in a YAC128 mouse model of Huntington disease", Hum Mol Genet, 12(13):1555-67.

[96] Wen S., Aki T., Unuma K., Uemura K., (2020), "Chemically Induced Models of Parkinson's Disease: History and Perspectives for the Involvement of Ferroptosis", Front Cell Neurosci, 14:581191.

[97] Ferrante R. J., Schulz J. B., Kowall N. W., Beal M. F., (1997), "Systemic administration of rotenone produces selective damage in the striatum and globus pallidus, but not in the substantia nigra", Brain Res, 753(1):157-62.

[98] Finnie J. W., Blumbergs P. C., (2002), "Traumatic brain injury", Vet Pathol, 39(6):679-89.

[99] Allegra Mascaro A. L., Cesare P., Sacconi L., Grasselli G., Mandolesi G., Maco B., et al., (2013), "In vivo single branch axotomy induces GAP-43–dependent sprouting and synaptic remodeling in cerebellar cortex", Proceedings of the National Academy of Sciences, 110(26):10824.

[100] Canty A. J., Huang L., Jackson J. S., Little G. E., Knott G., Maco B., et al., (2013), "In-vivo single neuron axotomy triggers axon regeneration to restore synaptic density in specific cortical circuits", Nature Communications, 4(1):2038.

[101] Stosiek C., Garaschuk O., Holthoff K., Konnerth A., (2003), "In vivo two-photon calcium imaging of neuronal networks", Proceedings of the National Academy of Sciences, 100(12):7319.

[102] Razansky D., Klohs J., Ni R., (2021), "Multi-scale optoacoustic molecular imaging of brain diseases", Eur J Nucl Med Mol Imaging, 48(13):4152-70.

[103] Schildknecht S., Karreman C., Pöltl D., Efrémova L., Kullmann C., Gutbier S., et al., (2013), "Generation of genetically-modified human differentiated cells for toxicological tests and the study of neurodegenerative diseases", Altex, 30(4):427-44.

[104] Shu X., Lev-Ram V., Deerinck T. J., Qi Y., Ramko E. B., Davidson M. W., et al., (2011), "A genetically encoded tag for correlated light and electron microscopy of intact cells, tissues, and organisms", PLoS Biol, 9(4):e1001041.

[105] Yiğit E. N., Sönmez E., Söğüt M. S., Çakır T., Kurnaz I. A., (2018), "Validation of an In-Vitro Parkinson's Disease Model for the Study of Neuroprotection", Proceedings, 2(25).

[106] Schildknecht S., Karreman C., Poltl D., Efremova L., Kullmann C., Gutbier S., et al., (2013), "Generation of genetically-modified human differentiated cells for toxicological tests and the study of neurodegenerative diseases", ALTEX, 30(4):427-44.

[107] Zhang X.-m., Yin M., Zhang M.-h., (2014), "Cell-based assays for Parkinson's disease using differentiated human LUHMES cells", Acta Pharmacologica Sinica, 35(7):945-56.

[108] Harris G., Eschment M., Orozco S. P., McCaffery J. M., Maclennan R., Severin D., et al., (2018), "Toxicity, recovery, and resilience in a 3D dopaminergic neuronal in vitro model exposed to rotenone", Archives of toxicology, 92(8):2587-606.

[109] Demir O., Kurnaz I. A., (2013), "Phospho-Ser383-Elk-1 is localized to the mitotic spindles during cell cycle and interacts with mitotic kinase Aurora-A", Cell Biochem Funct, 31(7):591-8.

[110] Bayat F. K., Polat Budak B., Yiğit E. N., Öztürk G., Gülçür H. Ö., Güveniş A., (2021), "Adult mouse dorsal root ganglia neurons form aberrant glutamatergic connections in dissociated cultures", PLOS ONE, 16(3):e0246924.

[111] Kujawska M., Domanskyi A., Kreiner G., (2021), "Editorial: Common Pathways Linking Neurodegenerative Diseases—The Role of Inflammation", Frontiers in Cellular Neuroscience, 15(362).

[112] Li P., Nie Y., Yu J., (2015), "An Effective Method to Identify Shared Pathways and Common Factors among Neurodegenerative Diseases", PLOS ONE, 10(11):e0143045.

[113] Ramanan V. K., Saykin A. J., (2013), "Pathways to neurodegeneration: mechanistic insights from GWAS in Alzheimer's disease, Parkinson's disease, and related disorders", American journal of neurodegenerative disease, 2(3):145-75.

[114] Ruffini N., Klingenberg S., Schweiger S., Gerber S., (2020), "Common Factors in Neurodegeneration: A Meta-Study Revealing Shared Patterns on a Multi-Omics Scale", Cells, 9(12).

[115] Smith W. W., Jiang H., Pei Z., Tanaka Y., Morita H., Sawa A., et al., (2005), "Endoplasmic reticulum stress and mitochondrial cell death pathways mediate A53T mutant alpha-synuclein-induced toxicity", Hum Mol Genet, 14(24):3801-11.

[116] Brack K. E., Lovick T. A., (2007), "Neuronal excitability in the periaqueductal grey matter during the estrous cycle in female Wistar rats", Neuroscience, 144(1):325-35.

[117] Liedtke A. J., Adeniji A. O., Chen M., Byrns M. C., Jin Y., Christianson D. W., et al., (2013), "Development of potent and selective indomethacin analogues for the inhibition of AKR1C3 (Type 5 17β-hydroxysteroid dehydrogenase/prostaglandin F synthase) in castrate-resistant prostate cancer", Journal of medicinal chemistry, 56(6):2429-46.

[118] Butterick T. A., Igbavboa U., Eckert G. P., Sun G. Y., Weisman G. A., Muller W. E., et al., (2010), "Simvastatin stimulates production of the antiapoptotic protein Bcl-2 via endothelin-1 and NFATc3 in SH-SY5Y cells", Mol Neurobiol, 41(2-3):384-91.

[119] Xu Y. Q., Long L., Yan J. Q., Wei L., Pan M. Q., Gao H. M., et al., (2013), "Simvastatin induces neuroprotection in 6-OHDA-lesioned PC12 via the PI3K/AKT/caspase 3 pathway and anti-inflammatory responses", CNS Neurosci Ther, 19(3):170-7.

[120] Tong H., Zhang X., Meng X., Lu L., Mai D., Qu S., (2018), "Simvastatin Inhibits Activation of NADPH Oxidase/p38 MAPK Pathway and Enhances Expression of Antioxidant Protein in Parkinson Disease Models", Front Mol Neurosci, 11:165.

[121] Yan J., Qiao L., Wu J., Fan H., Sun J., Zhang Y., (2018), "Simvastatin Protects Dopaminergic Neurons Against MPP+-Induced Oxidative Stress and Regulates the Endogenous Anti-Oxidant System Through ERK", Cell Physiol Biochem, 51(4):1957-68.

[122] Asanuma M., Nishibayashi-Asanuma S., Miyazaki I., Kohno M., Ogawa N., (2001), "Neuroprotective effects of non-steroidal anti-inflammatory drugs by direct scavenging of nitric oxide radicals", J Neurochem, 76(6):1895-904.

[123] Ferrera P., Arias C., (2005), "Differential effects of COX inhibitors against beta-amyloid-induced neurotoxicity in human neuroblastoma cells", Neurochem Int, 47(8):589-96.

[124] Leuchtenberger S., Maler J., Czirr E., Ness J., Lichtenthaler S. F., Esselmann H., et al., (2009), "Nonsteroidal anti-inflammatory drugs and ectodomain shedding of the amyloid precursor protein", Neurodegener Dis, 6(1-2):1-8.

[125] Ramazani E., Tayarani-Najaran Z., Fereidoni M., (2019), "Celecoxib, indomethacin, and ibuprofen prevent 6-hydroxydopamine-induced PC12 cell death through the inhibition of NFkappaB and SAPK/JNK pathways", Iran J Basic Med Sci, 22(5):477-84.

[126] Tasaki Y., Omura T., Yamada T., Ohkubo T., Suno M., Iida S., et al., (2010), "Meloxicam protects cell damage from 1-methyl-4-phenyl pyridinium toxicity via the phosphatidylinositol 3-kinase/Akt pathway in human dopaminergic neuroblastoma SH-SY5Y cells", Brain Res, 1344:25-33.

[127] Gobec S., Brožič P., Rižner T. L., (2005), "Nonsteroidal anti-inflammatory drugs and their analogues as inhibitors of aldo-keto reductase AKR1C3: New lead compounds for the development of anticancer agents", Bioorganic & Medicinal Chemistry Letters, 15(23):5170-5.

[128] Xi J., Zhang B., Luo F., Liu J., Yang T., (2012), "Quercetin protects neuroblastoma SH-SY5Y cells against oxidative stress by inhibiting expression of Kruppel-like factor 4", Neurosci Lett, 527(2):115-20.

[129] Ahn T. B., Jeon B. S., (2015), "The role of quercetin on the survival of neuron-like PC12 cells and the expression of alpha-synuclein", Neural Regen Res, 10(7):1113-9.

[130] Martin-Aragon S., Jimenez-Aliaga K. L., Benedi J., Bermejo-Bescos P., (2016), "Neurohormetic responses of quercetin and rutin in a cell line over-expressing the amyloid precursor protein (APPswe cells)", Phytomedicine, 23(12):1285-94.

[131] Pakrashi S., Chakraborty J., Bandyopadhyay J., (2020), "Neuroprotective Role of Quercetin on Rotenone-Induced Toxicity in SH-SY5Y Cell Line Through Modulation of Apoptotic and Autophagic Pathways", Neurochem Res, 45(8):1962-73.

[132] Kapesova J., Petraskova L., Markosova K., Rebros M., Kotik M., Bojarova P., et al., (2019), "Bioproduction of Quercetin and Rutinose Catalyzed by Rutinosidase: Novel Concept of "Solid State Biocatalysis"", Int J Mol Sci, 20(5).

[133] Demir O., Aysit N., Onder Z., Turkel N., Ozturk G., Sharrocks A. D., et al., (2011), "ETS-domain transcription factor Elk-1 mediates neuronal survival: SMN as a potential target", Biochimica et Biophysica Acta (BBA) - Molecular Basis of Disease, 1812(6):652-62.

[134] Kandemir B., Davis S., Yiğit E. N., Öztürk G., Yılmaz B., Laroche S., et al., (2020), "Expression of Pea3 protein subfamily members in hippocampus and potential regulation following neuronal stimulation", Neuroscience Letters, 738:135348.

[135] Scholz D., Pöltl D., Genewsky A., Weng M., Waldmann T., Schildknecht S., et al., (2011), "Rapid, complete and large-scale generation of post-mitotic neurons from the human LUHMES cell line", J Neurochem, 119(5):957-71.

[136] Schaedel L., Lorenz C., Schepers A. V., Klumpp S., Köster S., (2021), "Vimentin intermediate filaments stabilize dynamic microtubules by direct interactions", Nature Communications, 12(1):3799.

[137] Johnston J. A., Ward C. L., Kopito R. R., (1998), "Aggresomes: a cellular response to misfolded proteins", The Journal of cell biology, 143(7):1883-98.

[138] Riguet N., Mahul-Mellier A.-L., Maharjan N., Burtscher J., Croisier M., Knott G., et al., (2021), "Nuclear and cytoplasmic huntingtin inclusions exhibit distinct biochemical composition, interactome and ultrastructural properties", bioRxiv:2020.07.29.226977.

[139] Smith R., Bacos K., Fedele V., Soulet D., Walz H. A., Obermuller S., et al., (2009), "Mutant huntingtin interacts with {beta}-tubulin and disrupts vesicular transport and insulin secretion", Hum Mol Genet, 18(20):3942-54.

[140] Kwan W., Träger U., Davalos D., Chou A., Bouchard J., Andre R., et al., (2012), "Mutant huntingtin impairs immune cell migration in Huntington disease", The Journal of clinical investigation, 122(12):4737-47.

[141] Vieweg S., Mahul-Mellier A.-L., Ruggeri F. S., Riguet N., DeGuire S. M., Chiki A., et al., (2021), "The Nt17 domain and its helical conformation regulate the aggregation, cellular properties and neurotoxicity of mutant huntingtin exon 1", Journal of Molecular Biology:167222.

[142] Havel L. S., Wang C.-E., Wade B., Huang B., Li S., Li X.-J., (2011), "Preferential accumulation of N-terminal mutant huntingtin in the nuclei of striatal neurons is regulated by phosphorylation", Human Molecular Genetics, 20(7):1424-37.

[143] Didiot M.-C., Ferguson C. M., Ly S., Coles A. H., Smith A. O., Bicknell A. A., et al., (2018), "Nuclear Localization of Huntingtin mRNA Is Specific to Cells of Neuronal Origin", Cell Reports, 24(10):2553-60.e5.

[144] Charlesworth P., Cotterill E., Morton A., Grant S. G. N., Eglen S. J., (2015), "Quantitative differences in developmental profiles of spontaneous activity in cortical and hippocampal cultures", Neural Dev, 10(1):1.

[145] Sathe S., Chan X. Q., Jin J., Bernitt E., Döbereiner H.-G., Yim E. K. F., (2017), "Correlation and Comparison of Cortical and Hippocampal Neural Progenitor Morphology and Differentiation through the Use of Micro- and Nano-Topographies", Journal of Functional Biomaterials, 8(3).

[146] Zhao T., Hong Y., Li S., Li X.-J., (2016), "Compartment-Dependent Degradation of Mutant Huntingtin Accounts for Its Preferential Accumulation in Neuronal Processes", The Journal of Neuroscience, 36(32):8317.

[147] Jansen A. H. P., van Hal M., op den Kelder I. C., Meier R. T., de Ruiter A.-A., Schut M. H., et al., (2017), "Frequency of nuclear mutant huntingtin inclusion formation in neurons and glia is cell-type-specific", Glia, 65(1):50-61.

[148] Martín-Aparicio E., Avila J., Lucas J. J., (2002), "Nuclear localization of N-terminal mutant huntingtin is cell cycle dependent", European Journal of Neuroscience, 16(2):355-9.

[149] Tourette C., Li B., Bell R., O'Hare S., Kaltenbach L. S., Mooney S. D., et al., (2014), "A large scale Huntingtin protein interaction network implicates Rho GTPase signaling pathways in Huntington disease", J Biol Chem, 289(10):6709-26.

T.C.
İSTANBUL MEDİPOL ÜNİVERSİTESİ
Hayvan Deneyleri Yerel Etik Kurulu (İmü-Hadyek) Kararı

Toplantı Tarihi	Karar No	İlgi	Proje Yürütücüsü
17/07/2019	31		Prof. Dr. Gürkan ÖZTÜRK

"Investigation of Transneuronal Degeneration in Traumatic Injury and Neurodegenerative Diseases" başlıklı bilimsel araştırma etik kurulumuzda görüşülmüş olup, çalışmanın etik kurallara uygun olduğuna "**Oybirliği**" ile karar verilmiştir.
Etik Onay Geçerlilik Süresi: 30 ay

GÖREVİ	ADI SOYADI
Başkan	Prof. Dr. Hanefi ÖZBEK
Üye	Dr. Öğr. Üyesi Ahmet Burak ÇAĞLAYAN
Üye	Dr. Öğr. Üyesi Sultan Sibel ERDEM
Üye	Dr. Öğr. Üyesi Mehmet OZANSOY
Üye	Dr. Öğr. Üyesi Taha KELEŞTEMUR
Üye	Uzm.Vet. Hek. Ekrem Musa ÖZDEMİR
Üye	Cem GÜNEŞ
Üye	Burak Sefa DERİBAŞ

BIOGRAPHY

Esra Nur Yiğit holds a bachelor of science degree in Department of Genetics and Biotechnology as Highest ranked student in the depatment and holds a minor degree in Computer Engineering in 2014. In 2017, She took her master degree in Department of Neuroscience from İstanbul Medipol University. She has continued her education in Department of Biotechnology PhD. programme, in Gebze Technical University since 2017. She participated in a TUBİTAK 1001 project "Anne Sütü Kaynaklı Mikrokimerizmin Araştırılması" (114R078)) in 2015-2017 and a TUBİTAK 1003 project "Parkinson Hastalığı için Transkriptom verilerinin ve Hücre içi Ağyapıların Biyoinformatik Analizi: İlaç Hedefi ve İlaç Geliştirilmesi" (315S302) in 2017-2021. She also qualified for TÜBİTAK – 2211A National PhD Scholarship Program and earned a Scholarship during her PhD.